2009

Analysis And Design Of Wide-angle Foveated Optical Systems

George Curatu
University of Central Florida

ANALYSIS AND DESIGN OF WIDE-ANGLE FOVEATED OPTICAL SYSTEMS

by

GEORGE CURATU
B.S. Ryerson Polytechnic University, 1999
M.S. Laval University, 2002
M.S. University of Central Florida, 2005

A dissertation submitted in partial fulfillment of the requirements
for the degree of Doctor of Philosophy
from the College of Optics and Photonics
at the University of Central Florida
Orlando, Florida

Spring Term
2009

Major Professor: James E. Harvey

ABSTRACT

The development of compact imaging systems capable of transmitting high-resolution images in real-time while covering a wide field-of-view (FOV) is critical in a variety of military and civilian applications: surveillance, threat detection, target acquisition, tracking, remote operation of unmanned vehicles, etc. Recently, *optical foveated imaging* using liquid crystal (LC) spatial light modulators (SLM) has received considerable attention as a potential approach to reducing size and complexity in fast wide-angle lenses. The fundamental concept behind optical foveated imaging is reducing the number of elements in a fast wide-angle lens by placing a phase SLM at the pupil stop to dynamically compensate aberrations left uncorrected by the optical design.

In the recent years, considerable research and development has been conducted in the field of optical foveated imaging based on the LC SLM technology, and several *foveated optical systems* (FOS) prototypes have been built. However, most research has been focused so far on the experimental demonstration of the basic concept using off-the-shelf components, without much concern for the practicality or the optical performance of the systems. Published results quantify only the aberration correction capabilities of the FOS, often claiming diffraction-limited performance at the region of interest (ROI). However,

these results have continually overlooked diffraction effects on the zero-order efficiency and the image quality.

The research work presented in this dissertation covers the methods and results of a detailed theoretical research study on the diffraction analysis, image quality, design, and optimization of fast wide-angle FOSs based on the current transmissive LC SLM technology. The amplitude and phase diffraction effects caused by the pixelated aperture of the SLM are explained and quantified, revealing fundamental limitations imposed by the current transmissive LC SLM technology. As a part of this study, five different fast wide-angle lens designs that can be used to build practical FOSs were developed, revealing additional challenges specific to the optical design of fast wide-angle systems, such as controlling the relative illumination, distortion, and distribution of aberrations across a wide FOV. One of the lens design examples was chosen as a study case to demonstrate the design, analysis, and optimization of a practical wide-angle FOS based on the current state-of-the-art transmissive LC SLM technology. The effects of fabrication and assembly tolerances on the image quality of fast wide-angle FOSs were also investigated, revealing the sensitivity of these fast well-corrected optical systems to manufacturing errors.

The theoretical study presented in this dissertation sets fundamental analysis, design, and optimization guidelines for future developments in fast wide-angle FOSs based on transmissive SLM devices.

ACKNOWLEDGEMENTS

First, I would like to thank my advisor, James Harvey, for guiding me through my research, setting the highest standards, and helping me become a better scientist.

I would like to express my gratitude to my committee members, Glenn Boreman, S-T Wu, and Larry Andrews for their generous assistance, comments, and suggestions.

I would like to thank David Wick for introducing me to foveated imaging and for his support and mentoring during the first year of this research.

I cannot fully express my gratitude to my family for everything they taught me and all their support and encouragement over the years.

Most of all, I would like to thank my father for introducing me to the wonderful world of Optics and for his continued support and mentoring throughout my career.

TABLE OF CONTENTS

LIST OF FIGURES

LIST OF TABLES

1 INTRODUCTION

The research covered in this dissertation was initiated under the first phase of a research grant awarded to the College of Optics/CREOL, University of Central Florida, as part of the Bio Optic Synthetic Systems (BOSS) program, funded by the Defense Advanced Research Projects Agency (DARPA). The goal of the BOSS program was to produce synthetic components that mimic parts of biological vision systems in nature, which often demonstrate a great level of performance and adaptability without the size and complexity of man-made imaging systems. The research effort at CREOL was lead by Professor Shin-Tson Wu from the Photonics and Display Group, as Principal Investigator, and had as objective the development of high-birefringence nematic liquid crystals (LC) to be used in compact foveated optical systems (FOS) covering a very wide field-of-view (FOV).

During the first phase of this project, the Optical Design and Image Analysis Laboratory at CREOL was involved in the task of modeling different optical designs in order to establish the requirements and determine the achievable performance of FOSs for different applications, with FOVs up to 120 degrees.

In the second phase of the BOSS program, research groups at CREOL, Sandia National Laboratories (SNL), and Boulder Nonlinear Systems (BNS) collaborated on a technology demonstration of the FOS concept. Although the optical design and system performance modeling task was not included in the second phase of this research grant, we chose to pursue our independent research in the area of optical design and analysis of wide-angle FOSs.

1.1 Motivation and Objectives of the Dissertation

The independent work presented in this dissertation was motivated by our continued interest in the field of foveated imaging and other related technologies, as well as the apparent need for a thorough study of the optical design, analysis, and optimization of wide-angle FOSs. Studying the system design is vital to understanding design tradeoffs and current technological limitations. A thorough study of the system design, analysis, and optimization could provide clues on the best possible performance of an FOS based on the current technology and compare it to the performance of equivalent conventional optics. This study would also identify key limiting factors in the current transmissive SLM technology, such as resolution, fill-factor, transmission, and phase-stroke. It is very important to understand how these limitations affect the performance of an FOS in order to set realistic performance goals for future developments in practical transmissive SLM devices and wide-angle FOSs.

1.2 Organization of the Dissertation Content

The research work covered in this dissertation is organized in six chapters. This first chapter is an introductory chapter that begins with a general review of fast wide-angle lenses, covering particular optical design challenges and typical solutions. A short description of the foveated human vision system is provided as background to the notion of imaging systems with variable spatial resolution. The concept of optical foveated imaging using transmissive liquid crystal (LC) spatial light modulators (SLM) is briefly introduced as a possible method to develop compact fast wide-angle optical systems. A comprehensive review of the previous research work and current technologies that lead to the concept of optical foveated imaging is also covered in this first chapter.

The second chapter begins with a background section, justifying the need for optical foveated imaging in order to reduce size and complexity in wide-angle foveated imaging systems. A detailed review of the previous research work conducted in optical foveated imaging is covered, and different SLM options and current technologies are discussed. This chapter also defines the motivation and objectives of this dissertation.

Chapter 3 analyzes the diffraction phenomena occurring due to the pixelated SLM aperture, and their effect on the diffraction efficiency and the image quality of a foveated optical system (FOS). The diffraction efficiency and modulation transfer function (MTF)

of an FOS are calculated from the pupil function, taking into consideration the effect of higher diffraction orders on the MTF.

Chapter 4 is a detailed lens design study, covering particularities, challenges, and tradeoffs involved in the optical design of fast wide-angle lenses for optical foveated imaging. Several lens design examples, using spherical, aspheric, and hybrid optics, are presented and analyzed in terms of wavefront aberrations, distortion, relative illumination, and design complexity. This chapter also includes the optical design we developed for an experimental wide-angle FOS prototype that was built as part of a joint effort between several other research groups.

The first section in Chapter 5 covers the methods used in this dissertation to compute the diffraction efficiency and MTF of an FOS for a given lens design and a given SLM. One of the lens design examples proposed in Chapter 4 is chosen as a study case to demonstrate the design, analysis, and optimization of a practical wide-angle FOS based on the current state-of-the-art transmissive LC SLM technology. The optimal SLM resolution for the best FOS performance is determined for this lens design, and the MTF performance is estimated. This chapter also analyzes the effects of fabrication and assembly tolerances on the actual performance of the FOS. A method to calibrate the SLM in order to cancel out additional aberrations introduced by manufacturing errors is proposed. The estimated MTF performance of the optimized FOS design is compared to the MTF of an equivalent conventional lens, taking into account the diffraction efficiency and the SLM transmission of the FOS. At the end of Chapter 5, a few general and

particular foveated imaging system design considerations are covered, relating design parameters to practical application requirements.

Finally, Chapter 6 concludes this dissertation, summarizing the main contributions of this research work to the field of wide-angle optical foveated imaging. This chapter also reviews the main results, findings, and conclusions that emerged from our study.

1.3 Fast Wide-Angle Lenses

Many imaging applications require the use of fast (low F/#) wide-angle lenses to cover a large FOV: surveillance, situational awareness, threat detection, tracking, guidance of unmanned vehicles, etc. The F/# of these lenses is very important, as faster lenses have a larger aperture, and therefore collect more light onto the sensor, allowing for better detection in poor lighting conditions. On the other hand, aberrations increase quickly with the aperture and the field angle, due to the severe "ray bending". As a result, fast wide-angle lenses typically require complex designs with multiple elements, in order to carefully balance and correct these aberrations. The general design idea is to capture a wide FOV, and slowly bend the rays towards the image plane, minimizing steep refraction angles at the optical surfaces.

Wide-angle lenses have a short focal length relative to other lenses matching the same sensor format. The inverted-telephoto (or *retrofocus*) design is a popular configuration

for fast wide-angle lenses (f/1.8 to f/4, 60 to 150 degrees FOV) [1]. The retrofocus arrangement is formed by a front negative component followed by a rear positive component, and is characterized by a long back focal length (BFL) in relation to its effective focal length (EFL). Figure 1 shows the typical retrofocus arrangement. The long BFL is usually required to clear the shutter mechanism, aliasing filter, protective sensor window, and other components that might have to be introduced between the lens and the image plane. It is obvious that a retrofocus configuration is not symmetrical, so correcting coma and distortion is difficult. In many other design configurations, these aberrations are corrected or reduced by an approximately symmetrical arrangement of the elements about the aperture stop.

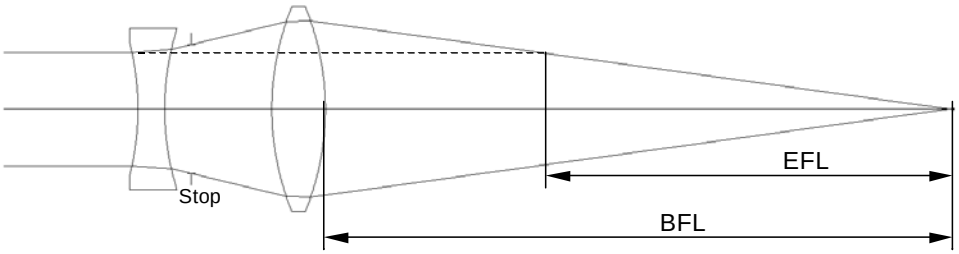

Figure 1: Inverted-telephoto (or retrofocus) arrangement, with BFL > EFL.

Large distortion values are common in reverse telephoto or fish-eye lenses. In most designs, the front element is a strongly bent negative meniscus lens, concave toward the aperture stop and the image plane. This element steers the high-obliquity principal rays through a large angle, directing them into the stop, which introduces a large amount of negative (barrel) distortion. However, in digital imaging applications, since distortion is only a constant magnification error that varies with the field angle, it can be calibrated

and corrected at the firmware level, without losing the image resolution (providing that the resolution of the sensor is large enough to avoid aliasing due to under-sampling).

For most wide-angle lenses, the relative illumination (RI) tends to decrease towards the peripheral fields. One reason this happens is the cosine-fourth falloff rule: the illumination onto the image plane decreases proportionally with the cosine-fourth of the angle of incidence of the chief-ray to the image plane. This effect is undesirable, because the signal-to-noise (S/N) ratio of the system will decrease with the RI, therefore decreasing the resolution of the system towards the peripheral field angles. An image-space telecentric design would solve the problem of the cosine-fourth falloff, but will also make a retrofocus wide-angle lens even more non-symmetrical about the stop, increasing distortion. Therefore, there is a tradeoff in the design of fast wide-angle lenses between flattening the RI and minimizing distortion. In lenses with large distortion, the negative distortion combined with the blur caused by other aberrations can balance the cosine-fourth effect, producing a more uniform RI. Other factors contributing to the drop in RI with is the vignetting at the peripheral field angles.

Even in the case of a fast monochromatic wide-angle lens, where the lens designer does not have to worry about correcting chromatic aberrations, multiple elements have to be used to correct off-axis aberrations. As an example, we designed an 18 mm F/2.8 monochromatic lens, optimized for 532 nm, covering a full-diagonal FOV of 80 degrees with a 25 mm diagonal image (including negative distortion). The lens prescription data

is given in Table 1, and the lens design layout, modulation transfer function (MTF), distortion, and RI are shown in Figure 2.

Table 1: Prescription (all dimension in mm).

Surf: Type		Comment	Radius		Thickness		Glass		Semi-Diameter
OBJ	Standard		Infinity		Infinity				Infinity
1	Standard		Infinity		10.000000				0.000000
2	Standard		63.352547	V	8.000000		BK7		22.336830
3	Standard		19.230013	V	15.000000				15.023323
4	Standard		121.741479	V	5.000000		BK7		11.467153
5	Standard		18.721208	V	8.802470	V			9.343004
6	Standard		-20.050834	V	5.000000		BK7		8.569225
7	Standard		-24.874066	V	3.000000				8.841252
8	Standard		84.460181	V	5.000000		BK7		8.224991
9	Standard		-37.847008	V	1.000000				7.792689
STO	Standard		Infinity		17.640488	V			7.247047
11	Standard		-110.009802	V	6.000000		BK7		12.520079
12	Standard		-36.988632	V	11.536273	V			13.524782
13	Standard		4158.093880	V	5.000000		BK7		15.881733
14	Standard		-63.425901	V	4.200000				16.190369
15	Standard		-29.995662	V	4.000000		BK7		16.232608
16	Standard		-54.222033	V	3.200000				17.565590
17	Standard		91.364567	V	6.000000		BK7		18.947507
18	Standard		-97.819594	V	1.000000				19.025287
19	Standard		48.162935	V	6.000000		BK7		18.705845
20	Standard		191.832507	V	28.000000				18.174601
IMA	Standard		Infinity		-				12.384172

In this design example, we corrected the wavefront aberrations over the entire FOV close to the diffraction limit (< 0.25 waves, peak-to-valley). However, in practical digital imaging applications, fast lenses are not diffraction limited, as aliasing artifacts due to detector sampling can become a problem if the cutoff of the optical MTF is much larger than the Nyquist frequency of the detector array. Only fast wide-angle lenses used in special high-resolution projection systems might require this level of correction. For this lens, it takes nine spherical elements to correct wavefront aberrations close to the diffraction limit, while keeping distortion relatively low (18%), and the RI flat (less than

3% drop). The overall length of the system is 143 mm, with a back focal length of 28 mm.

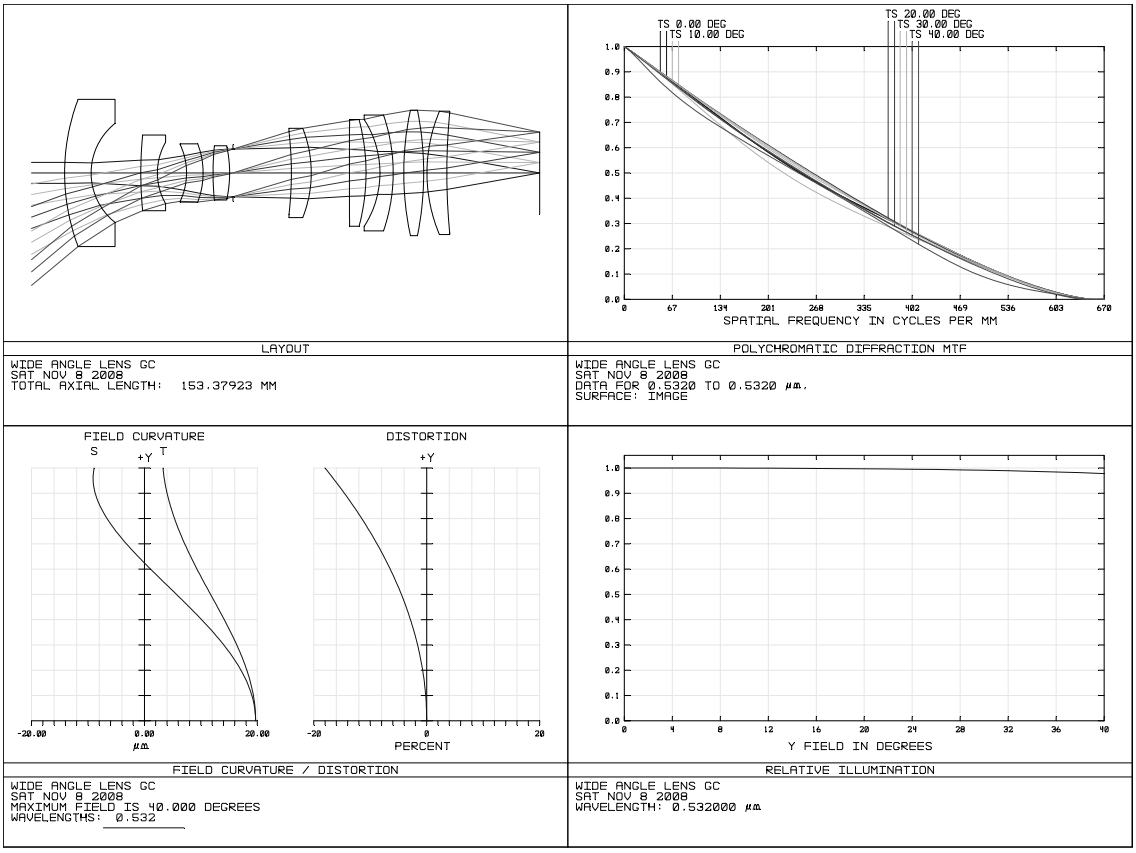

Figure 2: Fast wide-angle lens: 18 mm, F/2.8, 80 degrees FOV. Layout, modulation transfer function, field curvature and distortion, and relative illumination.

1.4 The Human Vision System

In nature, many vertebrates have vision systems covering a wide FOV with variable spatial resolution. This type of vision allows for an optimal use of the brain resources and simplifies the optics of the eye. The human vision apparatus is an excellent example of a

wide FOV imaging system with variable resolution. In essence, the human eye works just like any other imager: the lens forms an image onto the sensor (retina), which is connected to the brain through the optic nerve. A schematic diagram of the human eye is shown in Figure 3 [2].

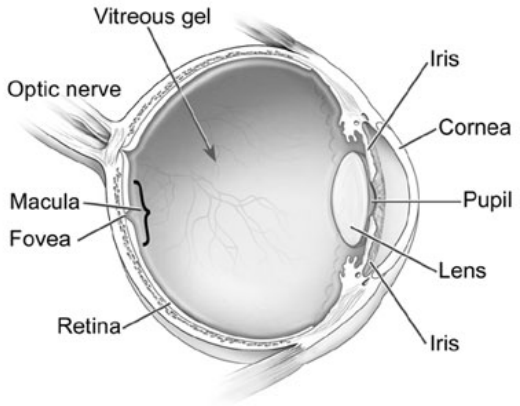

Figure 3: The human eye [2].

The retina is the visible light sensor in the human eye. It contains two types of photoreceptors: rods and cones [3]. The rods are more numerous (~120 million) and more sensitive to light than the cones. On the other hand, multiple rods are connected to a single nerve fiber, and such fiber can be activated by any one of about a hundred rods, which reduces the visual acuity. The 6 to 7 million cones are concentrated in the *macula*, a central yellow spot on the retina, about 3 mm in diameter. In the center of the macula, there is a 0.3 mm diameter rod-free area with very thin densely packed cones, known as *fovea centralis*. The cones in the fovea are thinner, with diameters of 3 μm down to 1.5 μm, and more densely packed than anywhere else in the retina. Also, cones in the

fovea are individually connected to nerve fibers. This makes the fovea the area on the retina capable of the highest visual acuity. Outside of this central region, the eye's spatial resolution drops significantly.

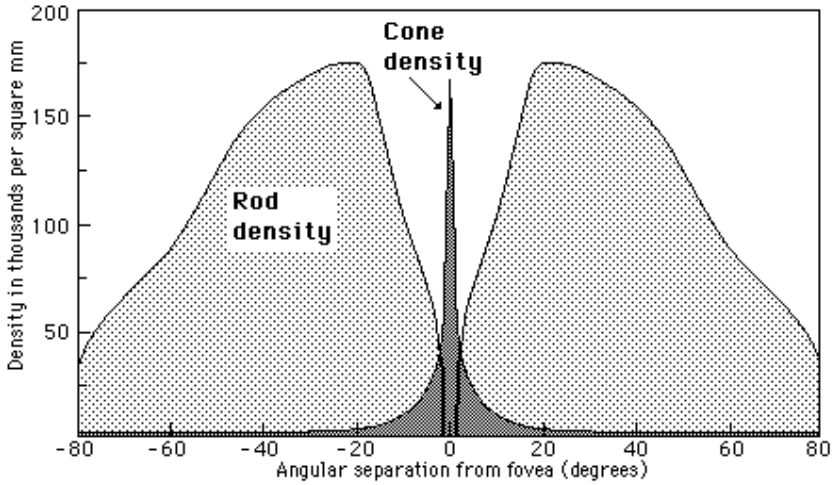

Figure 4: Cone and rod density versus angular field [4].

Although the eye receives data from a field of about 200 degrees, the acuity over most of that range is poor since most of the image is formed onto the area of the retina with a high rod density. Figure 4 shows the cone and rod density versus angular separation from the fovea for the human eye [4]. By studying cone densities, it has been found that the spatial resolution the human eye can resolve is cut in half at about 2 degrees from the point of fixation, and at 20 degrees, the resolution is cut by a factor of ten. For this reason, the eyeball must move continuously, so that light from the object of primary interest always falls onto the fovea.

1.5 The Concept of Optical Foveated Imaging

The natural vision concept of variable spatial resolution is known as *foveated imaging*, and has been applied in wide FOV imaging applications to reduce bandwidth and optics complexity. Foveated imaging was first applied in digital video image processing as a technique of data compression used to speed up the transmission and processing of large video images [5,6,7]. Data compression is achieved by reducing the resolution of the image with the exception of a region of interest (ROI), which could be repositioned every frame to track a moving target within the FOV.

The same foveated imaging concept was applied in optics by Martinez et al., who proposed a compact wide-angle lens with variable resolution across the FOV to reduce the complexity and size of wide FOV optics [8]. The fundamental idea behind the *optical foveated imaging* technique described by Martinez et al. is to reduce the number of elements in a fast wide-angle lens by placing a phase spatial light modulator (SLM) at the pupil stop to selectively correct aberrations at different points within the FOV (as shown in Figure 5). As aberrations vary significantly with the field angle, such lens would form a blurry image over its wide FOV with the exception of a highly resolved ROI. The ROI could be moved dynamically anywhere within the FOV by adjusting the optical path difference (OPD) pattern introduced by the SLM to cancel out the wavefront aberrations at the desired field point.

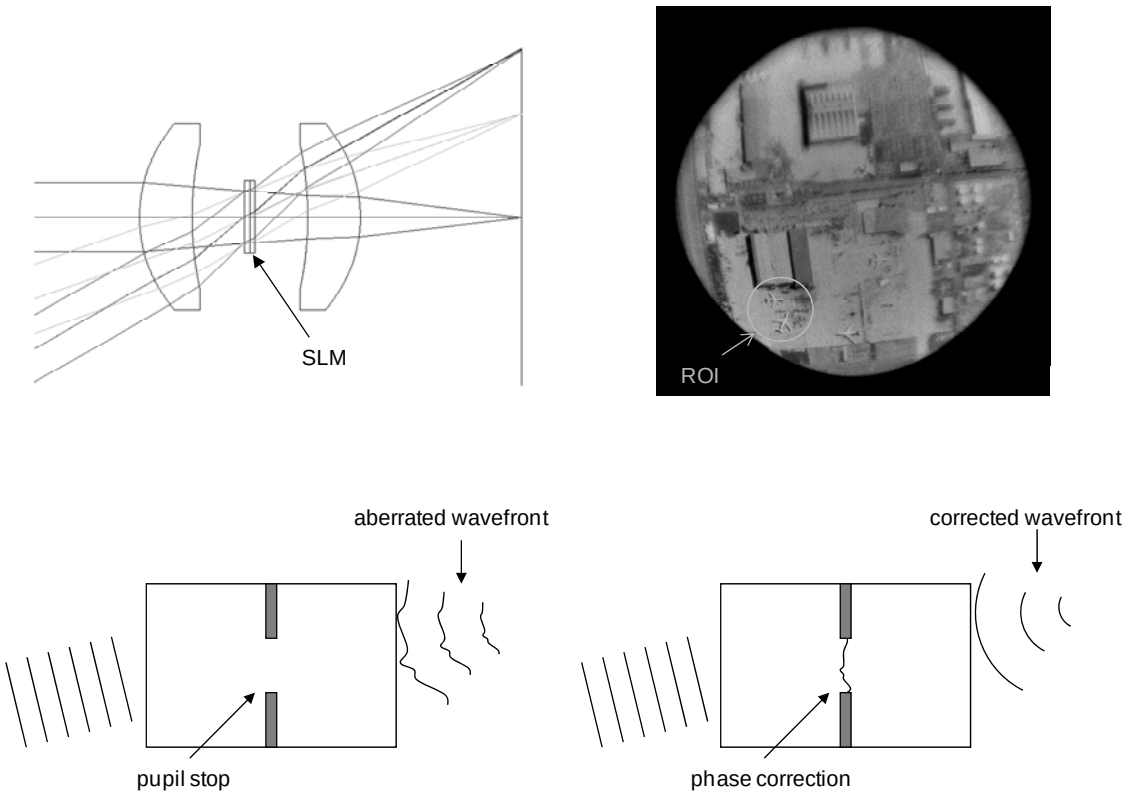

Figure 5: The SLM corrects the wavefront aberration at the field point of interest.

The proposed *foveated optical system* (FOS) resembles in essence to a high-resolution scanning imager overlaid onto a low-resolution wide-angle staring imager. Such hybrid lenses could potentially reduce the complexity and size of wide-angle optics. In addition, FOS's could be combined with foveated data compression techniques at the image processing level or with novel specially developed foveated sensors to save transmission bandwidth and computational resources. A detailed literature review covering research and technologies related to optical foveated imaging is presented in the following section and in the next chapter.

1.6 Related Research and Technologies

Optical foveated imaging was inspired not only by the variable spatial resolution in biological vision systems, but also by already existing technologies like wavefront correction in adaptive optics and the foveated data compression in digital imaging. It was also motivated by emerging novel technologies such as the development of sensors with spatially variant resolution and new advances in high-resolution transmissive SLMs. This section is a comprehensive review of the previous research work and current technologies that lead to the concept of optical foveated imaging. A detailed literature review covering specific research on optical foveated imaging is presented in the next chapter.

1.6.1 Adaptive Optics

For the past thirty years, wavefront correction using phase SLMs has been used extensively in several optics and photonics applications requiring adaptive optics (AO) to compensate dynamic wavefront aberrations. As shown in Figure 6, the correction is done in real-time by continuously sensing the incoming wavefront and adjusting the OPD of an SLM to compensate aberrations [9]. The most common applications are in astronomy and ophthalmology.

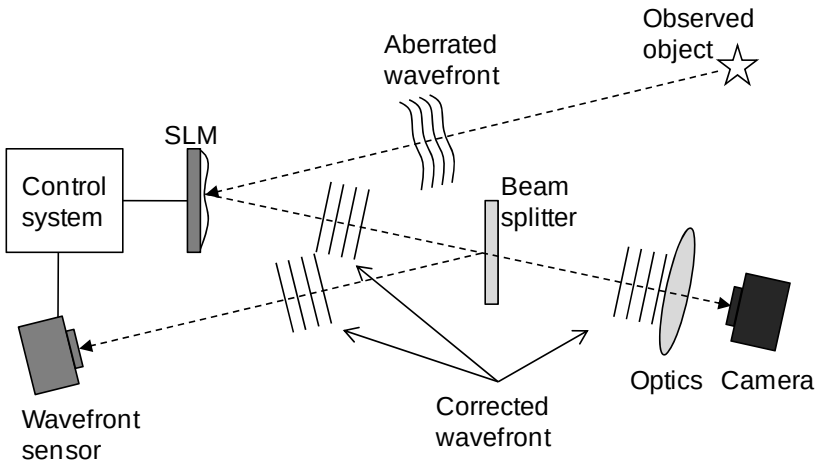

Figure 6: Real-time wavefront correction in adaptive optics.

AO was first used in astronomy to correct the wavefront aberrations created by the atmospheric turbulences in ground-based telescopes. Atmospheric turbulences create random changes in the refractive index of the air, constantly altering the OPD between the observed object and the telescope. SLMs are commonly used in ground-based telescopes to correct the wavefront aberration in real-time, since atmospheric turbulences change rapidly and randomly with time. The SLM is controlled in real-time by sensing the wavefront of the light coming from a *guide star*, which is a reference star close to the observed star, or the observed star itself. This reference can also be created artificially by the backscatter of a laser beam sent into the atmosphere, or by the emission of Sodium atoms in the mesosphere exited by a laser beam. A Shack-Hartmann sensor is usually used to continuously monitor the wavefront and feed back to the SLM the OPD required to correct the aberrations. Countless research papers and several books have been written on the subject of AO applied in astronomy. References [9,10,11] are only a few examples of this vast literature.

AO is also used in ophthalmology to allow high-resolution imaging of the retina [12,13]. Ocular aberrations can severely alter the image of the retina through the lens of the human eye. Defocus and astigmatism in the human eye are often corrected with spectacles or contact lenses, which is usually sufficient for normal visual function. However, additional aberrations such as coma and spherical aberration need to be corrected in order to achieve microscopic resolution. Furthermore, ocular aberrations are not completely stable, and may change very fast, with frequencies up to 100 Hz, as the eye moves and changes shape constantly over time. The correction of these aberrations requires real-time measurement and compensation. Just like in astronomy, the ocular aberrations are corrected by continuously sensing the wavefront coming from the eye with a Shack-Hartmann sensor and adjusting the OPD of an SLM to compensate the aberrations.

1.6.2 Foveated Imaging for Video Data Compression

Most technical literature on foveated imaging focuses on techniques to reduce the amount of video data per frame in order to speed up transmission and processing in digital video imaging applications. In foveated imaging, data compression is achieved by reducing the resolution of a wide-angle image with the exception of a ROI, which can be repositioned every frame. Figure 7 shows an example of foveated imaging with the ROI highly resolved at two different field angles [14]. The image on the left was captured with the ROI located at the bee on the flower, which appears highly resolved, while the butterfly

is hardly discernable. The image on the right was captured after the ROI was moved onto the butterfly, which now appears highly resolved. This multiresolution video compression technique was inspired by the operation of the human eye and is ideal for navigation, display, surveillance, and tracking applications, where images from a wide FOV need to be processed and transmitted in real-time.

Figure 7: Example of foveated images [14].

Extensive work has been done to explore foveation techniques in imaging and display applications. Examples include spatially variant compression ratio in image and video processing [7,15,16], variable levels of detail in three-dimensional rendering [17,18], and variable pixel resolution in imaging or display systems [19]. Previous work on foveated imaging can be placed in two main categories, as follows. The first category focuses on the algorithmic approach, where foveation techniques are applied primarily at the image processing stage to reduce data transmission bandwidth in order to achieve real-time video communication through low-bandwidth networks [5-7,15,16]. The second category of research on foveated imaging takes the hardware approach, where different imaging sensors and displays with spatially varying resolution are developed to acquire, transmit,

and render foveated images directly, without applying foveation algorithms at the image processing stage [8,19,21-23].

Compared to conventional imaging, both foveated imaging approaches provide the benefit of more efficient and faster transmission, post-processing and storage of the video images. However, although both the algorithmic and hardware approaches can achieve foveated imaging, the hardware approach achieves foveated imaging at a more fundamental level. In the algorithmic approach, full-resolution images are captured by conventional imagers with uniform spatial resolution and are processed by applying foveated data compression algorithms. The hardware approach does not require complex image processing algorithms, as foveation is applied directly at the hardware level, where foveated images are being captured by specially developed novel imaging sensors and systems with spatially variant resolution.

1.6.3 The Hardware Approach in Foveated Imaging

In the recent years, the hardware approach received considerable attention, with several research groups investigating various innovative solutions for the development of sensors, imagers and displays with variable resolution. The most straight-forward hardware approach proposed by several researchers was based on multiple imaging systems, where images are acquired simultaneously using two or more imaging systems covering different FOVs with different spatial resolutions. Foveation is achieved by

applying image mosaicing at the software level to combine these images into a single multi-resolution frame [4,5]. For instance, several researchers demonstrated the use of two separate cameras with different angular resolutions to achieve foveated imaging in robotic vision, navigation, and surveillance systems [3,25]. This concept is not new in optics, as the same principle has been applied in some astronomy and military applications, where a *view-finder* with a wider FOV is attached to telescopes in order to help aiming the telescope.

Other researchers proposed a more fundamental hardware approach to achieve foveated imaging, by combining two optical systems with two separate sensors into a single foveated imaging system. For example, Hua et al. developed a dual-sensor foveated imaging system, where a wide FOV is captured onto a sensor array through a low-resolution staring imager, while a scanning imager provides a high-resolution narrow FOV on a separate sensor [24]. This approach does not require the mechanical reorientation of the entire imaging system to follow the ROI. A schematic of the dual-sensor foveated imaging system concept proposed by Hua et al. is shown in Figure 8. The wide FOV is captured by a wide-angle objective lens, which forms an intermediary image. A beam splitter is placed immediately after the intermediary image plane to split and project the image following two separate paths (reflected and transmitted). The wide FOV staring imager uses a relay lens to reimage the reflected intermediary image onto the first sensor. The intermediary image transmitted through the beam splitter is collected by a scanning lens, which forms an intermediary pupil plane. A two-axis scanning mirror is placed at this intermediary pupil plane to redirect rays from the field point of interest

parallel to the optical axis back into the same scanning lens. The scanning lens captures the narrow FOV selected by the scanning mirror, and reimages it onto the second sensor using the same beam splitter to reflect the light towards the sensor. Foveated imaging is achieved by combining the images from the two sensors at the image processing stage.

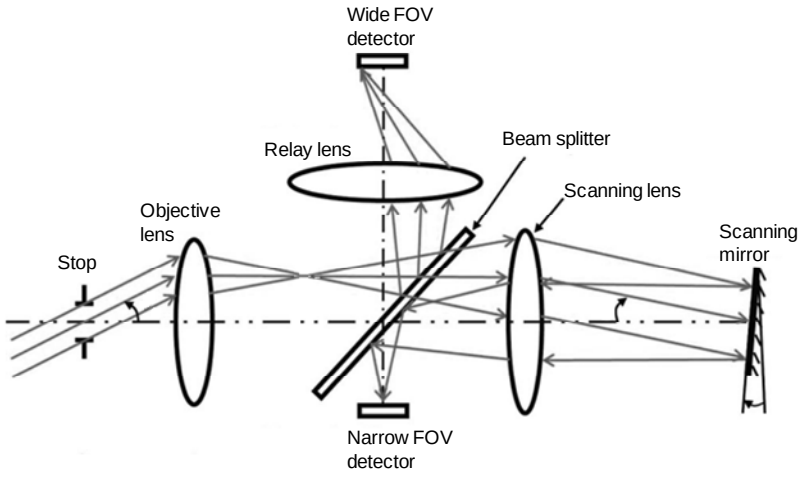

Figure 8: Dual-sensor foveated imaging system proposed by Hua et al. [24].

Hua et al. built a bench prototype of the dual-sensor foveated imaging system using off-the-shelf components. The wide FOV staring optical system had an EFL of 13.2 mm, with an F/9 aperture, and covered a 45 degrees full FOV on a CCD sensor with the maximum resolution of 24 lp/mm (Nyquist frequency). The scanning optical system had an EFL of 22.9 mm, with an F/15 aperture, and covered a 10-degree FOV on a CCD sensor with the maximum resolution of 72 lp/mm (9 times higher resolution than the wide FOV system). Both optical systems had a theoretical (or *nominal*) MTF contrast of about 20% or better at the Niquist frequency of their respective detectors.

1.6.4 Foveated Imaging Sensors

Another important research area in foveated imaging is the development of novel imaging sensor chips with variable resolution. This research also fits into the hardware approach, but deserves particular attention, since such sensors may play a critical role in the future development of compact hi-performance foveated imaging systems. Variable resolution sensors acquire foveated images directly at the chip level, without requiring image mosaicing at the software level. Integrating such sensors in foveated imagers can result in faster and more compact systems than in the case of the dual-sensor approach described previously.

Foveated imaging sensors can be placed in two distinct categories, as follows. The first category includes sensors with spatially variant pixel resolution across the surface of the chip similar to that of the human retina. The pixels in these retina-like sensors are smaller and more densely packed in the center of the chip and get larger towards the periphery. Just like in the human retina, the resolution varies spatially across the sensor, but remains constant over time, so these sensors can be thought of as *passive foveated sensors*. Several groups of researchers proposed various designs and implementations of such multi-resolution sensors, using both complementary metal oxide semiconductor (CMOS) and charged-coupled device (CCD) technologies [19,22]. Figure 9 shows four examples of pixel geometries and pattern architectures that have been implemented in different retina-like multi-resolution sensors.

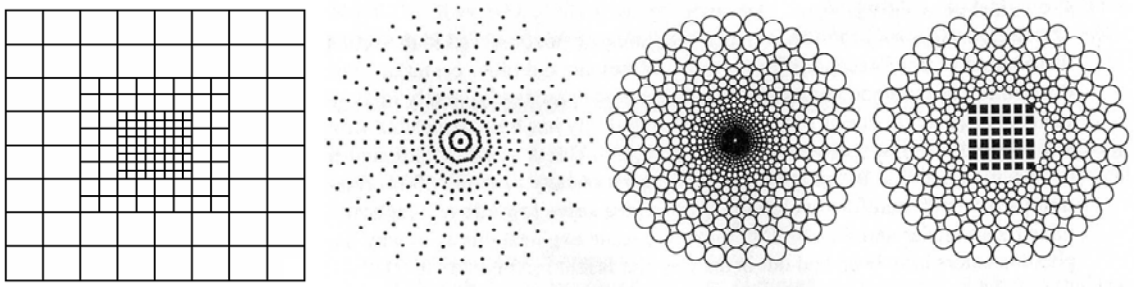

Figure 9: Various multi-resolution architectures for passive foveated sensors.

The second category of foveated imaging sensors includes uniform pixel resolution CMOS sensors with variable sampling capabilities. Such sensors can achieve foveated imaging by under-sampling pixels over the entire FOV except for the ROI, which can be sampled at a higher resolution. Under-sampling is done by combining (averaging) the photo-signals from a cluster of adjacent pixels. This sampling technique is referred to as *pixel binning*, and is commonly used in CCD sensor arrays to improve the S/N ratio and increase the frame rate at the cost of lower pixel resolution [25]. The concept of pixel binning is shown in Figure 10: 2× binning decreases resolution by a factor of 4, 2× binning decreases resolution by a factor of 9, etc. Several researchers applied the same variable sampling technique in CMOS sensors by implementing programmable pixel binning to achieve dynamic variable sampling resolution at the chip level [26]. We will call these sensors *active foveated sensors*.

In the case of the passive foveated sensors, where the resolution remains constant over time, the entire imaging system has to be mechanically reoriented to track the ROI. The active foveated sensors have the remarkable advantage of achieving dynamic foveation at

the chip level, so tracking can be done without having to reorient the entire imaging system. Therefore, active foveated sensors can be used with conventional high-performance staring wide-angle lenses or with foveated optical systems (FOS) to develop fast and compact foveated imaging systems with no mechanical moving parts.

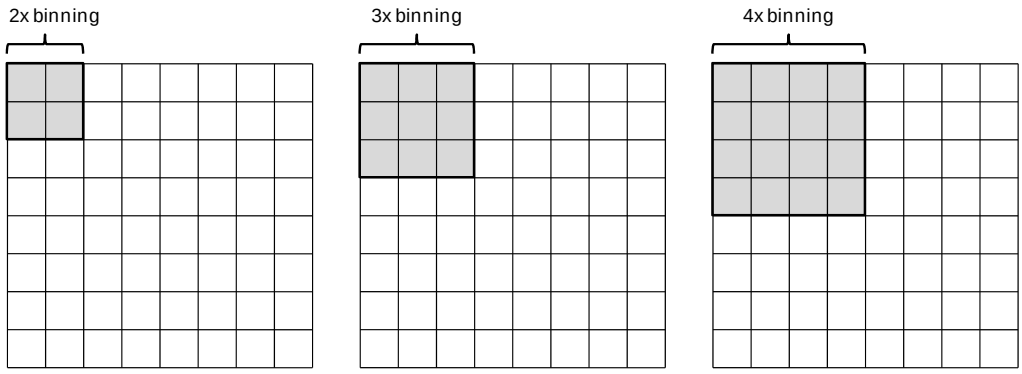

Figure 10: Examples of pixel binning.

The CMOS active-pixel sensor (APS) technology is ideal for the implementation of active foveated sensors. Unlike in CCD sensors, where all pixel charges are collected at single node, converted to voltage, buffered, and transmitted as an analog signal, in the CMOS APS technology each pixel has its own charge-to-voltage conversion, which allows random addressing of each individual pixel. Also, in CMOS sensors, amplification, noise-correction, and digitization circuitry can be implemented directly into the chip hardware. This extraordinary flexibility in the hardware design of CMOS sensors is ideal for the implementation of active foveated sensors, as foveation control algorithms can be embedded directly into the hardware design of the sensor, simplifying off-chip electronics, reducing power consumption, and increasing frame rate. Several research groups proposed and demonstrated different innovative chip design schemes and

architectures for the implementation of active foveated sensors based on CMOS APS technology [27,28].

The versatility of CMOS technology has led researchers to believe that CMOS sensors with dynamic variable resolution could potentially become the precursor technology for advanced ultra-fast high-resolution imaging in the future. Although CMOS APS technology is still in its infancy compared to the more mature CCD technology, CMOS sensors are the center of most research and development currently conducted in the imaging sensor industry. In the recent years, an increasing number of sensor and camera manufacturers have adopted CMOS technology to develop high-performance imaging sensors with pixels as small as 1.7 μm [29] and resolutions up to 50 MPixel [30].

2 OPTICAL FOVEATED IMAGING

Although several different concepts have been proposed to implement foveated imaging systems for video compression, only a few research groups have focused directly on developing methods for decreasing the size and complexity of the wide FOV optics in foveated imaging systems. The fundamental concept behind these methods is reducing the number of elements in fast wide-angle lenses by using a phase SLM to dynamically correct residual design aberrations at different points within the FOV. Throughout the dissertation, we refer to this concept as *optical foveated imaging*, in order to distinguish it from the general use of the term "foveated imaging". Also, we refer to wide-angle hybrid lenses developed using this concept as *foveated optical systems* (FOS).

This chapter begins with a background justifying the need for optical foveated imaging in order to reduce size and complexity in wide-angle foveated imaging systems. Next, a detailed review of the previous research work conducted in optical foveated imaging is covered, and different SLM options and current technologies are discussed. Finally, the motivation and objectives of this dissertation are stated and justified.

2.1 Why Optical Foveated Imaging?

Reducing the size and complexity of the optical system is a very important task in applications requiring fast (low F/#) and light-weight wide-angle optics. As discussed previously in Section 1.3, fast wide-angle lenses tend to be bulky and heavy, since complex designs with multiple elements are usually needed to correct large aberrations. Such lenses are often used in surveillance, navigation of unmanned vehicles, tracking, threat detection, and other applications where a large FOV has to be covered constantly, in different lighting conditions. The large aperture (low F/#) is generally needed to gather more light onto the sensor in outdoors applications, where poor ambient lighting can result in a low S/N ratio and therefore, poor detection capabilities.

Large aperture lenses are also required in foveated imaging systems using active foveated sensors based on CMOS APS technology. As discussed previously in Section 1.6.4, CMOS sensors can be developed to directly acquire and transmit foveated images, simplifying the off-chip electronics and image processing algorithms. In addition, compared to CCD sensors, CMOS sensors have the advantage of very low power consumption. Therefore, active foveated CMOS sensors can be used to develop compact, fast, power-efficient cameras, ideal for unmanned vehicles or space applications, where light-weight, fast data transmission, and low power consumption are critical requirements. However, CMOS sensors generally have lower sensitivities and higher noise, compared to CCD sensors. Large aperture lenses can be used to deliver more light

onto the CMOS sensor in order to increase the sensitivity of the imaging system, especially in poor lighting conditions.

Foveated imaging methods proposed by most researchers use conventional optics, and are mainly aimed at reducing the amount of transmitted data in video frames, without much concern for the relative size of the optical system. These foveation methods are usually demonstrated in a lab environment, using bench prototypes built with off-the-shelf components, and using artificial lighting. While such prototypes serve the purpose of demonstrating various innovative concepts, they can be hardly considered practical solutions for compact, high-performance wide-angle foveated imaging systems. For instance, the system proposed by Hua et al. (previously described in Section 1.6.3) was demonstrated using entirely off-the-shelf optics, and the optical systems were significantly stopped down (F/9 and F/15) in order to reduce optical aberrations [24]. Also, the light was split in half by the beam splitter, further reducing the amount of light onto the sensors. As a result, from a radiometric point of view, the F/9 wide FOV staring optical system is equivalent to an F/13 system, and the F/15 scanning system is equivalent to an F/21 system. In addition, the system is very bulky, only covers a full FOV of 45 degrees, requires additional processing hardware and software for image mosaicing, and is not power-efficient. Practically, this system can only be used in a lab environment, where size and power consumption are not a problem, and the object can be illuminated artificially. Another major disadvantage of the concept proposed by Hua et al. is that, due to the folded and asymmetrical arrangement, the aperture and FOV of the system can only be increased at the cost of a very complex optical design.

2.2 Previous and Current Research

Optical foveated imaging was first proposed a few years ago (in 2001) by Martinez et al., who described the concept of a wide-angle lens with variable resolution across the FOV, which could possibly reduce complexity and size in wide FOV optics [8]. The original concept proposed by Martinez et al. was to place a transmissive LC SLM at the pupil stop of a very compact wide-angle lens to selectively compensate aberrations at the desired points within the FOV. The proposed FOS would form an aberrated image over its wide FOV with the exception of a highly resolved ROI, which could be dynamically positioned anywhere within the FOV by adjusting the OPD pattern introduced by the SLM in order to cancel out the wavefront aberrations at the desired field point. In addition to their reduced weight and size, these hybrid lenses could be combined with foveated data compression techniques at the image processing level or with active foveated CMOS sensors (described previously in Section 1.6.4) in order to save transmission bandwidth and computational resources. The most attractive application for FOSs would be to combine them with active foveated CMOS sensors to develop compact, fast, power-efficient wide-angle foveated imaging systems, ideal for unmanned vehicles or space applications, where light-weight, fast data transmission, and low power consumption are critical requirements. However, a major drawback of this concept is the LC SLM, which limits the usability of FOSs to polarized monochromatic light.

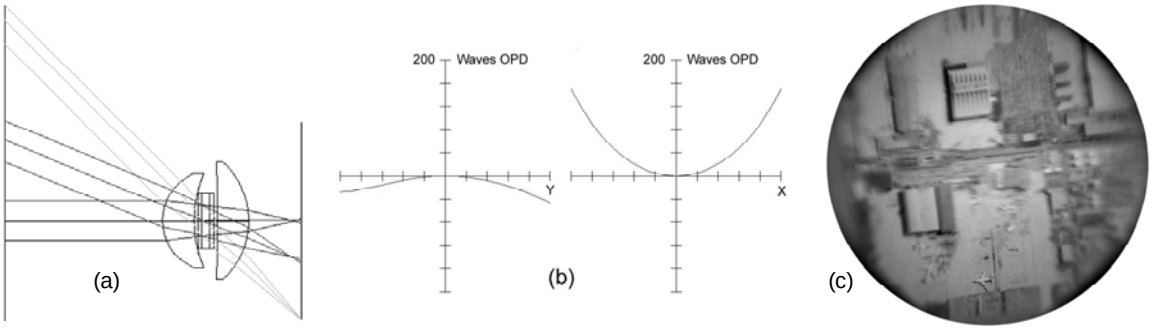

Figure 11: Foveated optical system proposed by Martinez et al. [8]. (a) Optical design layout. (b) OPD fan plots at 45 degrees without SLM correction. (c) Simulated image using ray-tracing (ignores diffractive and relative illumination effects).

The first paper on optical foveated imaging published by Martinez et al. [8] is only an introduction to the concept of using an SLM to construct an FOS. This paper also presents an example of an FOS design modeled in Zemax. The authors propose a compact wide-angle lens design using only two positive meniscus elements, symmetrically arranged about the aperture stop (front element EFL is 38 mm, and rear element EFL is 40 mm). A 2048×2048 transmissive phase SLM is placed at the stop, between the two elements, probably modeled as a 2048×2048 phase surface (authors do not provide any specific details on the SLM modeling). The layout of the optical design is shown in Figure 11 (a). The F/2.4 lens covers a full FOV of 90 degrees, and has an approximate EFL of 25 mm, which we estimated from the optical design layout (EFL not specified in the paper). We actually re-modeled this lens design starting from the optical layout provided in the paper, and using BK7 glass for both elements (see Appendix A). Distortion appears to be relatively small, as a result of the quasi-symmetrical arrangement of the elements about the aperture stop (distortion not specified in the paper). However,

this lens is extremely aberrated, as expected, with an estimate of more than 200 waves of aberration at 45 degrees (incorrectly specified in the paper as 150 waves).

Although this first paper on optical foveated imaging presents an innovative concept of a wide-angle FOS, it has several technical flaws, related to incorrect or incomplete modeling of the optical design and presentation of the analysis results. The first flaw is that the authors evaluate the maximum P-V wavefront aberration at the 45 degree field angle by considering only the one-dimensional OPD fan plot on x (shown in Figure 11 (b)), ignoring the OPD on y, which only works in the case of small field angles. By doing so, the authors erroneously claim a maximum peak-to-valley (P-V) wavefront error (WFE) of 150 waves, instead of approximately 210 waves (estimated from the two-dimensional pupil aberration). The second flaw is that the authors did not include in their model diffractive effects caused by the pixelated aperture of the SLM, neither have they commented on the possible image degradation and transmission loss due to these effects. The third flaw is ignoring the drop in the relative illumination (RI) with the field angle, due to the cosine-fourth falloff rule. This lens has no vignetting at the peripheral field angles, but the illumination also decreases proportionally with the cosine-fourth of the angle of incidence at the image plane. From the optical design layout, at the 45 degree field angle, we estimated the angle of incidence of the chief-ray at the image plane to be approximately 45 degrees (also expected from the fairly symmetrical arrangement). As a result, we estimated that the RI at the maximum field angle should drop by at least 75%. The authors failed to comment on this significant drop in illumination, which would result in a considerably lower S/N ratio towards the peripheral fields. For instance, using

ray-tracing modeling in Zemax, the authors presented the simulated image of an airport scene, where the SLM correction is applied to resolve the airplane on the bottom of the image (Figure 11 (c)). Again, it is obvious that only geometrical aberrations were considered in this ray-tracing simulation, completely ignoring the effects of diffraction and RI. However, despite the incomplete image analysis in the proposed design, the paper has the merit of introducing for the first time the concept of optical foveated imaging by using active optical elements in order to reduce size and complexity in wide-angle optical imaging systems.

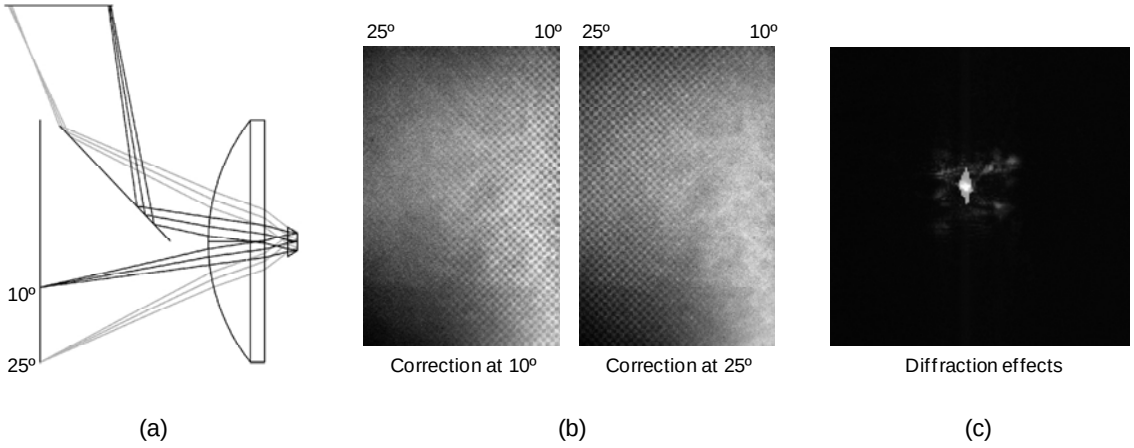

Figure 12: Optical foveated imaging demonstration by Wick et al. [31]. (a) Optical design layout. (b) Correction at 10 and 25 degrees (visible drop in the RI). (c) Correction at 25 degrees (visible diffraction effects).

A few months later, the same team of researchers published a second paper [31], describing a demonstration of the optical foveated imaging concept proposed in the first paper. The optical design proposed in the first paper turned out to be impractical because of the extremely large aberrations, requiring a 2048×2048 transmissive phase SLM

device, unavailable commercially at that time. Therefore, Wick et al. built a simple bench prototype using almost entirely off-the-shelf optical components. The experimental setup consisted of a single plano-convex lens (EFL = 50mm), with a reflective LC SLM placed at the aperture stop of the system, as illustrated by the optical design layout shown in Figure 12 (a). The SLM device (developed by Boulder Nonlinear Systems) measured 3.6×3.6 mm, had a resolution of 512×512, with 7 μm pixels, and a 77% fill factor [32]. In the case of a reflective SLM device, the image plane has to be placed such that the camera hardware does not block the FOV of the optical system. A folding mirror was used to steer the rays at a 90 degree angle and capture the image onto a large area CCD camera. The folding mirror severely limited the usable FOV to only 15 degrees, from +10 to +25 degrees. The authors did not provide any specific details on the optical properties of the system, so, in order to estimate these properties, we modeled a similar setup in Zemax following the optical layout in Figure 12 (a) (see Appendix A). From our Zemax model, we estimated that the optical system had an approximate EFL of 35 mm and was arranged in a finite conjugate configuration with a magnification of about 1.8. The aperture stop was set by the size of the SLM (3.6 mm), resulting in an effective image space F/# of 7.2. The maximum WFE was about 9 waves, assuming the focus has been adjusted for uniform distribution of the aberrations between 10 and 25 degrees. Distortion was small, due to the almost symmetrical arrangement, and the RI dropped by about 23% at the 25 degree field angle. This variation in the RI can be clearly seen in the experimental results presented in the paper, shown here in Figure 12 (b). The authors also presented results from imaging a pinhole placed at 25 degrees in the object plane, with the aberrations corrected by the SLM, shown in Figure 12 (c). Discrete diffraction orders

due to the pixelated aperture of the SLM are clearly visible. Although this setup is not a practical FOS design due to the small aperture and limited FOV, it has the value of being the first published experimental demonstration of an FOS based on the LC SLM technology. Also, this experiment revealed some of the problems related to the pixelated aperture of the SLM.

The same group of researchers has conducted further research in the area of optical foveated imaging, publishing more theoretical concepts and experimental results. For instance, Bagwell et al. proposed an FOS capable of color imaging, by adding an adjustable band-pass polarization interference filter in front of the LC SLM [33]. In this work, the authors try to overcome the monochromatic limitation, inherent in optical foveated imaging using LC SLMs, caused by applying modulo-λ correction in systems with aberrations larger than the phase stroke of the SLM (modulo-λ correction is described in more detail in the next subsection). The wavelength bands passed by the filter can be switched dynamically between red, green, and blue (RGB), and the SLM can be programmed to correct aberrations for each wavelength separately. The filter and the SLM can be synchronized such that correction at the ROI is done for each of the three wavelength bands. Such FOS would capture three images at three different wavelengths (RGB) and recombine the images at the software level to obtain a single color image. The authors claim the development a multispectral FOS at the cost of a longer image acquisition and processing time. However, this system only creates a multispectral image, and does not capture more light onto the sensor, which is the most important attribute of an imaging system used in reconnaissance and surveillance applications, where lighting

conditions can be very poor. An achromatic FOS is desirable in order to capture more light onto the sensor, which is not accomplished by the concept proposed by Bagwell et al. The proposed FOS is not an achromatic system since the three images are captured independently and then recombined at the image processing stage.

The same research group published another paper on optical foveated imaging by demonstrating a compact FOS using a transmissive SLM [34]. In this paper, Harriman et al. presented the development of a high resolution transmissive LC SLM and the integration of this device into a wide-angle FOS. The LC SLM was a 1280×1024 transmissive device specially developed for foveated imaging applications, with a pixel pitch of 15 μm and a fill factor of 56%. The transmission of the of the SLM was only 15%, including the 0-order diffraction efficiency due to the 56% fill factor, as well as losses due to absorption and Fresnel reflections. Although the authors provide detailed specifications on the SLM device and the LC, very few details are given on the wide-angle optical system. The FOS covers a full FOV of 120 degrees. A mechanical layout of the FOS showing a three-element optical design is provided (Figure 13 (a)), but without specifying important first-order optical properties of the system such as the EFL and F/#. The authors claim their FOS is more compact and covers a wider FOV compared to other prototypes built previously. However, such comparison is irrelevant without providing details on the first order properties, transmission, and image quality of the system. The FOS presented by Harriman et al. suffered significant transmission loss and image degradation due to diffraction effects in the SLM caused by a low pixel fill factor. Also, imaging results presented in the paper reveal poor image quality, a very large barrel

distortion (corrected by image processing) and a significant drop in the RI towards the peripheral FOV (Figure 13 (b)). Although this prototype is not a practical FOS due to its low transmission and poor image quality, it has value in being the first attempt of using a transmissive LC SLM into a wide FOV FOS. In addition, this work revealed important limitations in using transmissive LC SLM devices in optical systems.

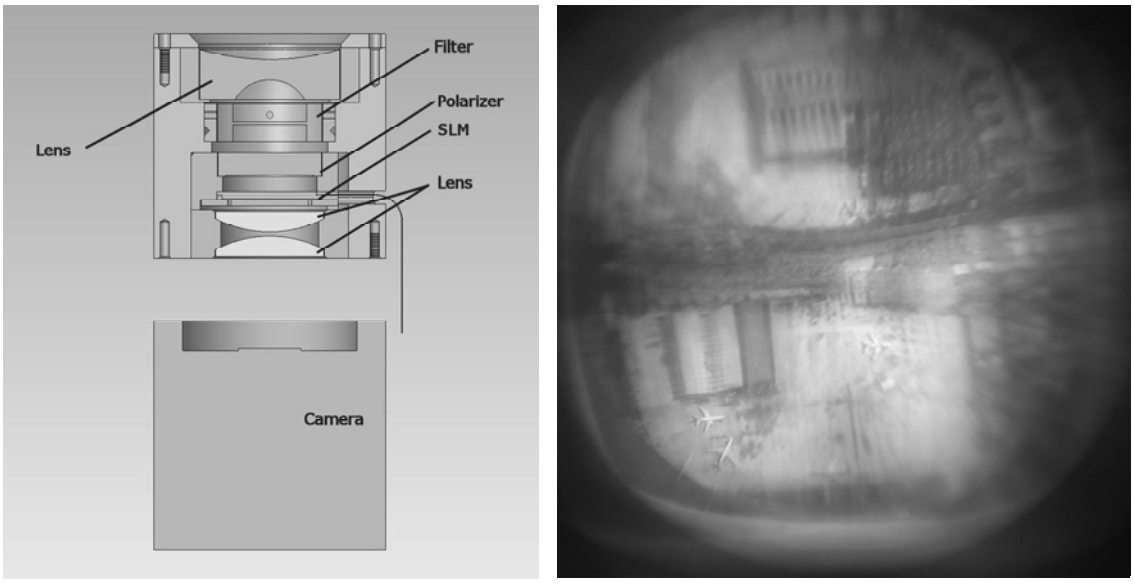

(a) (b)

Figure 13: Optical foveated imaging demonstration by Harriman et al. [34]. (a) Mechanical design layout. (b) Experimental imaging result.

The same concept used in optical foveated imaging to reduce size and complexity in wide-angle lenses was also applied by other groups of scientists to reduce complexity or improve performance in telescope and microscope systems. For example, Gruneisen et al. demonstrated a telescope with an increased FOV using an LC SLM to correct off-axis aberrations [35]. Similarly, Zhao used a micro-electro-mechanical-system (MEMS) deformable mirror (DM) to correct off-axis aberrations in a space-telescope [36]. Bagwell

et al. used a combination of MEMS DMs in a telescope to simultaneously achieve variable optical magnification (zoom) and dynamic correction of aberrations without any mechanical moving parts [37]. Potsaid et al. proposed an adaptive scanning microscope using a scanning system in conjunction with a DM to increase the FOV of a microscope [38]. Although the concept of correcting aberrations using an SLM is the same as in optical foveated imaging, the optical design arrangements in telescopes and microscopes are fundamentally different than in the case of fast wide-angle lenses. For instance, in telescope optics, the FOV and F/# are much smaller and the focal length is much longer than in the case of fast wide-angle optics. Also, microscope systems have relatively narrow FOVs. Therefore, since the term "foveated imaging" was originally used to describe wide FOV imaging systems with variable spatial resolution, most researchers have adopted the term *active optics* to refer to other hybrid imaging systems using the same concept. Both optical foveated imaging and active optics are new and promising areas in optical imaging. Currently, several research groups are conducting ongoing research and development in these novel areas.

2.3 Spatial Light Modulators for Optical Foveated Imaging

The phase SLM is the key active component enabling optical foveated imaging. Phase SLMs are reflective or transmissive devices used to control the optical wavefront by dynamically changing the OPD across the aperture. In optical foveated imaging, the SLM is placed at the aperture stop of a wide-angle lens to correct wavefront aberrations by

introducing an OPD with the same surface profile as the wavefront aberration in order to cancel the error. Therefore, the wavefront aberration of the lens has to be evaluated at discrete field points within the FOV and then translated into a lookup table to be preprogrammed into the SLM control electronics.

Two different types of phase SLMs based on two different technologies have emerged as the most commonly used devices in applications requiring wavefront correction: deformable mirrors (DM) and liquid crystal (LC) phase SLMs. This section covers an overview of typical SLM characteristics relevant to optical foveated imaging applications, and discusses advantages and disadvantages of different current SLM technologies.

2.3.1 Phase Stroke and Resolution

The maximum OPD that can be introduced by the SLM is known as the *phase stroke* of the SLM. If the wavefront aberration to be corrected exceeds the phase stroke, the correction can still be done modulo-λ [39], as shown in Figure 14. However, modulo-λ correction severely limits the wavelength range of the FOS, as diffraction efficiency drops quickly away from the center wavelength.

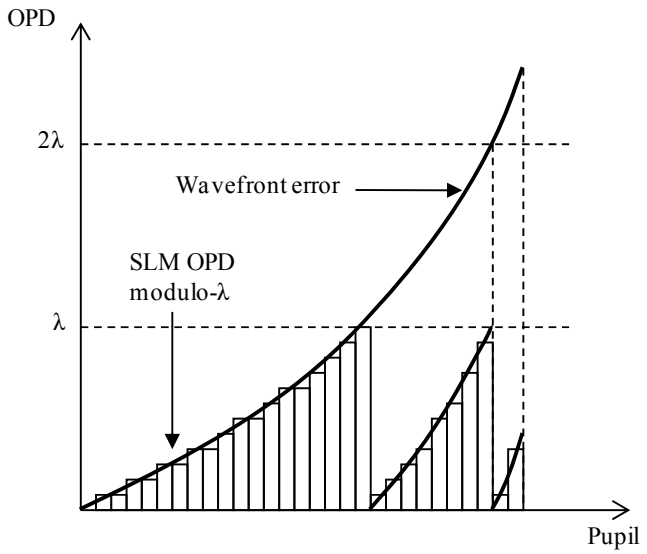

Figure 14: Wavefront correction modulo-λ.

Resolution is another important characteristic of SLMs used in foveated optical imaging, as it affects the residual wavefront error (RWFE) left after applying the SLM correction. The residual WFE is the uncorrected aberration left over after correction due to the discrete structure of the OPD introduced by the SLM. If the resolution is too low, the RWFE will affect the image quality of the FOS. The resolution of an SLM refers to the total number of elements available in the SLM (actuators or electrodes in DMs, or pixels in LC devices). However, SLMs with elements capable of piston-tip-tilt correction can reduce the RWFE more efficiently than SLMs with elements only capable of piston correction, as illustrated in Figure 15. For instance, in the case of a segmented DM with N elements ($N > 25$), the root-mean-square (RMS) RWFE with piston-only correction would be larger than with piston-tip-tilt correction by a factor equal to $\sqrt{N}$ [40,41].

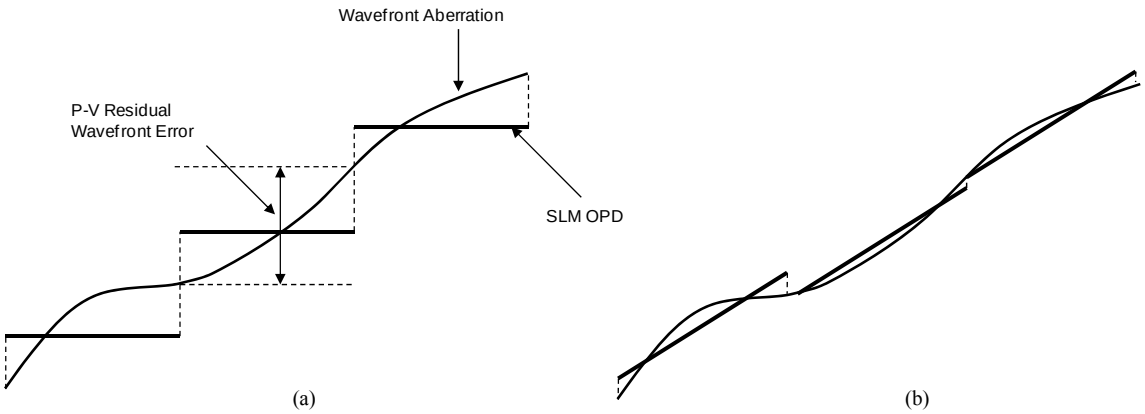

Figure 15: Residual wavefront error. (a) Piston-only correction. (b) Piston-tip-tilt correction.

2.3.2 Reflective Versus Transmissive Devices

Several research groups, including the Optical Design and Image Analysis Laboratory at CREOL, have demonstrated prototypes of FOSs using reflective SLM devices, but all these systems were unpractical, as they ended up being bulky, slow (large F/#), and covered a relatively limited FOV [31,42,43]. The main constraint was the use of a reflective SLM, which was the only commercially available solution at the time. Even now, most phase SLMs commercially available are reflective devices (DMs and LC SLMs). However, there is an ongoing research effort conducted in the area of transmissive SLMs, and several novel solutions are being investigated [34,44]. Some of these potential solutions are briefly covered in Section 2.3.5.

The problem with reflective SLM devices in optical foveated imaging applications is that they impose a 90 degree folded optical design immediately after the aperture stop, as

shown in Figure 12 (a) and Figure 37. Although achievable in slower systems with narrower FOVs, such folded designs are usually not possible and certainly not practical in the case of fast wide-angle lenses. Most of these lenses are retrofocus designs, with the stop positioned internally, somewhere between the front negative group and the back positive group, as described in Section 1.3. As a result, the diameter of the stop tends to be relatively large and the rays diverge at the stop (see for example Figure 32). Therefore, in order to fold the optical axis at 90 degrees after the stop, a rather large beam-splitting optics would be needed to capture all the rays emerging from the stop and send them through the positive group into the image plane. In the case of fast wide-angle lens designs, the position of the stop with respect to the adjacent optical elements does not allow enough space to insert such a large beam-splitter.

However, reflective SLM devices are excellent candidates for active optics in telescope systems, where narrow FOVs and large F/#s do not pose the same design problems as in the case of fast wide-angle lenses. Researchers have demonstrated the use of reflective SLMs to achieve variable optical magnification and expand the FOV in active optics based telescopes [35,36,37].

2.3.3 Deformable Mirrors

DMs are reflective SLMs commonly used in adaptive and active optics applications to control the optical wavefront [45]. They are usually made using individual flat mirror

segments (micro-mirrors) or a continuous membrane surface controlled by mechanical actuators or electrodes. The OPD is controlled by adjusting the position of the actuators or the voltage across the electrodes. Figure 16 shows the surface of a 91-element segmented DM with piston-tip-tilt capabilities, and a 4 mm aperture developed at the Sandia National Laboratories [46]. DMs have several advantages, such as large phase strokes (1 μm up to 27 μm), large fill factors (>98%), and low loss (good reflectivity). Although they have low resolutions relative to their size (usually less than 150 actuators on a 4 mm aperture), the RWFE is minimized by the continuous structure of the membrane, in membrane DMs, or by controlling the tip and tilt of each individual micro-mirror segment, in segmented DMs. Several research groups have demonstrated the use of one or more DMs to achieve active optics in telescope or microscope systems [36,37,38]. However, since DMs are by definition reflective devices, they cannot be used in practical wide-angle FOSs (as discussed in the previous section). Another disadvantage is the relatively high voltage required to control the actuators or the electrodes (up to 300 V).

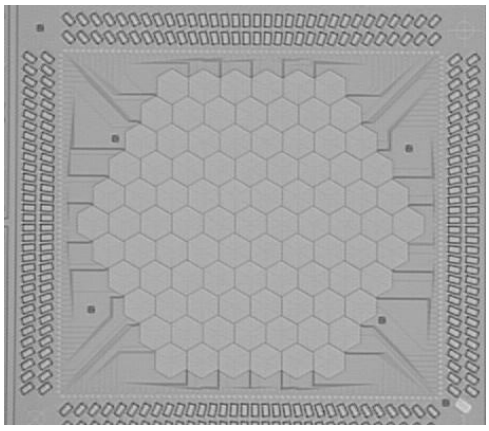

Figure 16: 91-element piston-tip-tilt DM with a 4 mm aperture [46].

2.3.4 Liquid Crystal Spatial Light Modulators

LC SLMs are another type of phase modulating devices commonly used in a variety of applications requiring wavefront control [47]. They can be reflective or transmissive, and are made by filling the space between two parallel glass plates (known as *cell*) with high-birefringence nematic LC. Figure 17 illustrates a schematic description of the basic components in a transmissive LC SLM device. The glass plates are coated on the inside with transparent electrodes. Reflective devices have an additional dielectric reflective coating over the electrodes on the bottom surface. LC SLMs can control the optical path traveled by the wavefront at each pixel in the pupil by a local change in the refractive index of the LC. The index of refraction is changed by applying a local electric field across the high-birefringence nematic LC.

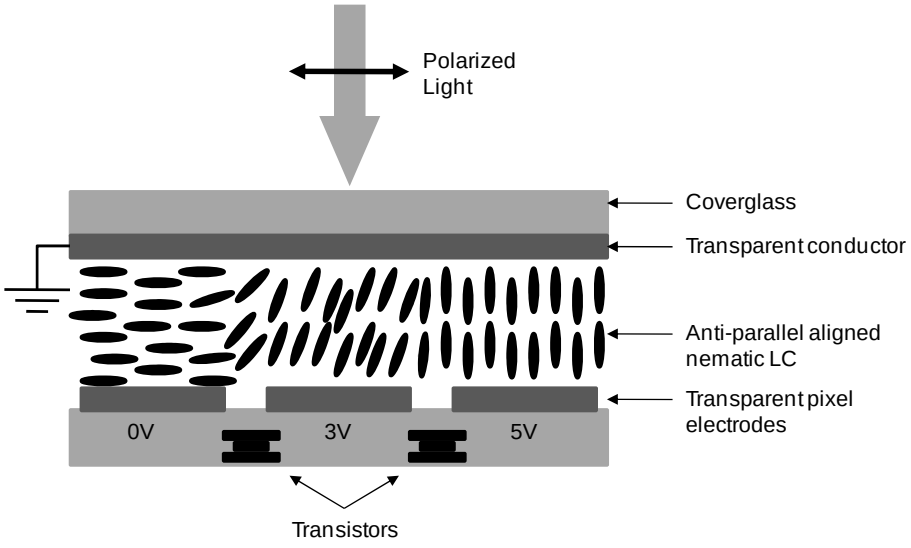

Figure 17: Operation of a transmissive LC SLM.

Nematic LCs are dielectric anisotropic liquids with elongated molecules aligned in one direction with position disorder [48]. This orientation order gives nematic LCs the optical properties of a uniaxial crystal. Nematic LCs are used in SLMs for applications where a large birefringence is needed. Light propagating through such a liquid with its polarization parallel to the molecular direction encounters the extraordinary refractive index, but if its polarization is perpendicular to the molecular direction, it encounters the ordinary index (the direction of the molecules is the direction of the optical axis). The molecules of a nematic LC normally lie parallel to the surface of the device. When an electric field is applied, the molecules tilt parallel to the field, rotating the optical axis, and therefore modulating the optical path, as shown in Figure 17. An additional advantage of nematic LC used in phase-only SLM is their good transmission of visible light.

The local OPD in LC SLMs is $\Delta n \times d$, where Δn is the index change (birefringence) in the direction of propagation, and d is the physical path length traveled by the light. The phase stroke of LC SLMs depends on the *cell gap* and the maximum refractive index change that can be induced in the LC. A large birefringence is desirable in order to decrease the cell gap, optical response time, absorption, and voltage required for the SLM operation. The optical response time is the time it takes for the device to modulate the phase from 0 to 2π. High-birefringence LCs (with Δn up to 0.4) have been developed for SLMs used in foveated imaging applications [34]. In spite of such large birefringence, the maximum phase stroke achievable practically in current SLM applications is not larger

than 2 waves in the visible region, which is not enough to correct the large aberrations in a typical fast wide-angle lens. Therefore, correction has to be done modulo-λ, significantly limiting the wavelength range of the FOS.

In an FOS, after evaluating the wavefront aberrations of the lens at discrete field angles, the pupil OPD is translated into arrays of voltages, stored in a lookup table, and preprogrammed into the control electronics of the SLM. The two-dimensional array of voltages applied to the SLM is given by $V_{i,j} = \alpha \times \left(A_{i,j} \bmod \lambda \right)$, where α is the multiplying coefficient converting OPD into voltage applied at the SLM pixel, $A_{i,j}$ is the two-dimensional array of phase values representing the wavefront error, and λ is the wavelength of the wavefront to be corrected. Since the optical phase response of the SLM is nonlinear with applied input voltage (or electric field), the coefficient α has to be calibrated over the full modulation depth such that the phase response versus applied voltage becomes a linear relationship. Also, the coefficient α has to be calibrated over the FOV of the FOS to account for the variation in OPD with the field angle. For instance, at larger field angles, the OPD in the SLM is larger than in the case of a smaller field angle. This is due to the incidence angle of the chief ray to the pupil stop of the optical system, which generally increases with the field angle.

2.3.5 Transmissive LC SLMs

We have established so far that reflective SLM devices are not a practical solution for building compact wide-angle FOSs. However, currently, there are no transmissive phase modulation devices available commercially that can be used to build a practical compact wide-angle FOS. Transmissive LC SLMs seem to be the only technology that could potentially allow practical optical foveated imaging applications in the future. Nevertheless, there are several fundamental limitations imposed by the current transmissive LC SLM technology that have to be overcome in order to allow the development of practical transmissive devices. A considerable amount of research is being currently conducted to overcome these shortcomings.

A cost effective method of building a high-resolution transmissive SLM is to modify a thin-film-transistor (TFT) transmissive LCD, which have the same structure as the SLM shown in Figure 17. These microdisplays are commonly used in projection systems, and are commercially available in relatively high resolutions (2052×1084 and even higher). Like most LCDs, they modulate intensity rather than phase. However, phase-only modulation can be achieved by changing the LC inside the cell. Another problem is that since these LCDs were developed for projection displays, the control electronics is designed for rastering and interleaving rather than individual pixel addressing. Luckily though, the TFT technology allows random pixel addressing because every pixel has its own transistor, which is somewhat similar to the CMOS technology in imaging sensors.

Therefore, addressing of individual pixels can be achieved by simply modifying the control electronics and the wiring of the device.

Recently, Harriman et al. demonstrated a high-resolution transmissive LC SLM that had been developed specifically for optical foveated imaging applications [34]. The device was developed at Boulder Nonlinear Systems (BNS) by modifying a miniature 1280×1024 transmissive liquid crystal display (LCD) for projection applications based on TFT technology. The LCD diagonal was about 24 mm, with a pixel pitch of 15 μm, and a fill factor of 56%. The cell had a gap of 5 μm and was filled with a high-birefringence nematic LC with $\Delta n = 0.4$, developed by Professor Shin-Tson Wu of the Photonics and Display Group at CREOL. The device had a phase stroke larger than one wave in the visible range, and an optical response time of 18 ms, which was several times faster than the response time of conventional SLM devices available at that time. However, the zero-order transmission of the device was only about 15%, as the 56% fill factor reduced the zero-order diffraction efficiency by about 70% and the polarizer reduced the transmission by 50%. Such a low transmission is not practical in optical systems used in imaging applications, as the amount of light onto the detector is one of the most important performance characteristics of an imaging system (the main reason for using a fast lens in an imaging system is to gather more light onto the sensor). Furthermore, the pixelated aperture of the SLM with a fill factor of 56% increased diffraction effects, significantly reducing the overall image quality of the system built using this SLM.

An important part of the transmission loss in these devices is due to the limitations imposed by the active matrix backplane technology. A drawback of the transmissive TFT technology is that a portion of the aperture of each pixel is blocked by transistors and wiring electronics, reducing the aperture ratio (or *fill factor*) of the pixel. Figure 18 shows a schematic description of the pixels in a typical transmissive LCD. In most transmissive devices, a *shadow mask* is placed over the electronics to block the light in order to prevent photoconduction. A similar problem occurs in the CMOS sensor technology, where the on-chip electronics blocks a portion of the aperture of each pixel, lowering the fill factor. This problem can be somewhat alleviated in transmissive LCDs by using a layer of micro-lenses over the cell, such that each micro-lens is lined up with a pixel in order to focus the incoming light through the clear aperture of the pixel. The same micro-lens concept is used to increase the fill factor in CMOS sensors. However, the quality of the micro-lenses in LCDs and CMOS sensors is not critical, as they are used as illumination optics rather than imaging optics, in order to ensure that most of the light gathered falls onto the active area of the pixel. This concept is not practical in the case of transmissive SLMs, because the SLM is placed at the pupil stop of the optical system, and micro-lenses would affect the wavefront. Decreasing the size of the electronics is one solution, but there are technological and theoretical limitations to how much further the size of the electronics can be shrunk. Sony introduced recently "BrightEra" [49], a new line of state-of-the-art high-resolution LCDs based on the TFT technology, in which the shadow mask width is reduced from 3.8 μm to 2.8 μm, which seems to be the current limit for the minimum mask width. Harriman et al. used a device with a 15μm pixel pitch and a 3.8 μm mask width (56% fill factor), which resulted in very poor 0-order

diffraction efficiency (almost 30%). This inherent limitation of the TFT technology affects the zero-order diffraction efficiency of transmissive SLMs, significantly reducing transmission and image quality of FOSs, which is a topic covered in more detail in the next chapters.

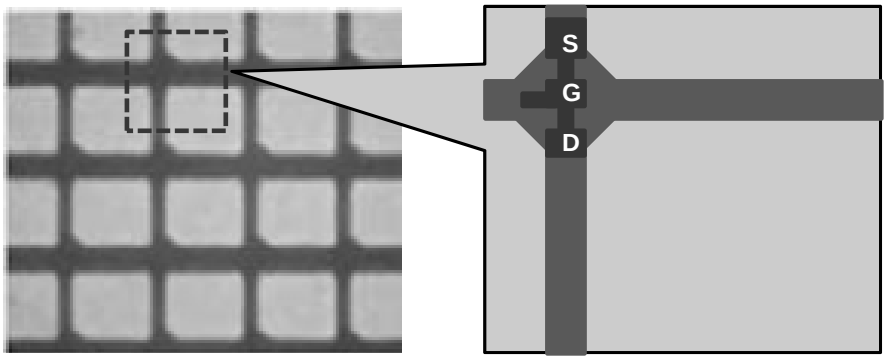

Figure 18: Transistor electronics reduces the fill factor in TFT LCDs.

Another important part of the loss in the transmissive SLM developed by Harriman et al. was due to the polarizer. LC SLMs require polarized light, as phase-only modulation can be achieved only if the polarization of the light is parallel to the molecular orientation of the LC (also known as *buffing* direction), as illustrated in Figure 17. With non-polarized light, such as natural sunlight, the polarizer alone introduces a loss of about 50%. However, several methods have been proposed to implement polarization-independent devices [44,50,51]. For instance, Lin et al. proposed a polarization-independent LC SLM by using a double-layered structure separated by thin polymer layers with orthogonal molecular alignment. This concept can possibly allow the future development of practical polarization-independent LC phase modulators.

An additional disadvantage of LC SLMs is that only small phase-strokes can be achieved practically (2π to 4π in the visible region). Larger phase-strokes are possible (up to 8π), but at the cost of a higher applied voltage or a slower response time. However, even the largest phase-stroke achievable currently in transmissive LC SLMs is not enough to correct aberrations in a practical compact wide-angle FOS. Therefore, correction has to be done modulo-λ, as shown in Figure 14, limiting the usable wavelength range due to the diffraction efficiency drop off away from the center wavelength. This monochromatic limitation imposes the use of a relatively narrow band-pass filter, reducing further the transmission of the optical system.

2.4 DARPA – Bio-Optic Synthetic Systems (BOSS) Program

The objective of the Bio-Optic Synthetic Systems (BOSS) Program funded by the Defense Advanced Projects Agency (DARPA) was to synthetically produce the components of a biologically-inspired vision system that would demonstrate a level of performance beyond standard optical imaging systems, with reduced size and complexity. This was to include a dynamically-controlled refractive index lens with a FOV approaching 180 degrees that, with a single set of optics, would be able to scan a broad area with a relatively low resolution and then focus on a target when desired.

The ultimate goal of this project was to collaborate with Sandia National Laboratories (SNL) in order to develop a very compact FOS with a FOV approaching 180 degrees.

The research effort at CREOL was lead by Professor Shin-Tson Wu, having as objective the development of high-birefringence nematic LCs to be used in compact FOSs covering very wide FOVs. The main task in the first phase of the research grant was to develop a nematic LC with $\Delta n > 0.8$. A secondary task was to demonstrate a prototype of a wide-angle FOS using an SLM based on the newly developed high-birefringence LC. The second phase of the grant included the design and synthesization of nematic LCs with an even higher birefringence, up to $\Delta n \sim 1.0$, and ultimately, the development of a second FOS prototype with a wider FOV in collaboration with SNL.

During the first phase of this project, the Optical Design and Image Analysis Laboratory under the direction of Assoc. Professor James E. Harvey was involved in the design of the FOS prototype, working closely with researchers at SNL on the optical design and analysis of the wide-angle lens. At that time, only reflective SLM devices were commercially available in high resolution, so for this first prototype, researchers from SNL decided to use an existing reflective SLM device with a resolution of 512×512 from Boulder Nonlinear Systems (BNS), and fill it with the high-birefringence nematic LC developed at CREOL during the first phase. A similar SLM device was used by Wick et al. [31] to build an earlier FOS prototype, described in Section 2.2. Our group was given the task of the optical design, with the goal of designing an FOS with a significantly wider FOV than the initial prototype demonstrated by Wick et al., which was somewhat challenging due to the use of a reflective SLM device. SNL built the FOS prototype using our optical design and the reflective SLM from BNS, filled with high-birefringence nematic LC with $\Delta n \sim 0.4$, developed at CREOL during first phase of this project. We

presented the design and experimental results of this FOS prototype at the SPIE Optics and Photonics meeting in 2005 [42]. Details on the lens design and experimental results are also presented in Chapter 4 of this dissertation.

In the second phase, research groups at CREOL, SNL, and BNS collaborated towards the development of an FOS with an even wider FOV, using a specially developed transmissive SLM device with a resolution of 1280×1024. The results of the experimental demonstration of this system were presented by Harriman et al. [34] (previously described here in Section 2.2). Although our group was not included in the funding for the second phase of this research grant, we chose to pursue our independent research in the area of optical design and analysis of wide-angle FOSs.

The independent work presented in this dissertation was motivated by the recently increasing interest in the field of foveated imaging and other related areas. Optical foveated imaging is still a very new area of research, as key technologies such as transmissive SLMs and CMOS sensors are still maturing. Recent advances in these technologies and the development of novel devices can make optical foveated imaging a very dynamic, innovative, and exciting research area. However, all research work in optical foveated imaging has focused so far only on unrealistic conceptual designs and unpractical experimental demonstrations using off-the-shelf components. Therefore, the results of the research conducted thus far are interesting, but largely inconclusive.

All FOSs demonstrated so far were built around already existing components, without much regard for the actual performance or practicality of the system. Researchers have been evaluating FOS prototypes primarily in terms of their FOV or size, which is absolutely irrelevant without considering other critical parameters such as F/#, EFL, transmission, and image quality. Therefore, the experimental research conducted so far does not provide any solid evidence on whether any of the demonstrated wide-angle FOSs have a real advantage over equivalent conventional optics.

Another important aspect overlooked thus far in the research on optical foveated imaging is the system design, analysis, and optimization of wide-angle FOSs. Studying the system design is vital to understanding design tradeoffs and current technological limitations. A thorough study of the system design, analysis, and optimization could provide clues on the best possible performance of an FOS based on the current technology and compare it to the performance of equivalent conventional optics. This study could also identify key limiting factors in the current transmissive SLM technology, such as resolution, fill-factor, transmission, and phase-stroke. It is very important to understand how these limitations affect the performance of an FOS in order to set realistic performance goals for future developments in transmissive SLM devices and wide-angle FOSs.

The main components of a foveated imaging system are the sensor, the optics, the SLM, the electronics, and the image processing software. Each component has several design parameters, which are often interrelated, and together contribute to the final performance of the imager. Table 2 lists the main design parameters related to the sensor, the optics

and the SLM. The main objective of this research work is to conduct a detailed study of the design, analysis, and optimization of wide-angle FOSs and identify limiting factors in the performance of such systems. Our research focuses mainly on the hybrid optical system, namely the optics and the transmissive SLM. Diffraction effects of the SLM on transmission, zero-order efficiency, and image quality are investigated and quantified. Tradeoffs between reducing the wavefront aberrations and reducing diffraction effects are explained and quantified. Consequences of the optical fabrication and assembly tolerances on the image quality are discussed and quantified. Realistic specifications for large format state-of-the-art CMOS sensors are used as a starting point for the optical system design. Several lens design solutions are proposed, discussing in detail performance and tradeoffs of each design. Performance of an optimized wide-angle FOS based on the current SLM technology is evaluated and compared to the performance of an equivalent conventional lens. Finally, realistic performance goals for future developments in transmissive SLM devices and wide-angle FOSs are set based on the conclusions of this research.

Table 2: Main design parameters in a foveated imaging system.

Sensor	Optics	SLM
Resolution Pixel pitch Sensitivity Noise	EFL, F/#, FOV Complexity Transmission Aberrations Relative illumination Distortion Fabrication tolerances	Resolution Pixel pitch Fill factor Transmission Response time

3 DIFFRACTION AND IMAGE ANALYSIS

The amount of signal onto the sensor and the image quality are the two most important performance characteristics of an optical imaging system. In the case of FOSs based on transmissive LC SLMs, diffraction is the main factor affecting both of these characteristics. As discussed previously in Section 2.3.5, transmissive SLM devices are based on the active matrix backplane TFT technology, where the active area of the pixels is limited by transistors and wiring electronics (Figure 18). An opaque shadow mask has to be placed over the electronics to avoid photoconduction, creating a periodic amplitude grid-like structure, which has the effect of a two-dimensional amplitude grating. Another diffractive effect is caused by the residual wavefront error (RWFE), which is the local uncorrected phase left at each pixel due to the discrete piston-only OPD of the SLM (Figure 15 (a)). The RWFE forms a periodic sawtooth-like phase structure with the same period as the amplitude grating, which has the effect of a two-dimensional blazed grating with the blaze angle slowly varying across the pupil.

The amplitude and phase diffraction caused by the pixelated structure of the transmissive LC SLMs affects the transmission, the zero-order diffraction efficiency, and the image quality (MTF) of the FOS. Figure 19 shows the diffraction pattern created by a He-Ne laser beam (633 nm) propagating through the aperture of the transmissive SLM device

developed by Harriman et al. (15 μm pixel pitch and 56% fill factor) [34]. The higher orders are clearly visible in this case, due to the relatively small fill factor. Higher diffraction orders are undesirable in imaging applications because they take energy away from the zero-order, and also fall onto the image plane as noise, affecting the contrast of the image.

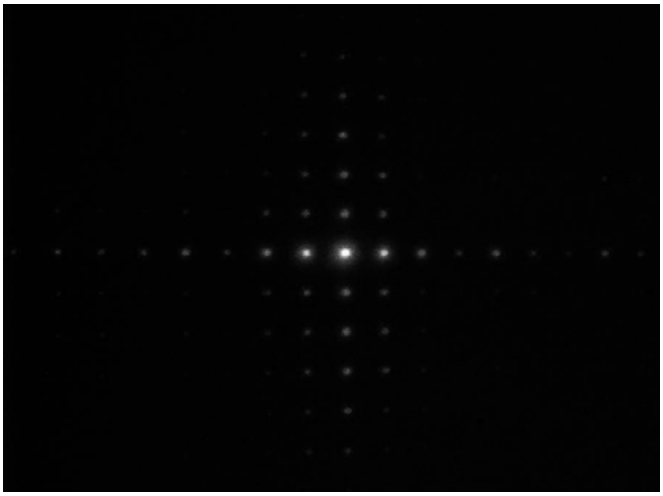

Figure 19: Diffraction pattern created by a transmissive LC SLM device [34].

This chapter analyzes diffraction phenomena occurring due to the pixelated SLM aperture, and their effect on the diffraction efficiency and the image quality of an FOS. The diffraction efficiency and MTF of an FOS are calculated from the pupil function, taking into consideration the effect of higher diffraction orders on the MTF.

3.1 The Pupil Function

The diffraction efficiency and MTF of an FOS can be calculated starting from the complex pupil function of the optical system:

$$p(x,y) = t(x,y)\, e^{j\psi(x,y)} \tag{3-1}$$

where $t(x,y)$ is the amplitude transmission function of the pupil, and $\psi(x,y)$ is the phase transmission function.

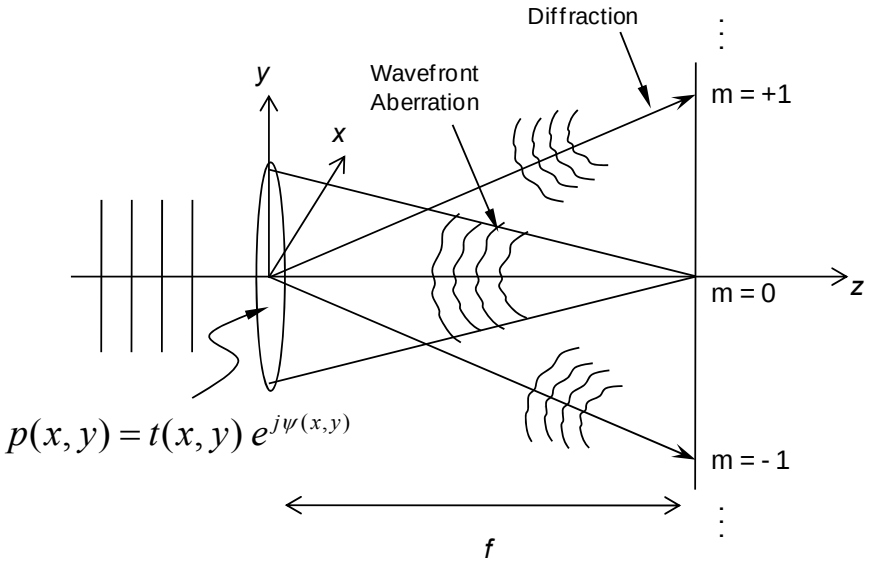

Figure 20: The effect of the pupil amplitude and phase on the diffraction and wavefront of an optical system.

Figure 20 illustrates the effect of the pupil amplitude and phase on the diffraction and wavefront aberrations of an optical system. Figure 20 also defines the coordinate system

used throughout this dissertation. The shape and magnitude of the pupil amplitude and phase determine the transmission, diffraction efficiency, and MTF of the optical system. In order to understand the effect of the SLM aperture on the performance of an FOS, we have to describe mathematically the amplitude and phase of the pupil in an FOS based on transmissive LC SLM technology.

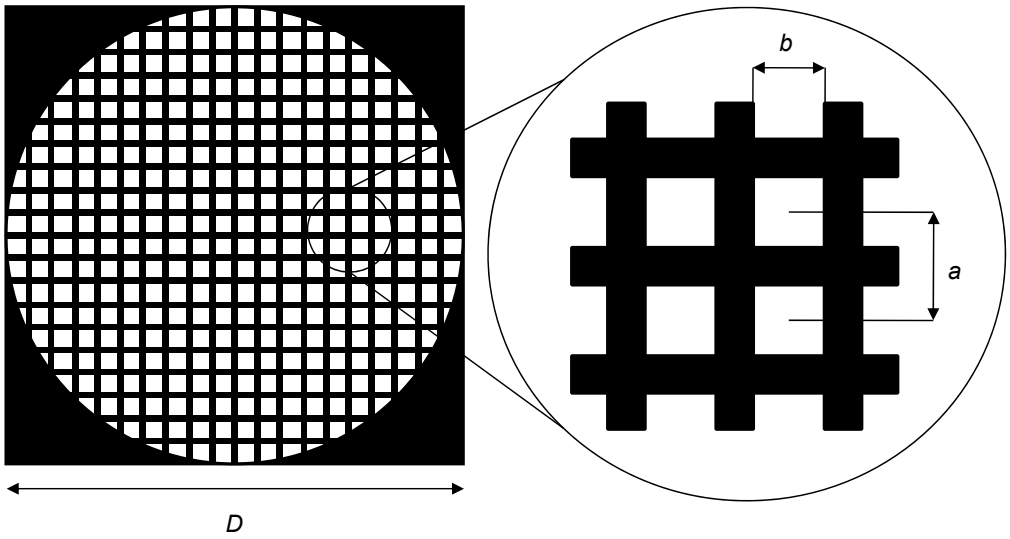

Figure 21: Amplitude transmission of the pupil of an FOS with transmissive LC SLM – *a* is the SLM pixel pitch, *b* is the pixel width and *D* is the diameter of the aperture.

Let us start first with the amplitude component of the pupil, $t(x,y)$. Figure 21 illustrates the typical geometry of the amplitude transmission in a transmissive LC SLM. The dark area represents the electronics shadow mask and the obscuration due to the circular aperture of the optics. Consider the following notation: *a* is the SLM pixel pitch, *b* is the active pixel width, and *D* is the diameter of the aperture. The fill factor is defined as the ratio between the transparent area and the total area of the pixel, so in our case, the fill factor is $(b/a)^2$. We can write the amplitude transmission function of the pupil as a

two-dimensional train of rectangle functions of width b, spaced apart by the pixel pitch a on x and y, and delimited by the circular aperture of diameter D:

$$t(x,y)=\left[\text{rect}\left(\frac{x}{b}\right)*\frac{1}{a}\text{comb}\left(\frac{x}{a}\right)\right]\left[\text{rect}\left(\frac{y}{b}\right)*\frac{1}{a}\text{comb}\left(\frac{y}{a}\right)\right]\text{circ}\left(\frac{\sqrt{x^2+y^2}}{D/2}\right) \tag{3-2}$$

Now, let us look at the phase component, $\psi(x,y)$. In the case of an FOS, the wavefront aberration at the ROI, $W(x,y)$, is corrected by the SLM, with the exception of the residual wavefront error (RWFE), which is the uncorrected aberration left at each pixel after the SLM correction is applied, as illustrated in Figure 15 (a). The RWFE is a consequence of the discrete piston-only OPD of the transmissive LC SLM. For a large number of pixels ($N \times N$, $N > 32$), the local RWFE at each pixel can be approximated by a wavefront tilt on x and y, as shown in Figure 22. The local P-V RWFE on x and y at the pixel $[i, j]$ is given by the local slope of the wavefront aberration and the pixel pitch of the SLM:

$$\begin{aligned} RWFE_{P\text{-}Vx}[i,j] &= a\times\left|\frac{\partial W(x,y)}{\partial x}\right|_{x=x_i,y=y_j} \\ RWFE_{P\text{-}Vy}[i,j] &= a\times\left|\frac{\partial W(x,y)}{\partial y}\right|_{x=x_i,y=y_j} \end{aligned} \tag{3-3}$$

where x_i and y_i are the pupil coordinates at the pixel $[i, j]$.

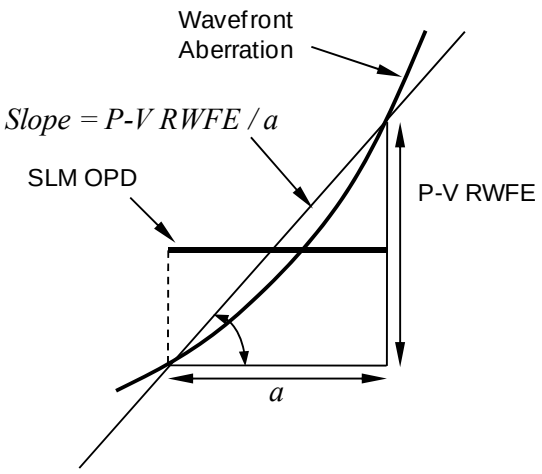

Figure 22: The local RWFE at each pixel can be approximated by a wavefront tilt.

After the wavefront aberration is corrected by the SLM, the transmitted pupil phase at the ROI will have the shape of a two-dimensional periodic sawtooth function, which has the effect of a *blazed transmission phase grating*, with the period *a*, and the *blaze angle* given by the slope of the wavefront aberration. The blaze angle will follow a similar variation across the pupil as the slope of the wavefront aberration. The transmitted phase of an FOS with an SLM resolution of $N \times N$ at the wavelength λ can be written as

$$\psi(x,y) = \frac{2\pi}{\lambda} \sum_{i,j=1}^{N} \left[\left. \frac{\partial W(x,y)}{\partial x} \right|_{\substack{x=x_i \\ y=y_j}} x + \left. \frac{\partial W(x,y)}{\partial y} \right|_{\substack{x=x_i \\ y=y_j}} y \right] t(x,y) \tag{3-4}$$

Figure 23 shows a schematic one-dimensional plot of the pupil amplitude and phase of an FOS based on transmissive LC SLMs after correcting the wavefront aberration at the ROI. The amplitude, $t(x)$, has a value of one at the regions where the SLM is transparent and zero where the SLM is opaque. The phase, $\psi(x)$, looks like a blazed grating with the

blaze angle following the variation of the slope of the corrected wavefront aberration, $W(x)$.

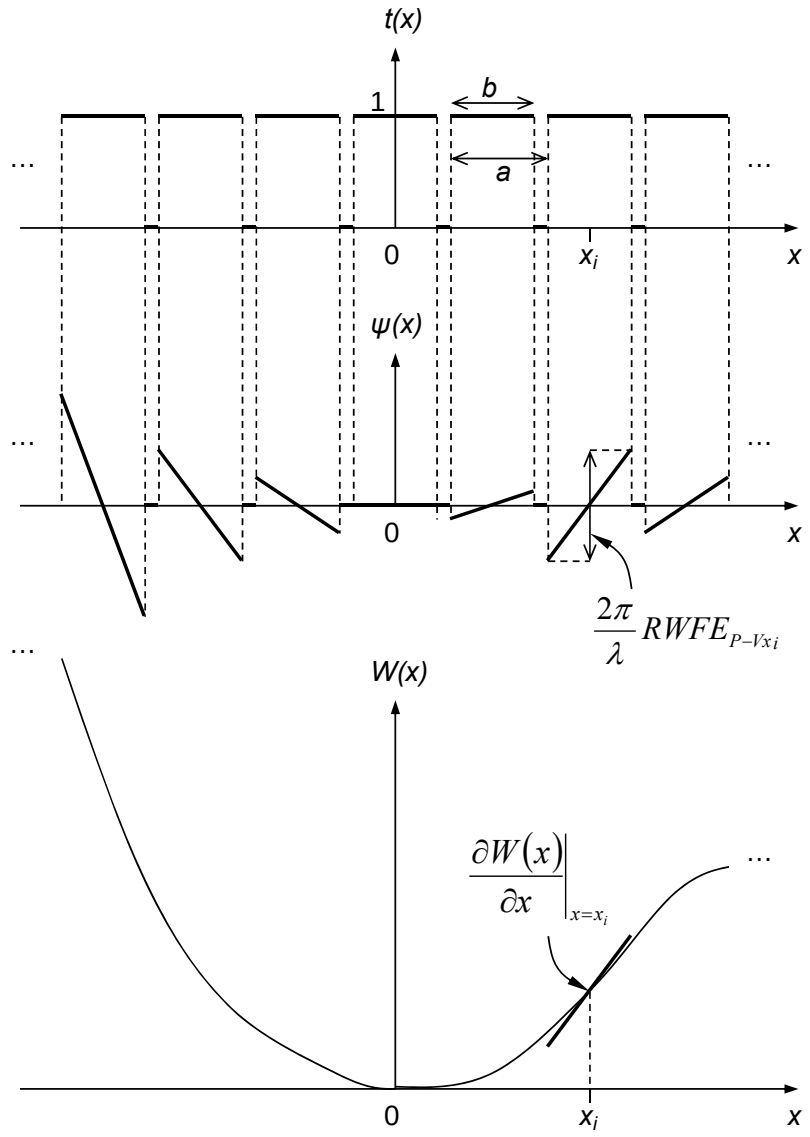

Figure 23: One-dimensional pupil amplitude and phase transmission plots, $t(x)$ and $\psi(x)$, after correcting the aberration $W(x)$ (period exaggerated for clarity).

3.2 Diffraction Efficiency

The amount of signal onto the sensor in an optical system depends on the aperture, F/#, transmission, and diffraction efficiency of the system. In FOSs based on transmissive LC SLMs, a significant loss in signal is caused by the zero-order diffraction efficiency. The periodic structure of the pupil amplitude and phase produces a grating effect, creating higher diffraction orders and limiting the zero-order efficiency. In this section, the diffraction efficiency at the ROI of an FOS with an SLM resolution of $N \times N$ is derived as a function of a, b, and the P-V RWFE on x and y at every pixel $[i, j]$, as defined in the previous section.

Note that, in all equations in this chapter and subsequent chapters, the symbols D, a, and b refer to the physical dimensions in the stop scaled to the size of the entrance pupil. So, if the entrance pupil of the optical system is not the same as the stop, the physical dimensions have to scaled by the magnification of the stop in the object space, which is given by the ratio between the entrance pupil diameter and the stop diameter:

$$M_{obj} = \frac{D_{EP}}{D_{STOP}} \tag{3-5}$$

The efficiency of each diffraction order can be calculated from the power spectral density (or *point spread function*) in the image plane, which is the magnitude squared of the field. The field in the image plane is given by the Fourier transform of the field in the pupil [52]. As a result, the diffraction efficiency can be calculated starting from the complex

pupil function, $p(x,y)$, which completely describes the amplitude and phase of the field in the pupil. In order to simplify calculations, we can start by considering a few reasonable assumptions, and then generalize the end results. If $D >> a$, we can consider the case of an infinite aperture, which eliminates the term $\mathrm{circ}\left(\frac{\sqrt{x^2+y^2}}{D/2}\right)$ in Equation (3-2). Also, we need only to derive the one-dimensional diffraction in the paraxial case. Furthermore, we can consider the particular case where the wavefront aberration to be corrected at the ROI is only a tilt on x with the slope equal to $\frac{RWFE_{P-V}}{a}$. In this particular case, after the wavefront aberration at the ROI is corrected by the SLM, the pupil becomes a transmission phase grating with a constant blaze angle, so the one-dimensional pupil function on x can be written as

$$p(x) = \left[\mathrm{rect}\left(\frac{x}{b}\right) * \frac{1}{a}\mathrm{comb}\left(\frac{x}{a}\right)\right] \exp\left(j\frac{2\pi}{\lambda}\frac{RWFE_{P-V}}{a}x\right) \tag{3-6}$$

Assuming monochromatic plane waves coming from a point source at infinity, the field in the image plane is given by the Fourier transform of the pupil, $p(x)$:

$$P(\xi) = \frac{b}{a}\,\mathrm{sinc}\left[b\left(\xi - \frac{RWFE_{P-V}}{\lambda\, a}\right)\right] a\,\mathrm{comb}(a\xi) \tag{3-7}$$

where $\xi = \frac{x}{\lambda f}$ is the spatial frequency, λ is the wavelength of the incident light, and f is the focal length of the optical system. The power spectral density in the image plane is given by the magnitude squared of the field:

$$\left|P(\xi)\right|^2 = \left(\frac{b}{a}\right)^2 \operatorname{sinc}^2\left[b\left(\xi - \frac{RWFE_{P-V}}{\lambda\, a}\right)\right] a^2 \operatorname{comb}^2(a\xi) \tag{3-8}$$

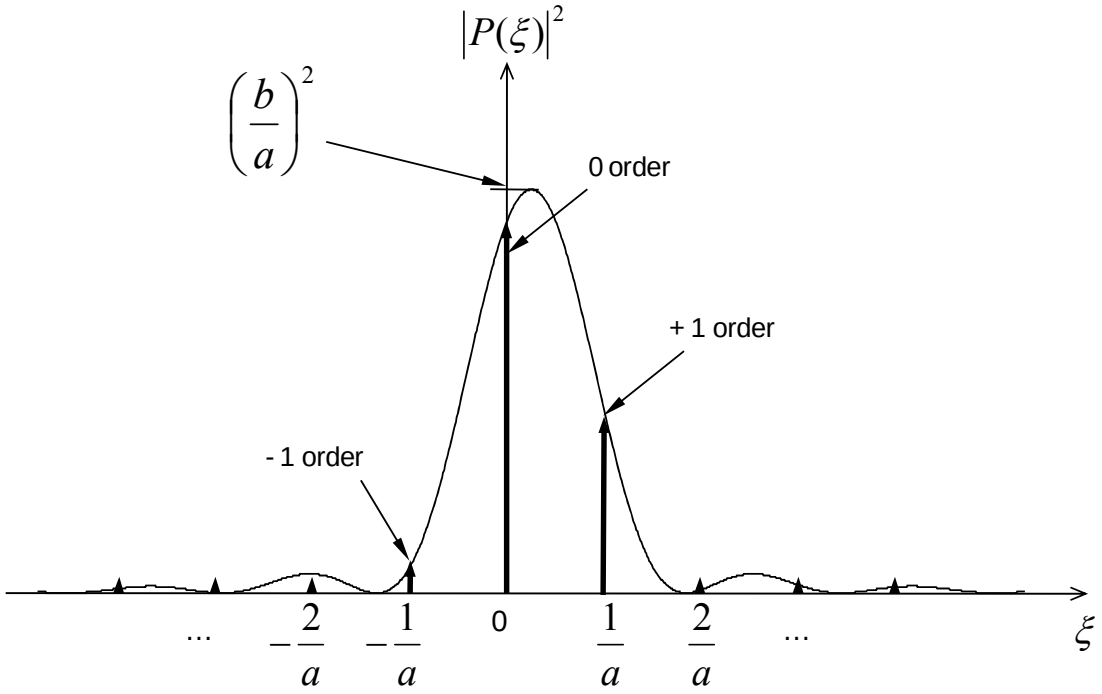

Figure 24: Power spectral density of a one-dimensional blazed grating.

The term $a^2 \operatorname{comb}^2(a\xi)$ in Equation (3-8) is an array of *delta* functions of height 1, spaced by $\frac{1}{a}$ along ξ. This array of delta functions is multiplied by the term

$\left(\frac{b}{a}\right)^2 \text{sinc}^2\left[b\left(\xi - \frac{RWFE_{P-V}}{\lambda\, a}\right)\right]$, which is a sinc^2 function of height $\left(\frac{b}{a}\right)^2$, offset by $\frac{RWFE_{P-V}}{\lambda\, a}$, with zeros at $\pm\frac{1}{b} + \frac{RWFE_{P-V}}{\lambda\, a}$, $\pm\frac{2}{b} + \frac{RWFE_{P-V}}{\lambda\, a}$, … The one-dimensional power spectral density in the image plane is schematically plotted in Figure 24, in the case where $b > \frac{a}{2}$ and $RWFE_{P-V} < \lambda$.

The diffraction angles are determined by the locations of the delta functions:

$$\beta_m = \sin^{-1}\left(\sin\theta + \frac{m\lambda}{a}\right) \tag{3-9}$$

where β_m is the diffraction angle of the m-order with respect to the optical axis in object space, and θ is the field angle in object space. The efficiency of each diffraction order is given by the height of the delta function at the corresponding spatial frequency. From Equation (3-8), the m-order diffraction efficiency relative to the total incident light is given by

$$\sigma_m = \left|P\left(\xi = \frac{m}{a}\right)\right|^2 = \left(\frac{b}{a}\right)^2 \text{sinc}^2\left[\frac{b}{a}\left(m - \frac{RWFE_{P-V}}{\lambda}\right)\right] \tag{3-10}$$

Notice that, for a given grating period, a, the blaze angle (RWFE) only has the effect of shifting the distribution of the efficiency among diffracted orders, and does not affect the

diffraction angles or the total transmission. For instance, if $RWFE_{P-V} = 0$, the highest diffraction efficiency will be in the zero-order. If $RWFE_{P-V} = \lambda$, the highest efficiency will be in the +1-order.

So, the diffraction angles in an FOS depend on the SLM pixel pitch, and the total transmission and the diffraction efficiency in each order depend on the pixel fill factor and the RWFE. However, the RWFE in an FOS varies across the pupil on *x* and *y*, depending on the shape of the wavefront aberration and the OPD introduced by the SLM. Therefore, in order to calculate the diffraction efficiency for any wavefront aberration, the result in Equation (3-10) has to be generalized for a two-dimensional pupil with variable RWFE across *x* and *y*. Assuming an FOS with a high-resolution SLM, the RWFE varies relatively slowly over several pixels, so for each order, (m_x, m_y), we can define the *local two-dimensional diffraction efficiency* at every pixel $[i, j]$ as the product between the local diffraction efficiencies on *x* and *y*:

$$\sigma_{m_x,m_y}[i,j] = \left(\frac{b}{a}\right)^4 \operatorname{sinc}^2\left[\frac{b}{a}\left(m_x - \frac{RWFE_{P\text{-}Vx}[i,j]}{\lambda}\right)\right] \operatorname{sinc}^2\left[\frac{b}{a}\left(m_y - \frac{RWFE_{P\text{-}Vy}[i,j]}{\lambda}\right)\right] \quad (3\text{-}11)$$

where m_x and m_y are the diffraction orders on *x* and on *y*, and $RWFE_{P\text{-}Vx}[i,j]$ and $RWFE_{P\text{-}Vy}[i,j]$ are the P-V RWFE values on *x* and on *y* at the pixel $[i, j]$, as defined in Equation (3-3). The term $\left(\frac{b}{a}\right)^4$ in Equation (3-11) represents the diffraction efficiency due to the amplitude part of the pupil function (the electronics shadow mask), and the

sinc^2 terms represent the local diffraction efficiency on x and y caused by the phase part of the pupil function (the RWFE). The term $\frac{b}{a}$ in the argument of the two sinc^2 functions represents the truncation factor of the local P-V RWFE due to the limited active pixel width. Assuming an SLM resolution of $N \times N$, the overall diffraction efficiency for any order can be calculated as the root-mean-square (RMS) across the entire pupil:

$$\sigma_{m_x,m_y} = \sqrt{\frac{\sum_{i,j=1}^{N} \left(\sigma_{m_x,m_y}[i,j]\right)^2}{N^2}} \tag{3-12}$$

The total transmission of all diffraction orders combined is equal to the fill factor:

$$\sigma_{total} = \left(\frac{b}{a}\right)^2 \tag{3-13}$$

Note that, when calculating the diffraction efficiency for each order in Equation (3-11), the total transmission is already included in the term $\left(\frac{b}{a}\right)^4$.

The distribution of the diffraction efficiency among higher orders at the ROI depends on the shape and symmetry of the wavefront aberration corrected at the ROI. For instance, if the wavefront aberration is rotationally symmetric about the optical axis, such as the aberration of an optical system on-axis, the diffraction efficiency will be distributed evenly among the symmetrical orders about the origin and about x and y axes

($\sigma_{\pm m,\pm m} = \text{constant}$ and $\sigma_{\pm m,0} = \sigma_{0,\pm m}$). In the case of non-symmetrical aberrations, the diffraction efficiency is distributed according to the overall slope of the wavefront aberration across the pupil. Figure 25 shows the relative distribution of the diffraction efficiency at the ROI, with $\frac{b}{a} = 0.64$ and $\lambda/10$ P-V RWFE on *x* and *y*, after correcting a wavefront tilt. In this example, the total transmission of all diffracted orders is 40% and the zero-order diffraction efficiency is only 9%. Also, notice that $\sigma_{-1,-1} \approx 0$.

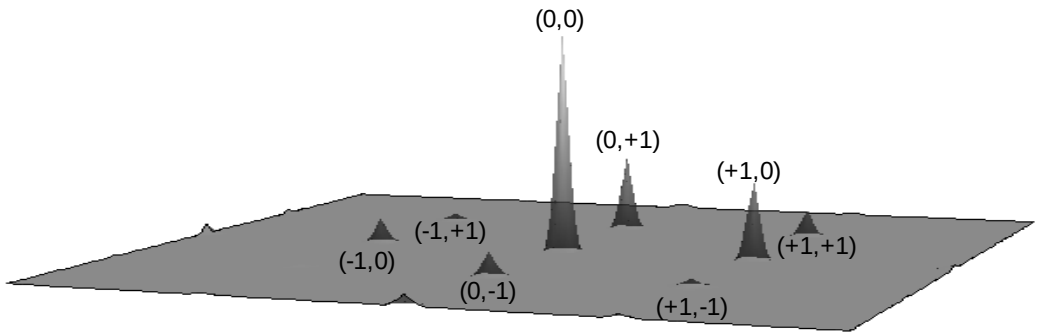

Figure 25: Example of diffraction efficiency distribution with $\frac{b}{a} = 0.64$ and $\lambda/10$ P-V RWFE on *x* and *y*, after correcting a wavefront tilt.

3.3 Modulation Transfer Function

The image quality of an optical system is affected mainly by three factors: diffraction, aberrations not corrected in the optical design, and additional aberrations caused by fabrication and assembly errors. In an FOS, wavefront aberrations at the ROI are corrected by the SLM, with the exception of the RWFE. If the RWFE is very small (diffraction limited), diffraction becomes the dominant factor affecting the image quality at the ROI. This section covers a derivation of the diffraction MTF of FOSs based on transmissive LC SLMs. The effect of higher diffraction orders on the MTF contrast is also covered in this section.

The modulation transfer function (MTF) is a suitable tool for quantifying the image quality of an optical system, because it includes both diffraction and aberrations effects. The MTF of an optical system fully characterizes the resolving capabilities of the optics, and is defined as the contrast of the image relative to the contrast of the object, as a function of the spatial frequency. The MTF of the optics can be conveniently multiplied by the MTF of the other components in the imaging system, such as the MTF of the sensor and the MTF of the electronics, in order to obtain the overall MTF of the electro-optical imaging system [53].

Figure 26 shows some useful and convenient relationships between the pupil function, $p(x,y)$, the field in the image plane, $P(\xi,\eta)$, the point spread function (PSF), $PSF(x,y)$, the optical transfer function (OTF), $OTF(\xi,\eta)$, and the modulation transfer

function (MTF), $MTF(\xi,\eta)$. The OTF is the normalized autocorrelation of the pupil function, with $x = \xi\lambda f$ and $y = \eta\lambda f$, and the MTF is the magnitude of the OTF. The OTF can also be obtained from the Fourier transform of the PSF. The PSF is the magnitude squared of the field in the image plane, with $\xi = \frac{x}{\lambda f}$ and $\eta = \frac{y}{\lambda f}$, and the field is given by the Fourier transform of the pupil function.

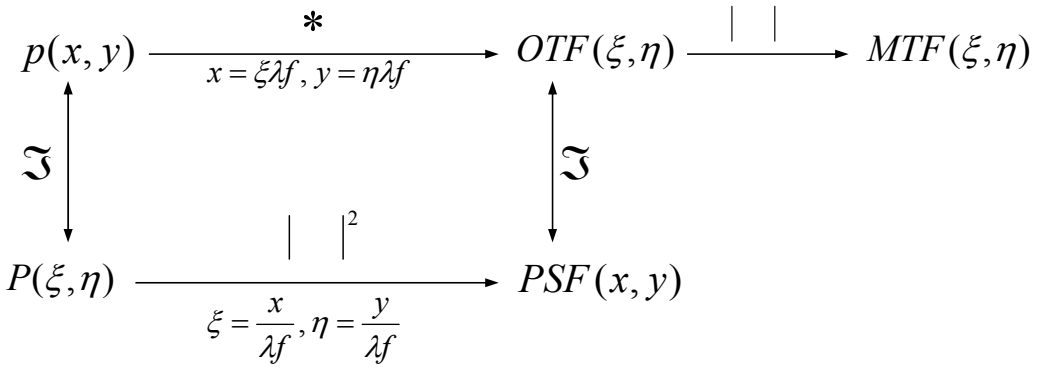

Figure 26: Relationships between pupil function, field, PSF, OTF, and MTF.

3.3.1 Diffraction MTF

To simplify calculations, let us assume that the RWFE at the ROI is very small, and has no significant effect on the MTF of the FOS at the ROI. Also, if $D >> a$, the effect of the aperture of diameter D on the MTF is a function that varies very slowly compared to the effect of the SLM amplitude transmission. Therefore, we can first derive the diffraction MTF of the SLM amplitude, and then multiply the result by the MTF of the aperture. The SLM amplitude transmission on x can be written as

$$p_{SLM}(x) = \text{rect}\left(\frac{x}{b}\right) * \frac{1}{a}\text{comb}\left(\frac{x}{a}\right) \tag{3-14}$$

The field in the image plane is given by the Fourier transform of the pupil:

$$P_{SLM}(\xi) = b\ \text{sinc}(b\xi)\,\text{comb}(a\xi) \tag{3-15}$$

The PSF is the magnitude squared of the field in the image plane, with $\xi = \frac{x}{\lambda f}$:

$$PSF_{SLM}(x) = \left|P(\xi)\right|^2_{\xi=\frac{x}{\lambda f}} = \left(\frac{b}{a}\right)^2 \text{sinc}^2\left(\frac{x}{\lambda f / b}\right)\ a^2\,\text{comb}^2\left(\frac{x}{\lambda f / a}\right) \tag{3-16}$$

The OTF is the Fourier transform of the PSF, normalized to the total area under the PSF. From the *central ordinate theorem* of the Fourier transform theory, the area under the PSF is equal to the Fourier transform of the PSF at $\xi = 0$. Since the OTF does not have a phase component in this case, the MTF is equal to the OTF. So the MTF of the SLM amplitude transmission can be written as

$$MTF_{SLM}(\xi) = \left|\frac{\Im\{PSF(x)\}}{\Im\{PSF(x)\}\big|_{\xi=0}}\right| = \text{tri}\left(\frac{\xi}{b/\lambda f}\right) * \left(\frac{\lambda f}{a}\right)^2 \text{comb}^2\left(\frac{\xi}{a/\lambda f}\right) \tag{3-17}$$

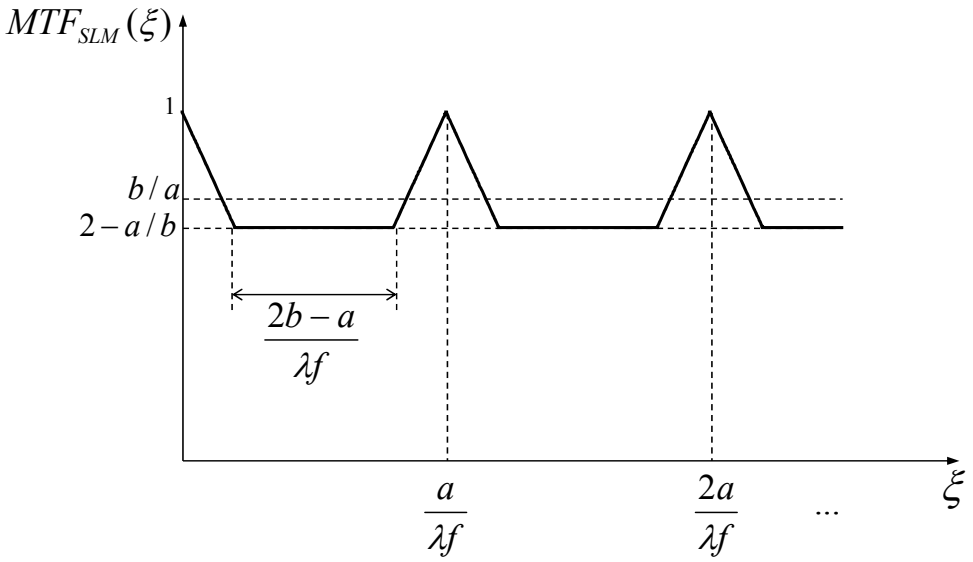

Figure 27: Diffraction MTF of the SLM amplitude is a sawtooth function with the period $a/\lambda f$ and an average contrast of b/a.

The expression in Equation (3-17) is a train of triangle functions spaced apart by $\frac{a}{\lambda f}$, forming a sawtooth function with the period $\frac{a}{\lambda f}$ and an average contrast of $\frac{b}{a}$. A schematic plot of this expression is shown in Figure 27. The flat portion of this sawtooth has a width of $\frac{2b-a}{\lambda f}$ at a contrast of $2-\frac{a}{b}$. There are three possible cases. If $\frac{a}{b}<2$, the sawtooth would look like the plot in Figure 27. If $\frac{a}{b}=2$, the triangles would go all the way down to zero, and then go back up to 1 periodically. If $\frac{a}{b}>2$, the sawtooth would stay flat at zero between each triangle for a portion of width $\frac{a-2b}{\lambda f}$ before going back up to 1. It is obvious that the last two cases are not practical for imaging applications.

Actually, if the contrast of the flat portion, $2-\frac{a}{b}$, is not greater than 0.5, the SLM is not suitable for optical foveated imaging, as the MTF would reach a low value periodically, creating artifacts in the image.

The diffraction MTF of the FOS can be calculated by multiplying the MTF of the SLM amplitude by the MTF of the aperture. Assuming $2-\frac{a}{b}>0.5$ and $D>>a$, we can approximate the high-frequency sawtooth in Equation (3-17) by its average value, $\frac{b}{a}$. As a result, the diffraction MTF of an FOS can be written as

$$MTF_{diffr}(\xi)=\left(\frac{b}{a}\right)\times MTF_{aperture}(\xi) \tag{3-18}$$

Equation (3-18) is valid for any aperture shapes, as long as all the features of the aperture are significantly larger compared to the SLM pixel pitch. If the aperture has any small features comparable in size to the pixel pitch, the diffraction MTF has to be calculated as the convolution between the expression for the MTF of the SLM amplitude from Equation (3-17) and the expression for the MTF of the aperture. In our case, we assumed a circular aperture of diameter *D*, so the MTF of the aperture is given by the following expression:

$$MTF_{aperture}(\xi) = \frac{2}{\pi}\left[\cos^{-1}\left(\frac{\xi}{\xi_{cutoff}}\right) - \left(\frac{\xi}{\xi_{cutoff}}\right)\sqrt{1-\left(\frac{\xi}{\xi_{cutoff}}\right)^2}\right] \tag{3-19}$$

where $\xi_{cutoff} = \frac{D}{\lambda f}$ is the cutoff frequency [53]. Figure 28 shows the diffraction MTF of a circular aperture.

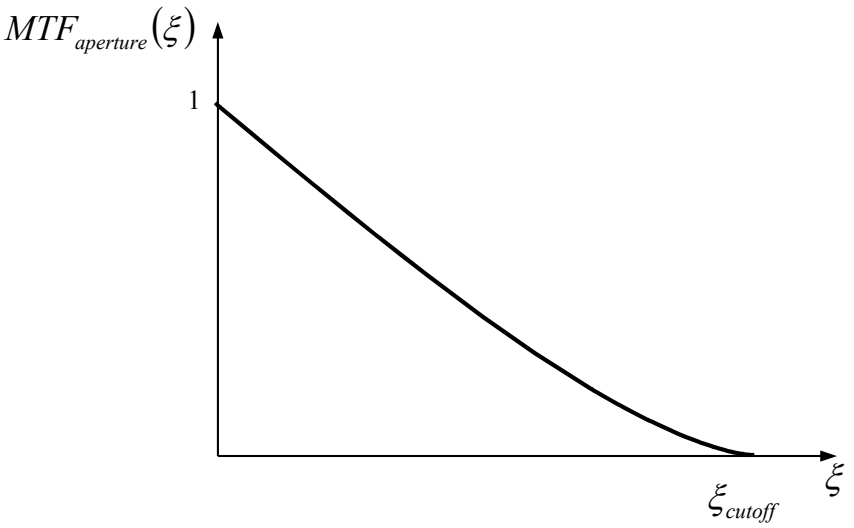

Figure 28: Diffraction MTF of a circular aperture.

The diffraction MTF of an FOS with a circular aperture is schematically plotted in Figure 29 (the period of the sawtooth is exaggerated for clarity). So, in practical optical foveated imaging applications, where $\xi_{cutoff} >> \frac{a}{\lambda f}$ and $2 - \frac{a}{b} > 0.5$, the diffraction MTF of an FOS can be approximated by the diffraction MTF of the aperture, washed down by the multiplication factor $\frac{b}{a}$.

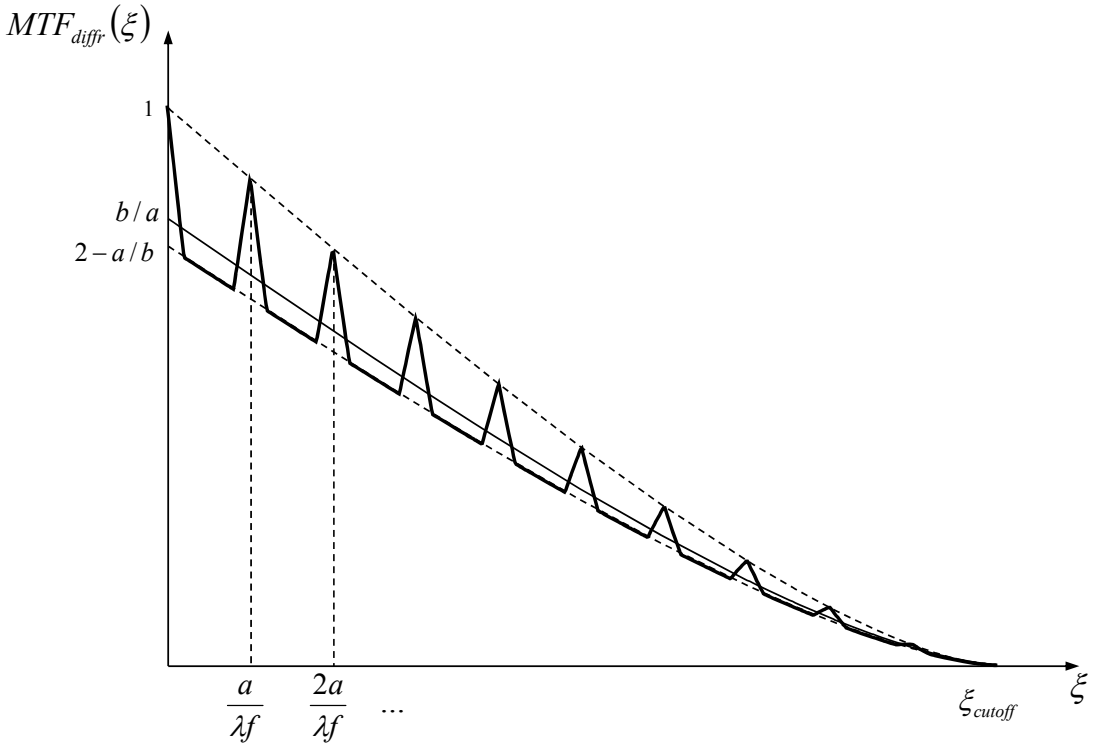

Figure 29: Diffraction MTF of an FOS.

3.3.2 Effect of Higher Diffraction Orders on MTF

As discussed in Section 3.2, a portion of the light transmitted through the SLM will end up in higher diffraction orders. Since FOSs image extended objects, the diffraction MTF will be further affected by the higher orders from other field angles falling onto the image plane. The images formed by the higher diffraction orders will superimpose onto the zero-order image, creating shifted "ghost" images of the extended object, equally spaced on *x* and *y*. This section covers a method to estimate the drop in the MTF due to these parasitical images created by higher diffraction orders as a function of *a*, *b*, and the RMS zero-order diffraction efficiency at the ROI, $\sigma_{0,0}$, as defined in Equation (3-12).

From Equation (3-9), the angular increment between diffraction angles on x and y, $\Delta\beta$, can be approximated by

$$\Delta\beta \approx \frac{\lambda}{a} \tag{3-20}$$

Therefore, the zero-order image at the ROI with the field angle (θ_x, θ_y) is affected by a superposition of higher diffraction orders, (m_x, m_y), each order coming from a different field angle, $\left(\theta_x - \frac{m_x\lambda}{a}, \theta_y - \frac{m_y\lambda}{a}\right)$, where $m_x, m_y = 0, \pm 1, \pm 2, \ldots$, with $m_x = m_y \neq 0$.

In a practical FOS, $a >> \lambda$, so the angular increment between diffraction angles, $\Delta\beta$, is small relative to the FOV of the FOS. In this case, the wavefront aberration of the optical system and the diffraction efficiency, σ_{m_x,m_y}, can be considered constant over a small rectangular FOV centered at the ROI and covering $\pm\Delta\beta$ on x and y. Also, in a practical FOS, most of the transmitted light goes into the zero-order, and most of the remaining light goes into the eight orders closest to the zero-order. As a result, the total amount of light diffracted from other field angles falling onto the zero-order at the ROI can be approximated by the total diffraction efficiency of the higher orders at the ROI:

$$\sigma_{\substack{higher \\ orders}} \approx \left(\frac{b}{a}\right)^2 - \sigma_{0,0} \tag{3-21}$$

where $\left(\frac{b}{a}\right)^2$ is the total transmission of all diffraction orders, and $\sigma_{0,0}$ is the zero-order RMS diffraction efficiency at the ROI, as defined in Equation (3-12).

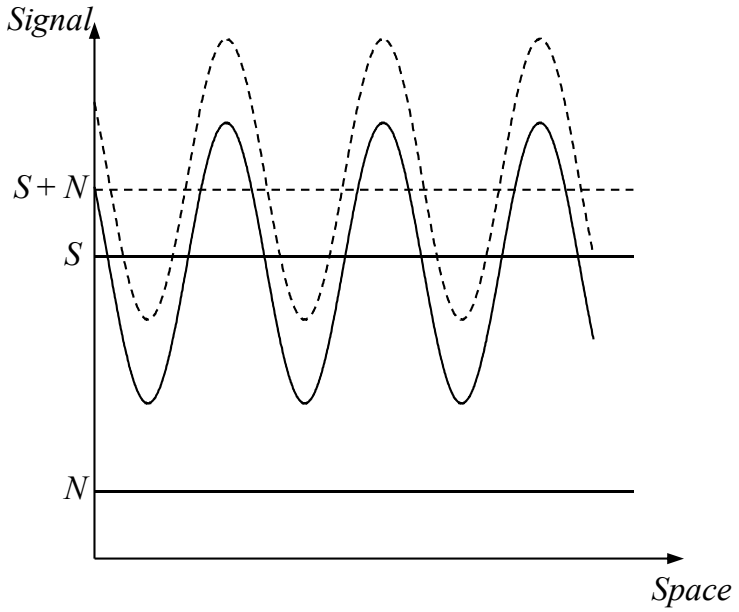

Figure 30: The effect of higher orders on the zero-order contrast.

The useful image information is in the zero-order, which can be considered the modulated signal of magnitude *S*. Since the spatial frequencies and contrast variations across an extended object are non-deterministic, the effect of higher diffraction orders from different field angles can be treated as white noise of magnitude *N*, washing down the contrast of the signal *S*. Figure 30 illustrates the effect of higher diffraction orders on the zero-order contrast. The MTF contrast of the zero-order is washed down by a factor

equal to $\frac{S}{S+N}$. From Equation (3-21), $S=\sigma_{0,0}$, $N=\sigma_{\substack{higher\\orders}}$, and $S+N=\left(\frac{b}{a}\right)^2$. So the diffraction MTF in Equation (3-18) is washed down by a factor equal to

$$\frac{S}{S+N}=\frac{\sigma_{0,0}}{(b/a)^2} \tag{3-22}$$

Assuming the RWFE at the ROI is very small (diffraction-limited), the MTF of the FOS at the ROI can be written as

$$MTF_{ROI}(\xi)=\frac{\sigma_{0,0}}{b/a}\times MTF_{aperture}(\xi) \tag{3-23}$$

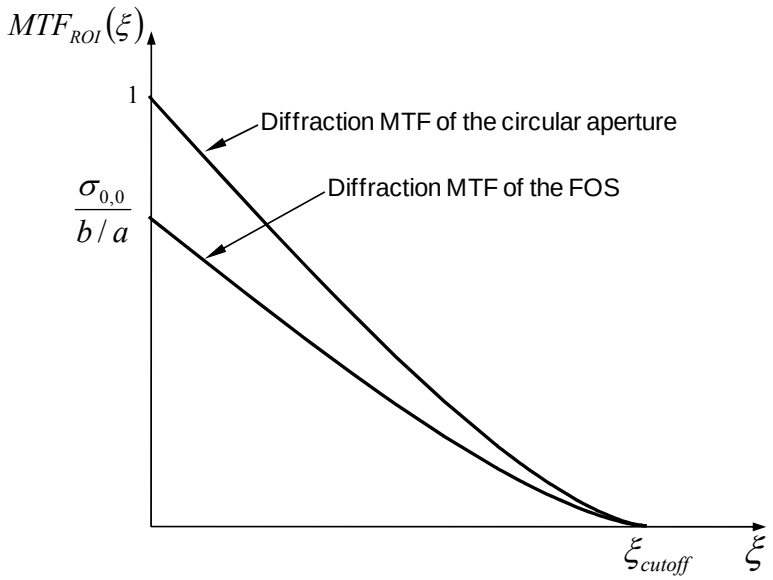

Figure 31: MTF at the ROI for a diffraction-limited FOS with a circular aperture, an SLM pixel fill factor, $\left(\frac{b}{a}\right)^2$, and a zero-order diffraction efficiency at the ROI, $\sigma_{0,0}$.

Figure 31 shows the estimated MTF at the ROI for a diffraction-limited FOS with a circular aperture, an SLM pixel fill factor, $\left(\frac{b}{a}\right)^2$, and a zero-order diffraction efficiency at the ROI, $\sigma_{0,0}$.

4 LENS DESIGN

The compact optical design of the fast wide-angle lens is one of the most challenging and important steps in the design of an FOS. This chapter covers the particularities, challenges, and tradeoffs involved in the optical design of fast wide-angle lenses for optical foveated imaging in the visible wavelength range. Several lens design examples, using spherical, aspheric, and hybrid optics, are presented and analyzed in terms of wavefront aberrations, distortion, relative illumination (RI), and design complexity. The design examples covered in this chapter are realistic and manufacturable designs that can be used in practical FOSs based on the current state-of-the-art transmissive LC SLM technology.

This chapter also covers the optical design we executed for an experimental wide-angle FOS prototype that was built as part of a joint effort project between the University of Central Florida (UCF), Sandia National Laboratories (SNL), Boulder Nonlinear Systems Inc. (BNS), the Naval Research Laboratories (NRL), and Narrascape LLC. The project was funded under the Defense Advanced Research Project Agency (DARPA) as part of the Bio-Optic Synthetic Systems (BOSS) Program.

4.1 Background

All fast wide-angle designs that have been proposed so far were not practical due to several different reasons. As previously discussed in Chapter 2, most FOS designs were aimed at building experimental prototypes using standard off-the-shelf components, because phase transmissive LC SLMs devices were not commercially available at the time. Most research has been focused on the experimental demonstration of the basic principle using off-the-shelf components, without much concern for the practicality or the optical performance of the systems. Published results quantify only the aberration correction capabilities of the FOS, often claiming diffraction-limited performance at the ROI, yet continually overlooking the effects of diffraction on the zero-order efficiency and the image quality. Also, the effects of the RI and distortion on the image quality are ignored in all previous wide-angle designs.

4.1.1 Previous Wide-Angle Designs

Even the initial theoretical design illustrating the basic concept of a fast wide-angle FOS using a transmissive SLM, proposed by Martinez et al [8], is not a practical design. Although it covers an impressive full FOV of 90 degrees with a very compact two-element optic, the proposed design requires an SLM with a resolution of 2048×2048 in order to achieve diffraction limited RWFE. The stop diameter in this design is about 8 mm, so the pixel pitch would have to be 3.9 μm. Considering a shadow mask width of 2.8

μm, which is the smallest width achieved so far in transmissive TFT technology [49], only 8% of the light would be transmitted, and only about 0.6% would be in the zero-order. Another disadvantage of this design is that towards the peripheral field angles, the incidence angles to the image plane become very steep. As a result, the RI at the maximum field angle drops down to almost 20%. This design was reproduced from the data provided by the authors and is presented in Appendix A.

A different wide-angle FOS design was proposed by Harriman et al [34], who demonstrated a system covering 120 degrees, using a transmissive LC SLM with a resolution of 1280×1024 and a pixel fill factor of 56%. However, this design turned out to be impractical as well, due to the limited zero-order diffraction efficiency, and the severe artifacts created by the higher diffraction orders.

4.1.2 Chromatic Limitations

Bagwell et al. proposed a "multi-spectral foveated imaging system" based on the wide-angle FOS built following our design [33]. The optical design we performed for this project is covered later, in Section 4.4. However, the system proposed by Bagwell et al. is not a real achromat, since the authors used an adjustable filter to capture three separate images at three different wavelengths (red, blue, and green). This FOS generates a color image, but does not increase the amount of light onto the sensor by broadening the wavelength range of the system.

Although an achromatic FOS is desirable in order to capture more light onto the sensor, all design examples in this chapter are limited to monochromatic systems. Achromatic systems are only practical in the case of all-reflective systems, such as telescopes using DMs [35,36,37], because they do not exhibit dispersion and DMs have large phase-strokes, eliminating the need for modulo-λ correction. On the other hand, there is no practical solution for an achromatic fast wide-angle FOS that could cover the entire visible wavelength range. As discussed previously in Section 2.3.2, optical arrangements in fast wide-angle lenses are fundamentally different than in the case of telescopes. The large FOV and low F/# in fast wide-angle lenses require an all-refractive/transmissive design in order to achieve a compact and practical FOS. The first problem with these systems is the limited phase stroke of transmissive LC SLMs, which requires modulo-λ correction. This limits significantly the wavelength range due to the quick falloff of the diffraction efficiency away from the center wavelength [35]. Another problem is caused by the dispersion in the optics and in the LC. Theoretically, the first problem could be solved by a transmissive SLM with a very large phase stroke, and the second problem could be solved by an optical design in which the chromatic aberrations are cancelled by the dispersion in the LC. However, none of these solutions seem practical, taking into account current limitations in the transmissive LC SLM technology.

4.2 Specifications and Requirements

In the next section, we propose several optical design examples that can be used to build practical fast wide-angle FOSs based on the current transmissive LC SLM technology. For all examples, it was assumed that a custom transmissive LC SLM device that can fit at the aperture stop can be built with the optimal resolution required by the particular lens design. The shadow mask width was considered to be 2.8 μm, which is the smallest width achieved so far in state-of-the-art transmissive TFT technology. Enough space was allowed between the stop and other optical elements to place the SLM. Although optical flats, such as the filter, polarizer, and SLM cover plates, do not have optical power, they were taken into account and represented in the optical design examples (if required), because they can have an impact on aberrations or create manufacturability issues related to mechanical and assembly constraints. Also, fabrication and assembly tolerances associated with these flat optical elements can further affect the image quality.

Table 3 lists the general design specifications and target requirements for all the monochromatic design examples. These specifications were set empirically, based on state-of-the-art realistic application requirements, taking into account the capabilities of the current manufacturing technologies. Prior to setting these specifications and requirements, a series of preliminary designs were performed in order to help assess feasibility and to ensure that requirements can be achieved with practical and compact designs. Some of these preliminary optical designs are shown in Appendix B. A detailed

example on how to determine the best achievable diffraction efficiency and MTF of an FOS for a given lens design and SLM shadow mask width is covered in the next Chapter.

Table 3: General design specifications and requirements.

Design wavelength	532 nm
EFL	18 mm
F/# (image space)	2.8
FOV (full diagonal)	80 degrees
Image diagonal (including distortion)	25-30 mm
Uncorrected RMS WFE (target)	< 2 waves
Uncorrected P-V WFE (target)	< 15 waves
Distortion (target)	< 20%
RI variation (target)	< 20%
Number of elements (spherical designs)	< 4
Number of elements (aspheric designs)	< 2
Total track	< 60 mm

4.2.1 First-Order Properties

All lenses were designed to the same first-order optical properties: EFL, F/#, and FOV. The EFL is 18 mm with an aperture ratio of F/2.8. The full diagonal FOV covers 80 degrees with a 25-30 mm diagonal image size (the variation in the image size allows for a maximum of ~20% negative distortion). Since most FOSs demonstrated so far have been designed to operate in the visible wavelength range, all design examples presented here

were optimized for 532 nm. Compared to the IR regions, in the visible, aberrations are the dominant factor affecting the image quality in fast imaging optics, so a fast wide-angle lens in the visible range would benefit more from optical foveated imaging than an equivalent IR lens.

4.2.2 Wavefront Aberrations

There are a few additional specific requirements that have to be taken into consideration when designing these lenses. In order to be able to build practical FOS based on the current transmissive LC SLM technology (2.8 μm shadow mask), aberrations in the uncorrected 18 mm, F/2.8, 80º FOV lens have to be less than 2 waves RMS and less than 15 waves P-V (roughly). This was determined empirically by applying the theory developed in Chapter 3 to several preliminary lens designs in which aberrations were corrected to different extents. Another requirement, which is somewhat intuitive from Chapter 3, is related to the distribution of the wavefront aberrations over the wide FOV of these lenses. Wavefront aberrations in fast wide-angle lenses typically tend to increase rapidly with the field angle. However, the uncorrected aberrations in an FOS should be distributed as evenly as possible over the FOV in order to obtain a uniform zero-order diffraction efficiency and image quality at the ROI across the entire FOV.

4.2.3 Relative Illumination and Distortion

The relative illumination (RI) and distortion are also important design requirements, specific to wide-angle FOSs. In a wide-angle FOS, the RI should be flat in order to truly achieve uniform performance at the ROI across the entire FOV. A drop in the RI with the field angle would result in a lower MTF contrast at the peripheral field angles. On the other hand, in wide-angle lenses, it is difficult to flatten the RI and correct the barrel distortion in the same time. However, distortion is only a field-dependent magnification error, and does not affect the resolution of the optics. As long as the resolution of the sensor array is large enough to avoid aliasing due to under-sampling, barrel distortion can be calibrated and corrected at the electronics or software level.

4.2.4 Stop Size

Another important aspect in the design of wide-angle FOSs based on transmissive LC SLMs is the size of the physical aperture stop in relation to the entrance pupil. Since the SLM is placed at the stop, the pixel pitch is proportional to the stop diameter. So, for a given SLM resolution and shadow mask width, a larger stop will result in a larger fill factor, and therefore, higher zero-order diffraction efficiency. As a result, the size of the stop should be as large as practically possible relative to the entrance pupil of the optical system.

4.3 Optical Design Examples

The lens design examples presented here are compact, light-weight, and cost effective. Complexity varies between 1 and 4 elements. Polished glass spherical optics and/or precision glass molded aspheric optics are used in all examples, taking into consideration manufacturability and cost. Although heavier than plastic optics, glass optics has the advantage of optical fabrication processes capable of very tight tolerances. Also, glasses have a coefficient of thermal expansion (CTE) much lower than the CTE of plastic optical materials. Therefore, glass designs can be used over a wider temperature range. In this chapter we do not take into consideration any fabrication or assembly tolerances. Manufacturing tolerances and their impact on the image quality of fast wide-angle FOSs are covered as a separate section in the next chapter.

4.3.1 Four-Element Spherical Design

Since this is a monochromatic design, there is no need to correct chromatic aberrations. Therefore, all elements can be made of a single glass type. BK7 glass (from Schott) was chosen in this design, since it is a cost effective and widely available glass, with good resistance to environmental agents. The 18 mm F/2.8 monochromatic lens covers a full FOV of 80 degrees and matches a sensor with a 25 mm diagonal. The overall length of the optics is 63 mm, with a back focal length of 30 mm. The lens prescription data is

given in Table 4. The optical layout, the largest wavefront aberration (at 40º), distortion, and RI plots are shown in Figure 32. This 4-element design is arranged in a retrofocus configuration, with a front negative element followed by a rear positive group. This type of arrangement is typically used in fast wide-angle lenses with aperture ratios ranging from F/4 down to F/1.8 and FOVs larger than 60 degrees [1].

The RI in wide-angle lenses tends to decrease towards the peripheral field angles. One reason this happens is the *cosine-fourth falloff rule*: the illumination onto the image plane decreases proportionally with the cosine-fourth of the angle of incidence of the chief-ray to the image plane. If the exit pupil is located at infinity (or very far) from the image plane, such as in image-space telecentric systems, all chief-rays fall perpendicular onto the image plane, eliminating the cosine-fourth problem. The stop in this design was positioned between the negative and the positive group, as close as possible to the focal point of the positive group, in order to place the exit pupil as far as possible from the image plane. Vignetting at the peripheral field angles is another factor that could contribute to the drop in the RI. In this design example, there is no vignetting. Additionally, the effect of negative distortion combined with blur caused by other aberrations helps to offset the cosine-fourth effect. As a result, the RI is almost flat across the FOV (only 3% drop at the maximum field angle). On the other hand, as previously discussed, it is difficult to flatten RI and correct barrel distortion in these lenses. The barrel distortion in this lens is 18% at the maximum field angle.

Table 4: Prescription – four element spherical design (all dimensions in mm).

Surf:Type		Comment	Radius	Thickness	Glass	Semi-Diameter	
OBJ	Standard		Infinity	Infinity		Infinity	
1	Standard		Infinity	7.000000		0.000000	U
2*	Standard	Lens 1	20.199219	2.700000	BK7	11.700000	U
3*	Standard		7.733743	8.100000		7.200000	U
4*	Standard	Polarizer	Infinity	0.900000	B270	7.200000	U
5*	Standard		Infinity	0.450000		7.200000	U
6*	Standard	Filter	Infinity	0.900000	F_SILICA	7.200000	U
7*	Standard		Infinity	2.250000		7.200000	U
8*	Standard	SLM front cover	Infinity	0.900000	SUPRASIL	5.400000	U
STO	Standard	SLM back cover	Infinity	0.900000	SUPRASIL	4.778000	U
10*	Standard		Infinity	4.050000		5.400000	U
11*	Standard	Lens 2	-26.035432	3.600000	BK7	7.400000	U
12*	Standard		-13.901774	0.360000		9.000000	U
13*	Standard	Lens 3	-194.793427	3.600000	BK7	9.450000	U
14*	Standard		-25.952554	0.360000		10.800000	U
15*	Standard	Lens 4	54.770178	3.600000	BK7	11.700000	U
16*	Standard		-79.984847	30.127212		11.700000	U
IMA	Standard		Infinity	-		12.214713	

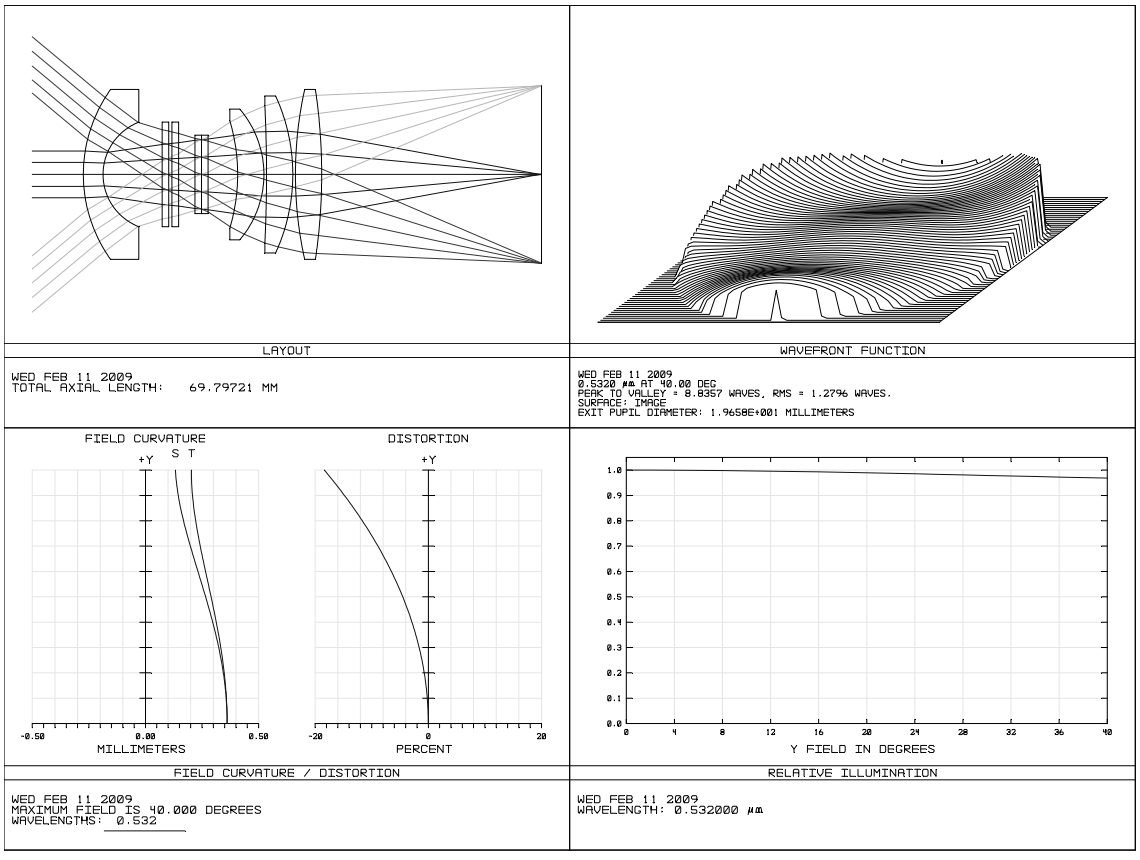

Figure 32: Four-element spherical design.

The stop was also positioned as far as possible behind the negative front element in order to increase as much as possible the stop diameter relative to the entrance pupil diameter. The stop in this lens is 50% larger than the entrance pupil, significantly increasing the required pixel pitch for a given SLM resolution.

The RMS and P-V wavefront aberrations at 0º, 10º, 20º, 30º, and 40º are listed in Table 5. The design was optimized to distribute aberrations as uniformly as possible across the FOV. The maximum P-V wavefront error is 9 waves, which is larger than the phase stroke of transmissive LC SLMs currently available. Therefore, the correction has to be done modulo-λ.

Table 5: Wavefront aberrations of the uncorrected lens.

Field angle in degrees	0º	10º	20º	30º	40º
RMS WFE in waves	0.74	0.69	0.67	0.87	1.28
P-V WFE in waves	2.95	2.71	3.29	4.98	9.01

4.3.2 Three-Element Spherical Design

Since the same optical power can be obtained with a higher index and larger radii of curvature, a higher refractive index glass could be used in the previous design example in order to reduce the surface sag of the optical elements. Shallower sags usually decrease

aberrations, as the incidence angles of the marginal rays to the optical surfaces become less extreme.

In this example, the positive three-element group was replaced by a doublet made of LASF-9 (from Schott), a glass with a refractive index of 1.85. The negative front element was left in BK-7, with a refractive index of about 1.52. This is exactly the opposite arrangement than the arrangement of an achromat. In an achromatic lens, the negative element is made of a *flint* glass (high index, high dispersion), and the positive element is made of a *crown* glass (low index, low dispersion). However, since this example is only a monochromatic design, color correction is not important. The lens prescription data is given in Table 6. The optical layout, largest wavefront aberration (at 40º), distortion, and RI plots are shown in Figure 33. The 18 mm F/2.8 monochromatic lens covers a full FOV of 80 degrees and matches a sensor with a 24 mm diagonal. The overall length of the optics is 60 mm, with a back focal length of 26 mm. At the maximum field angle, the RI drops by 5%, and barrel distortion is 19%.

Table 6: Prescription – three element spherical design (all dimensions in mm).

Surf:Type		Comment	Radius	Thickness	Glass	Semi-Diameter	
OBJ	Standard		Infinity	Infinity		Infinity	
1	Standard		Infinity	10.000000		0.000000	U
2	Standard	Lens 1	16.220809	4.000000	N-BK7	12.167939	
3	Standard		8.299604	12.000000		7.974334	
4	Standard	Polarizer	Infinity	2.000000	F_SILICA	5.487777	
5	Standard		Infinity	1.000000		4.944682	
6	Standard	SLM front cover	Infinity	1.000000	SUPRASIL	4.530335	
STO	Standard	SLM back cover	Infinity	1.000000	SUPRASIL	4.258787	
8	Standard		Infinity	4.000000		4.690285	
9	Standard	Lens 2	-37.566439	4.000000	N-LASF9	7.054505	
10	Standard		-18.260689	0.360000		8.242481	
11	Standard	Lens 4	65.834721	4.000000	N-LASF9	9.397872	
12	Standard		-60.250492	25.991065		9.711320	
IMA	Standard		Infinity	-		12.109805	

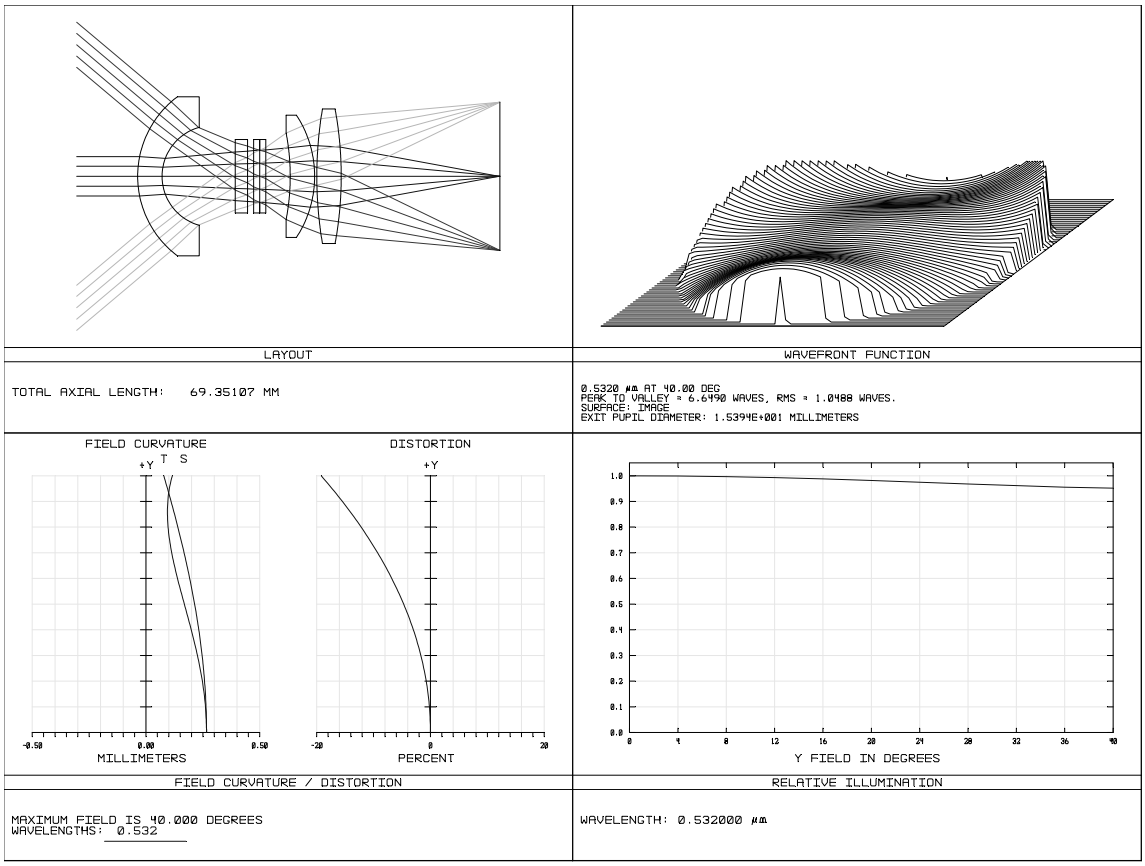

Figure 33: Three-element spherical design.

The RMS and P-V wavefront aberrations at 0º, 10º, 20º, 30º, and 40º are listed in Table 7. The largest wavefront aberration occurs at the 40º field angle, and is 6.73 waves P-V and 1.05 waves RMS. Even though it has only three elements, this lens design is slightly less aberrated than the four-element design presented in the previous example. On the other hand, the shape of the front meniscus element became more extreme, which could increase cost and the sensitivity of the lens to manufacturing tolerances. Also, the stop in this design is only 33% larger than the entrance pupil, which is smaller compared to the stop in the previous example.

Table 7: Wavefront aberrations of the uncorrected lens.

Field angle in degrees	0º	10º	20º	30º	40º
RMS WFE in waves	0.58	0.54	0.58	0.72	1.05
P-V WFE in waves	2.27	2.35	3.36	4.98	6.73

4.3.3 Aspheric Doublet Design

Aspheric optics can be used to further reduce the number of elements in these lenses. Precision glass molding is a newly developed optical fabrication process that can produce aspheric optics with tight tolerances in large volumes and at a reasonable cost. A high index moldable glass, SF57 (from Schott), was used to design a two-element lens with the same first-order specifications as in the previous examples. The main goal in this design was to make the lens as compact as possible.

The lens prescription data is given in Table 8. The optical layout, largest wavefront aberration (at 30º), distortion, and RI plots are shown in Figure 34. The 18 mm F/2.8 monochromatic lens covers a full FOV of 80 degrees and matches a sensor with a 24 mm diagonal. The overall length of the optics is 38 mm, with a back focal length of 25 mm, making this design much more compact than the previous spherical examples. At the maximum field angle, the RI drops by 20%, and the barrel distortion is 20%. The significant drop in the RI is due to the position of the stop, which was placed very close to the positive element in order to obtain a more compact design.

Table 8: Prescription – aspheric doublet design (all dimensions in mm).

Surf:Type		Comment	Radius	Thickness	Glass	Semi-Diameter	
OBJ	Standard		Infinity	Infinity		Infinity	
1	Standard		Infinity	10.000000		0.000000	U
2	Even Asphere		27.963919	3.000000	SF57_MOLD	5.305861	
3	Even Asphere		9.898565	1.000000		3.653633	
4	Standard	SLM front cover	Infinity	1.000000	SUPRASIL	3.601602	
STO	Standard	SLM back cover	Infinity	1.000000	SUPRASIL	3.345096	
6	Standard		Infinity	1.000000		4.013527	
7	Even Asphere	Lens 2	-31.028221	6.000000	SF57_MOLD	4.767543	
8	Even Asphere		-8.622466	25.016738		6.730281	
IMA	Standard		Infinity	-		12.088869	

Aspheric coefficients:

Surf:Type		Conic	2nd Order Term	4th Order Term	6th Order Term	8th Order Term	10th Order Term
OBJ	Standard	0.000000					
1	Standard	0.000000					
2	Even Asphere	0.000000	0.000000	6.877467E-005	-1.339535E-006	2.724192E-008	-6.842601E-010
3	Even Asphere	0.000000	0.000000	6.830373E-004	-1.025719E-006	1.477199E-006	2.977702E-009
4	Standard	0.000000					
STO	Standard	0.000000					
6	Standard	0.000000					
7	Even Asphere	0.000000	0.000000	-1.808999E-004	-3.263307E-006	1.736862E-007	-5.975329E-010
8	Even Asphere	0.000000	0.000000	-4.333381E-005	-7.459112E-007	-2.759695E-009	-3.056850E-010
IMA	Standard	0.000000					

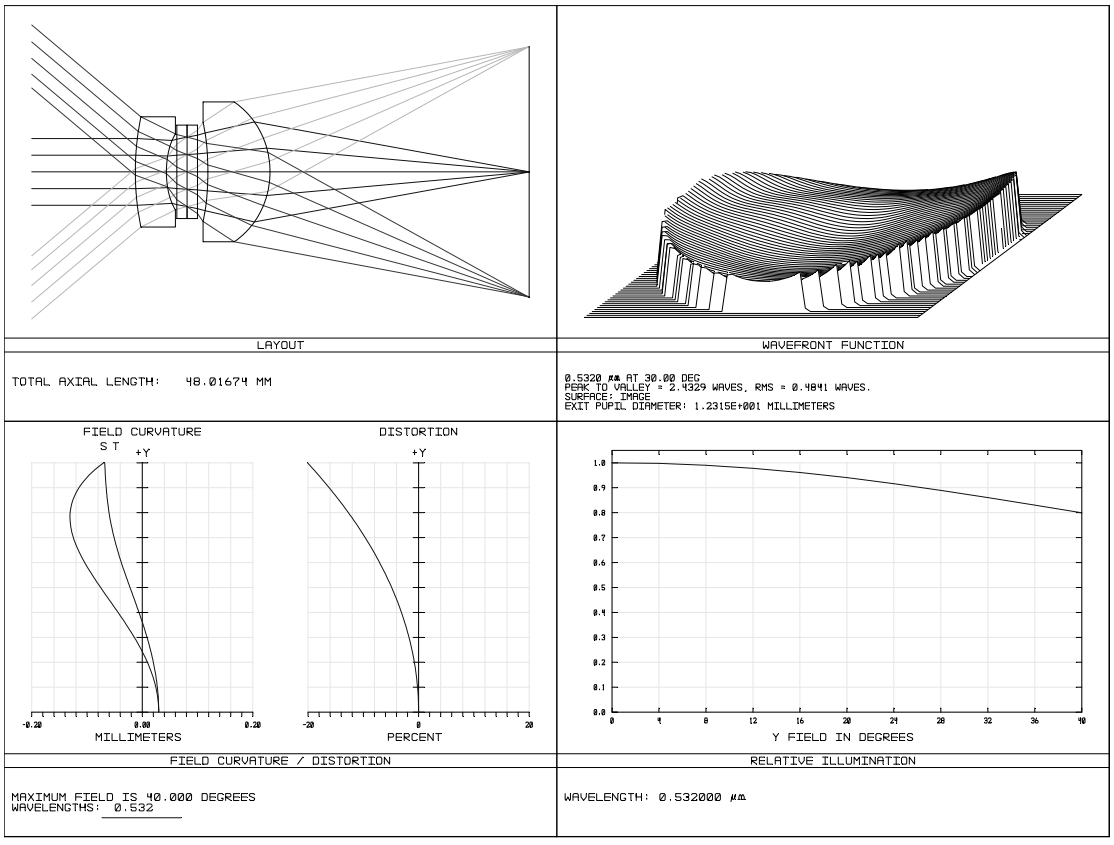

Figure 34: Aspheric doublet design.

The RMS and P-V wavefront aberrations at 0º, 10º, 20º, 30º, and 40º are listed in Table 9. The largest wavefront aberration occurs at the 30º field angle, and is 2.59 waves P-V and 0.49 waves RMS. This aspheric design is significantly less aberrated than the previous spherical design examples. However, the stop in this lens is only 4% larger than the entrance pupil, because it was placed very close to the front element in order to make the lens more compact.

Table 9: Wavefront aberrations of the uncorrected lens.

Field angle in degrees	0º	10º	20º	30º	40º
RMS WFE in waves	0.42	0.29	0.35	0.49	0.33
P-V WFE in waves	1.26	1.20	2.02	2.59	1.95

4.3.4 Aspheric Single-Element Design

An even more compact design can be achieved with a single aspheric element. The same moldable high refractive index glass, SF57, was used to design a single-element lens with the stop very close to the front optical surface. In this design, the stop is also the entrance pupil. The lens in this example is a thick meniscus bent towards the object space, which is essentially a very compact retrofocus design with a front negative optical surface and a rear positive surface. The lens is relatively thick in order to efficiently correct off-axis aberrations and flatten the RI as much as possible.

Table 10: Prescription – aspheric single-element design (all dimensions in mm).

Surf:Type		Comment	Radius	Thickness	Glass	Semi-Diameter	
OBJ	Standard		Infinity	Infinity		Infinity	
1	Standard		Infinity	10.000000		0.000000	U
2	Standard	SLM front cover	Infinity	1.000000	SUPRASIL	3.704272	
STO	Standard	SLM back cover	Infinity	1.000000	SUPRASIL	3.214220	
4	Standard		Infinity	1.000000		3.704272	
5	Even Asphere	Lens 2	-18.743354	8.500000	SF57_MOLD	4.007712	
6	Even Asphere		-10.227528	22.126282		7.620202	
IMA	Standard		Infinity	-		12.677018	

Aspheric coefficients:

Surf:Type		Conic	2nd Order Term	4th Order Term	6th Order Term	8th Order Term	10th Order Term
OBJ	Standard	0.000000					
1	Standard	0.000000					
2	Standard	0.000000					
STO	Standard	0.000000					
4	Standard	0.000000					
5	Even Asphere	0.000000	0.000000	-6.537853E-004	1.291690E-005	-5.998060E-007	-4.662039E-008
6	Even Asphere	0.000000	0.000000	4.826701E-007	-3.128424E-006	7.642628E-008	-9.598295E-010
IMA	Standard	0.000000					

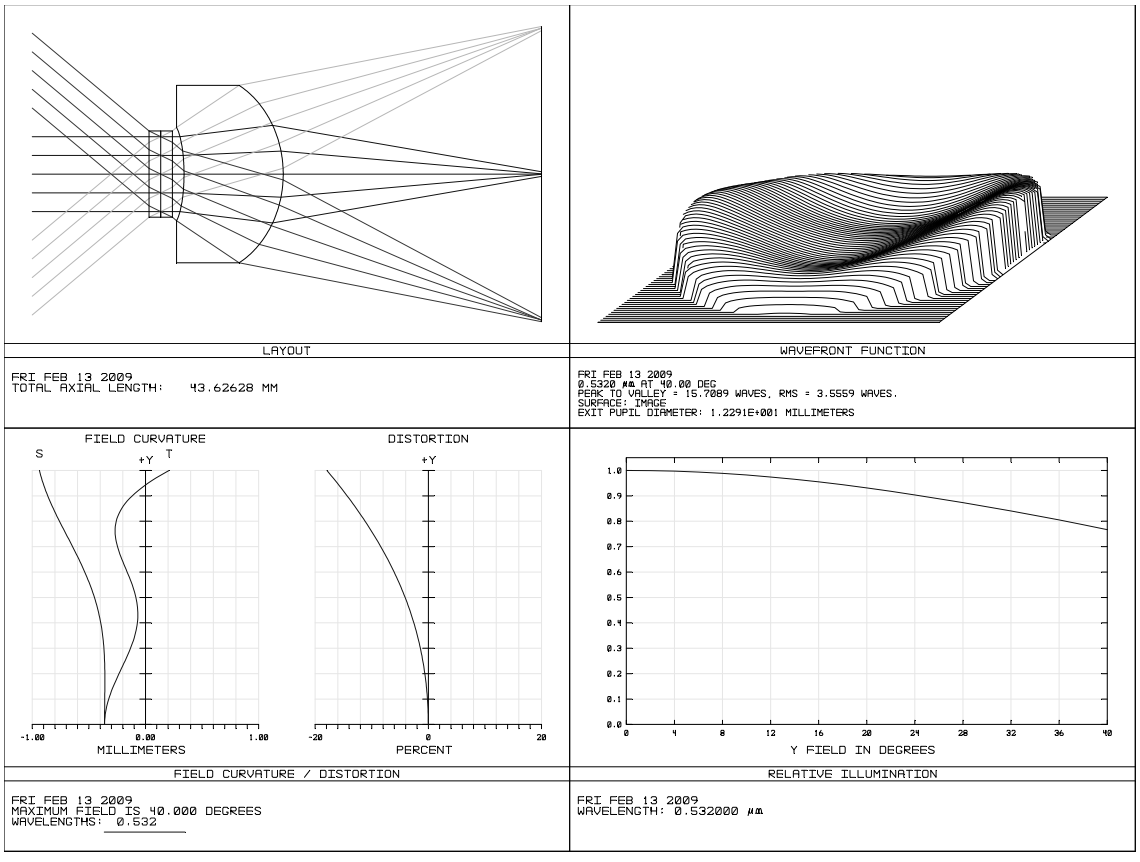

Figure 35: Aspheric single-element design.

The lens prescription data is given in Table 10. The optical layout, largest wavefront aberration (at 40º), distortion, and RI plots are shown in Figure 35. The 18 mm F/2.8 monochromatic lens covers a full FOV of 80 degrees and matches a sensor with a 25 mm diagonal. The overall length of the optics is 34 mm, with a back focal length of 22 mm. At the maximum field angle, the RI drops by 23%, and the barrel distortion is 18%. The RI in this design can be further flattened by moving the stop further away from the lens. However, the optics diameter increases quickly as the stop is moved away from the lens, due to the wide-FOV. Also, moving the stop further results in extreme aspheric surfaces, which would be difficult or impossible to manufacture in glass with reasonable precision.

The RMS and P-V wavefront aberrations at 0º, 10º, 20º, 30º, and 40º are listed in Table 11. The largest wavefront aberration occurs at the 40º field angle, and is 15.79 waves P-V and 3.55 waves RMS. This single-element design is more aberrated than all the previous design examples, but it is a very compact lens.

Table 11: Wavefront aberrations of the uncorrected lens.

Field angle in degrees	0º	10º	20º	30º	40º
RMS WFE in waves	3.60	3.14	1.88	2.18	3.55
P-V WFE in waves	12.42	12.95	9.82	11.67	15.79

4.3.5 Hybrid (Spherical-Aspheric) Doublet Design

A very practical, low-cost and compact design was achieved by combining a spherical element with an aspheric element in a retrofocus arrangement. Both elements in this design are easy to manufacture and can be conveniently assembled in a very compact housing. The front negative element is a plano-concave spherical lens made of BK7. The rear positive element is a bi-convex aspheric lens that can be easily molded in SF57. The SLM fits at the stop, closely sandwiched between the two elements.

Table 12: Prescription – hybrid doublet design (all dimensions in mm).

Surf: Type		Comment	Radius	Thickness	Glass	Semi-Diameter	
OBJ	Standard		Infinity	Infinity		Infinity	
1	Standard		Infinity	10.000000		0.000000	U
2*	Even Asphere		-11.270877	1.800000	BK7	5.000000	U
3*	Even Asphere		Infinity	0.500000		6.500000	U
4*	Standard	SLM front cover	Infinity	1.000000	SUPRASIL	6.500000	U
STO	Standard	SLM back cover	Infinity	1.000000	SUPRASIL	3.620593	
6*	Standard		Infinity	1.200000		6.500000	U
7	Even Asphere	Lens 2	37.851119	4.500000	SF57_MOLD	5.665838	
8*	Even Asphere		-14.250320	21.700770		7.000000	U
IMA	Standard		Infinity	-		11.262335	

Aspheric coefficients:

Surf: Type		Conic	2nd Order Term	4th Order Term	6th Order Term	8th Order Term	10th Order Term
OBJ	Standard	0.000000					
1	Standard	0.000000					
2*	Even Asphere	0.000000	0.000000	0.000000	0.000000	0.000000	0.000000
3*	Even Asphere	0.000000	0.000000	0.000000	0.000000	0.000000	0.000000
4*	Standard	0.000000					
STO	Standard	0.000000					
6*	Standard	0.000000					
7	Even Asphere	0.000000	0.000000	-1.960704E-004	0.000000	0.000000	0.000000
8*	Even Asphere	0.000000	0.000000	-1.309551E-004	3.914311E-006	-1.209040E-007	8.872091E-010
IMA	Standard	0.000000					

The lens prescription data is given in Table 12. The optical layout, largest wavefront aberration (at 30º), distortion, and RI plots are shown in Figure 36. The 18 mm F/2.8 monochromatic lens covers a full FOV of 80 degrees and matches a sensor with a 22.5 mm diagonal. The overall length of the optics is 33 mm, with a back focal length of

22 mm. This is the most compact of all the design examples presented here. At the maximum field angle, the RI drops by 13%, and the barrel distortion is 24%.

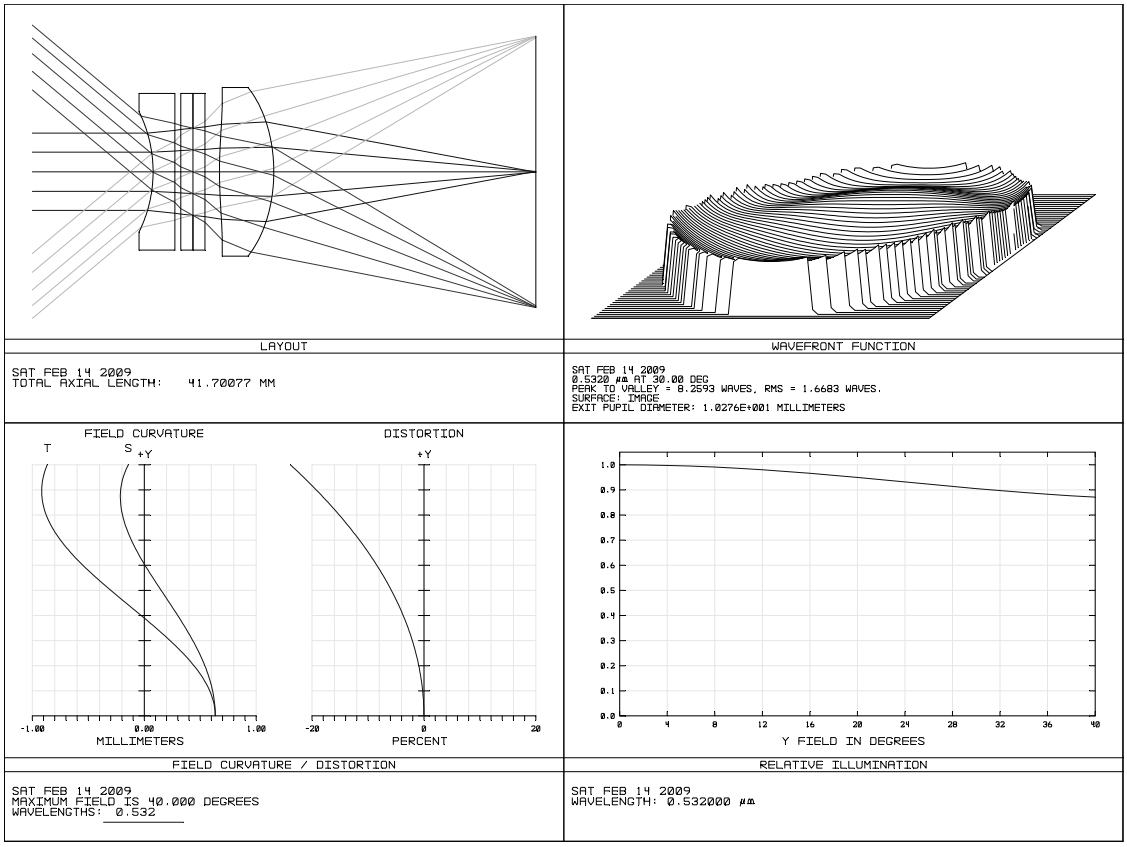

Figure 36: Hybrid doublet design.

Table 13: Wavefront aberrations of the uncorrected lens.

Field angle in degrees	0º	10º	20º	30º	40º
RMS WFE in waves	1.82	1.29	1.10	1.67	1.19
P-V WFE in waves	6.47	4.69	6.03	8.28	8.40

The RMS and P-V wavefront aberrations at 0º, 10º, 20º, 30º, and 40º are listed in Table 13. The largest wavefront aberration occurs at the 30º field angle, and is 8.28 waves P-V

and 1.67 waves RMS. This compact, practical, and elegant design is an excellent tradeoff between design complexity and optical performance.

4.4 Optical Design for an Experimental Wide-Angle FOS Prototype

We also designed a custom wide-angle optical system for an experimental FOS prototype that was developed as part of a joint effort project between the University of Central Florida (UCF), Sandia National Laboratories (SNL), Boulder Nonlinear Systems Inc. (BNS), the Naval Research Laboratories (NRL), and Narrascape LLC. The FOS prototype was built at SNL, using a standard reflective LC SLM device provided by BNS, filled with high-birefringence LC developed at UCF. The main goal of the project was to develop a foveated imaging system covering a larger FOV than the previous experimental prototype demonstrated by Wick et al. [31].

We designed a 27 mm F/7.7 lens covering a full FOV of 60 degrees to match a 26 mm diagonal sensor. The design was optimized for operation at 633 nm. The lens prescription data is given in Table 14. The optical layout, largest wavefront aberration (at 30º), distortion, and RI plots are shown in Figure 37. This two-element design is arranged in a retrofocus configuration formed by a plano-concave front element and a plano-convex rear element with spherical surfaces. The use of plano and spherical surfaces allowed for easy fitting to off-the-shelf lenses. The optical axis is folded by a beam splitter cube placed in front of the SLM. The optical design also includes a front protective window, a

polarizer, and a 633 nm narrowband filter. The largest aberration is 35 waves P-V and 6.3 waves RMS. The RI is flat and the barrel distortion is 13% at the maximum field angle.

The optics ended up relatively bulky (78×121×50 mm, not including the front window). The BFL is 74 mm, 2.74 times longer than the EFL. This design was severely constrained by having to place an off-the-shelf reflective SLM at the pupil stop. A transmissive SLM would have significantly simplified the optical design, but there were no such devices available at that time. Even at this time, we are not aware of any practical transmissive LC SLM devices that could be used to build a compact and efficient wide-angle FOS.

Table 14: Prescription data – experimental prototype (all dimensions in mm).

Surf:Type		Comment	Radius	Thickness		Glass		Semi-Diameter	
OBJ	Standard		Infinity	Infinity				Infinity	
1	Standard		Infinity	30.000000				0.000000	U
2*	Standard		Infinity	15.900000		QUARTZ		38.100000	U
3	Standard		Infinity	10.000000				0.000000	U
4*	Standard	FIRST LENS	Infinity	2.000000		BK7		23.500000	U
5*	Standard		25.939660	20.000000				23.500000	U
6*	Standard		Infinity	2.000000		B270		25.000000	U
7*	Standard		Infinity	0.000000				25.000000	U
8*	Standard		Infinity	7.000000		F_SILICA		25.000000	U
9*	Standard		Infinity	15.000000				25.000000	U
10*	Standard	ENTRANCE CUBE	Infinity	25.000000		BK7		12.500000	U
11*	Standard	EXIT CUBE	Infinity	5.000000				12.500000	P
12*	Standard	SUPRASIL COVER	Infinity	2.000000		1.46,67.9		5.430000	U
STO*	Standard	SLM	Infinity	0.000000		MIRROR		5.430000	U
14	Standard	SUPRASIL COVER	Infinity	-2.000000		1.46,67.9	P	5.430000	U
15	Standard		Infinity	-5.000000	P			4.195401	
16*	Standard	ENTRANCE CUBE	Infinity	-12.500000	P	BK7		12.500000	P
17	Coordinate B..	CUBE		0.000000		-		0.000000	
18*	Standard	CUBE	Infinity	0.000000		MIRROR		17.677700	U
19	Coordinate B..	CUBE		0.000000		-		0.000000	
20*	Tilted	EXIT CUBE		12.500000	P	BK7		12.500000	P
21*	Standard		Infinity	5.000000				12.500000	U
22*	Standard	SECOND LENS	Infinity	5.200000		BK7		12.500000	U
23*	Standard		-26.169790	74.182661				12.500000	U
IMA	Standard		Infinity	-				13.051934	

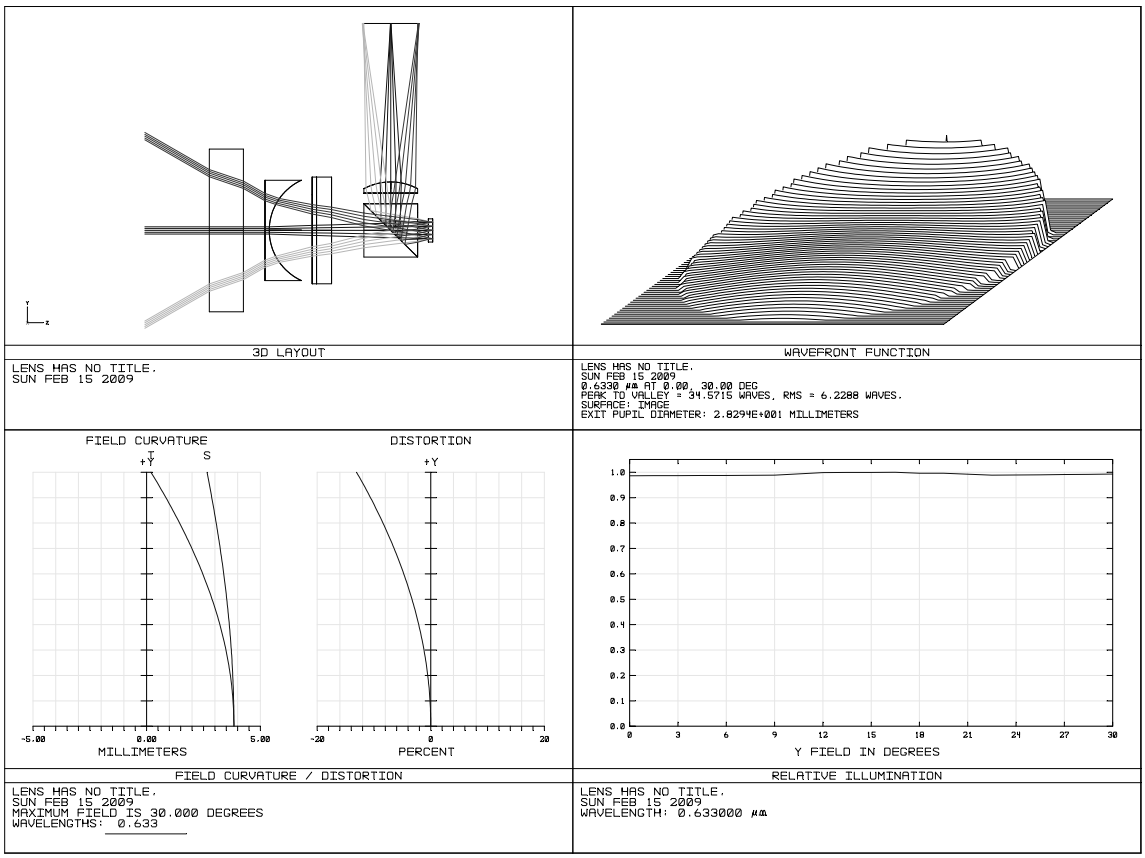

Figure 37: Optical design for the experimental prototype.

Figure 38 shows a photograph of the wide-angle foveated imaging system built at SNL from our optical design. The SLM was a 7.68 × 7.68 mm reflective device with a resolution of 512×512 pixels and a 15 μm pixel pitch. The cell gap was 2.5 μm thick and was filled with high-birefringence LC ($\Delta n = 0.39$ at 633 nm), to obtain a phase stroke larger than one wavelength (in double-pass). Correction was done modulo-λ.

The prototype was tested with an 8×8 ft print of an airport scene placed in the object plane. Figure 39 shows two experimental images taken with correction applied at two different ROIs.

Figure 38: Wide-angle FOS prototype.

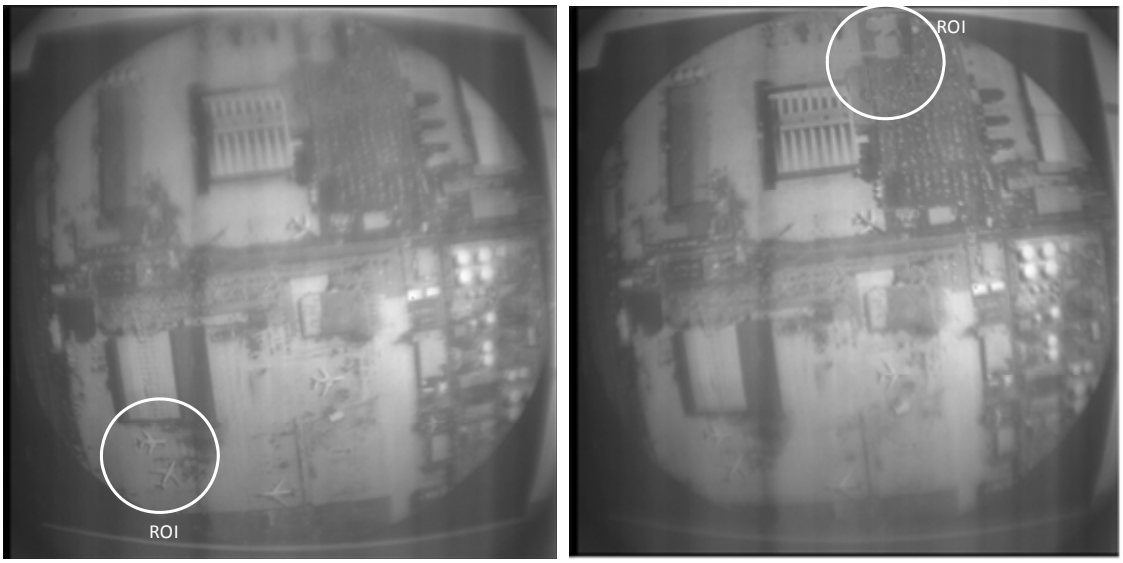

Figure 39: Experimental images with correction at two different ROIs.

This prototype achieved the main goal of the project, which was to develop and demonstrate an FOS with a wider FOV than the previous experimental demonstrations. However, since the design was severely constrained by using mostly off-the-shelf

components, this FOS ended up relatively slow (F/7.7) and bulky. This FOS was subsequently used by Bagwell et al. to develop a multispectral foveated imaging system [33].

5 FOVEATED OPTICAL SYSTEM DESIGN

The first section in this chapter covers the methods used in this dissertation to compute the diffraction efficiency and MTF of an FOS for a given lens design and a given SLM. The computational methods proposed in the first section are applied to determine the optimal SLM resolution for the best FOS performance, using the four-element spherical design presented in Section 4.3.1 as an example, and assuming a 2.8 μm shadow mask. The MTF performance and size of the ROI are estimated for the same lens design, which is used as an example throughout this chapter. Also, the effects of fabrication and assembly tolerances on the actual performance of the FOS are analyzed, revealing the sensitivity of fast wide-angle systems to manufacturing tolerances. A method to calibrate the SLM in order to cancel out additional aberrations introduced by tolerances is proposed. This chapter also compares the estimated MTF performance of the FOS design example proposed here to the MTF of an equivalent conventional lens, taking into account the diffraction efficiency and the SLM transmission of the FOS. At the end of this chapter, a few general and particular foveated imaging system design considerations are covered, relating design parameters to practical application requirements.

5.1 Computational Methods

To estimate the performance of an FOS in terms of diffraction efficiency and image quality across the entire FOV, we have to evaluate the wavefront aberration, the zero-order diffraction efficiency, $\sigma_{0,0}$, and $MTF(\xi = 0)$ at the ROI. Additionally, we also have to determine aberrations, $\sigma_{0,0}$, and $MTF(\xi = 0)$ at the other field angles, while the correction is applied at the ROI. This section covers the methods used in this dissertation to evaluate aberrations, $\sigma_{0,0}$, and $MTF(\xi = 0)$ for a given lens design, SLM resolution, and shadow mask width.

5.1.1 Diffraction Efficiency at the ROI

Zemax was used for all the optical design and analysis work covered in this dissertation [54]. In Zemax, like in most commercially available ray-tracing programs, the pupil aberration of an optical system at any field angle can be extracted as a two-dimensional $N \times N$ array, also called *wavefront map*. The sampling resolution for the wavefront map can be set by the user to any of the following values: 32×32, 64×64, 128×128, and so on, up to 8192×8192. We can look at this sampling resolution as being equivalent to the SLM resolution. As a result, the local P-V RWFE caused by the piston-only OPD of the SLM on x and y at every pixel $[i, j]$ when the wavefront aberration is corrected at the ROI by an SLM with a resolution of $N \times N$ can be determined directly from the $N \times N$ wavefront map of the aberration at the ROI, $W_{ROI}[i, j]$:

$$RWFE_{P\text{-}Vx}[i,j] = |W_{ROI}[i+1,j] - W_{ROI}[i,j]|$$
$$RWFE_{P\text{-}Vy}[i,j] = |W_{ROI}[i,j+1] - W_{ROI}[i,j]| \tag{5-1}$$

For an SLM resolution of $N \times N$, the ratio $\frac{b}{a}$ can be calculated as

$$\frac{b}{a} = 1 - \frac{w}{a} = 1 - \frac{N\,w}{D_{Stop}} \tag{5-2}$$

where *w* is the width of the SLM shadow mask and D_{Stop} is the pupil stop diameter for the lens design. It is assumed here that a square SLM covers the entire circular pupil of the optics.

A Zemax macro was written to compute $\sigma_{0,0}$ and $MTF(\xi = 0)$, given the ratio $\frac{b}{a}$ and the wavefront map. The code for the Zemax macro is given in Appendix C. This macro reads in an $N \times N$ wavefront map and calculates the $RWFE_{P\text{-}Vx,y}[i,j]$ values using Equation (5-1). Then, Equations (3-11) and (3-12) are used to calculate $\sigma_{0,0}$. The *MTF* at $\xi = 0$ is calculated from Equation (3-23) as

$$MTF(\xi = 0) = \frac{\sigma_{0,0}}{b/a} \tag{5-3}$$

5.1.2 RMS RWFE at the ROI

Sometimes, it might be necessary to evaluate the RWFE at the ROI, which can be calculated as the RMS across x and y of the local RMS RWFE at every pixel $[i, j]$. Since the local RWFE at every pixel is a wavefront tilt, the local RMS RWFE on x and y can be written in terms of the local P-V RWFE, taking into consideration the truncation factor, $\frac{b}{a}$:

$$\begin{aligned} RWFE_{RMSx}[i,j] &= \int_{-a/2}^{a/2} \frac{b}{a} RWFE_{P\text{-}Vx}[i,j]\, x\, dx = \frac{b}{a} \frac{RWFE_{P\text{-}Vx}[i,j]}{2\sqrt{3}} \\ RWFE_{RMSy}[i,j] &= \int_{-a/2}^{a/2} \frac{b}{a} RWFE_{P\text{-}Vy}[i,j]\, y\, dy = \frac{b}{a} \frac{RWFE_{P\text{-}Vy}[i,j]}{2\sqrt{3}} \end{aligned} \tag{5-4}$$

Therefore, for an SLM resolution of $N \times N$, the RMS RWFE across the pupil can be calculated as

$$RWFE_{RMS} = \frac{b}{a} \sqrt{\frac{\sum_{i,j=1}^{N} \left[\left(RWFE_{P\text{-}Vx}[i,j] \right)^2 + \left(RWFE_{P\text{-}Vy}[i,j] \right)^2 \right]}{12\, N^2}} \tag{5-5}$$

5.1.3 Performance at the Uncorrected Field Angles

Now, what happens at the other field angles when the wavefront aberration is corrected at the ROI? The zero-order diffraction efficiency at any given field angle depends only on the SLM resolution, $\frac{b}{a}$, and the initial wavefront aberration at that field angle, W. At any given field angle, the diffraction efficiency remains constant, regardless of where within the FOV the correction is applied. Therefore, $\sigma_{0,0}$ and $MTF(\xi = 0)$ at any angle, can be calculated by applying the Zemax macro to the wavefront map of the initial uncorrected aberration at that particular angle, following the same method for calculating $\sigma_{0,0}$ and $MTF(\xi = 0)$ at the ROI.

In addition to the amplitude and phase diffraction effects caused by the pixelated structure of the SLM, uncorrected field angles are also affected by the wavefront aberration $W' = W - W_{ROI}$, where W is the initial aberration and W_{ROI} is the wavefront correction applied at the ROI. The effect of this aberration on the MTF can be obtained directly from Zemax, which uses a Fast Fourier Transform (FFT) algorithm to compute the MTF of an optical system, including both diffraction and aberration effects.

To evaluate the effect of W' on the MTF, a *Zernike fringe phase surface* can be placed at the stop to simulate the OPD introduced by the SLM at the ROI. In Zemax, the Zernike fringe phase surface is a zero-thickness surface with a phase described by Zernike fringe polynomials. If the Zernike coefficients from the wavefront aberration at the ROI are

placed in the Zernike phase surface, the aberration at all field angles becomes $W' = W - W_{ROI}$, and the MTF can be directly evaluated in Zemax. However, the MTF from Zemax only takes into consideration the wavefront aberration and the diffraction from the aperture (circular aperture, in our case). To obtain the actual MTF of the FOS, we have to multiply the MTF curve from Zemax by the wash-down factor $MTF(\xi = 0)$, from Equation (5-3).

5.2 The Optimal SLM Resolution

As discussed in Section 2.3.5, transmissive LC SLMs are based on the active matrix backplane technology, where a shadow mask is placed over the electronics, creating a periodic amplitude structure. Also, the piston-only correction introduces a residual wavefront error (RWFE) at each pixel, generating a quasi-periodic phase structure across the pupil. In Chapter 3, it was shown that this periodic amplitude and phase structure has the effect of a two-dimensional diffraction grating, affecting the zero-order diffraction efficiency and MTF of the FOS. This section covers a method to determine the optimal SLM resolution. The four-element spherical design example presented in Section 4.3.1 is taken as an example.

5.2.1 Background

Most research in the field of optical foveated imaging is currently pursuing the development of relatively high-resolution transmissive LC SLMs in order to correct large wavefront aberrations. For instance, Harriman et al. demonstrated a wide-angle FOS using a 1280×1024 transmissive SLM with a pixel pitch of 15 μm [34]. The width of the shadow mask was 3.8 μm and the fill factor was 56%. As a result, the zero-order diffraction efficiency and the image quality were very poor. The authors measured the zero-order diffraction efficiency due to the shadow mask to be only about 15% (fill factor squared and the loss due to the polarizer). The paper does not provide specific quantitative results on the image quality. However, the authors describe severe image degradation and visible artifacts due to diffraction effects. Using the diffraction MTF model developed in Chapter 3, we estimated that amplitude diffraction effects alone must have dropped the MTF contrast at $\xi = 0$ to 40% or less. Such marginal performance can be easily achieved and even surpassed using simpler and more compact equivalent conventional optics. In this instance, the fill factor of the SLM pixel was the main cause for the poor performance of the FOS.

The minimum width of the shadow mask is imposed by the TFT technology currently used in transmissive LC SLM devices, as illustrated in Figure 18. An obvious solution would be to further shrink the size of the electronics in order to reduce the mask width. However, although manufacturers of transmissive LCDs have recently reduced the width of the mask from 3.8 μm to 2.8 μm [49], any further significant reduction in the size of

the electronics seems unlikely, due to fundamental limitations in the current TFT fabrication technology.

Increasing the size of the aperture would not help increase the fill factor, as wavefront aberrations increase very fast (non-linearly) with the size of the aperture (or the inverse of the F/#). As discussed in the previous section, the spherical aberration increases with the cube of the aperture, coma increases with the square of the aperture, and astigmatism and field curvature increase linearly with the aperture. Therefore, in order to correct these larger aberrations, the resolution of the SLM would have to be increased by a factor larger than the increase in the aperture, which would actually result in a smaller fill factor.

Scaling up the entire system would not help increase the fill factor either, because wavefront aberrations also scale up with the focal length, so the SLM resolution has to be scaled up by approximately the same factor. Furthermore, scaling up the system would make it larger and heavier, opposing the main goal of optical foveated imaging, which is to reduce size and complexity of fast wide-angle optics.

Another solution is to decrease the resolution of the SLM as much as possible in order to increase the fill factor. However, this will increase the residual wavefront error (RWFE). As a result, the resolution of the transmissive LC SLM has to be carefully selected in order to optimize the FOS performance. If the SLM resolution is too low, the RWFE will affect the diffraction efficiency and MTF of the system. On the other hand, since the

minimum shadow mask width is limited by the current TFT technology, increasing the SLM resolution for a given aperture size will decrease the fill factor, also affecting the diffraction efficiency and MTF. Therefore, choosing the optimal SLM resolution is a tradeoff between minimizing the amplitude diffraction effects caused by the shadow mask, and minimizing the phase diffraction effects caused by the RWFE. Figure 40 illustrates the tradeoff between a low and a high SLM resolution.

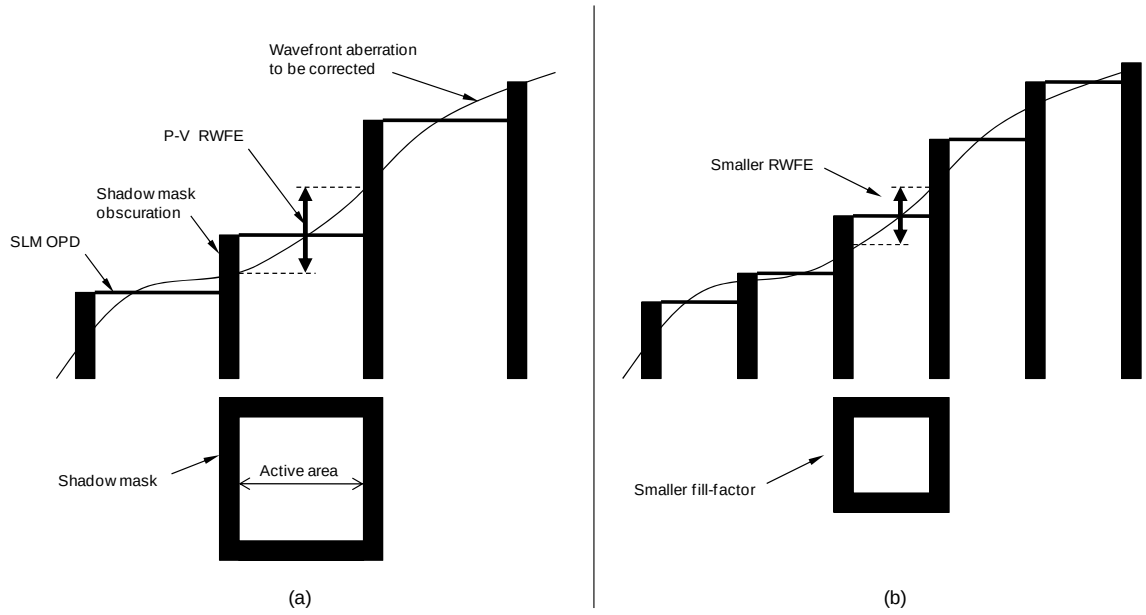

Figure 40: Design tradeoff in choosing the SLM resolution. (a) A lower SLM resolution results in a larger fill factor and a larger RWFE. (b) A higher SLM resolution results in a smaller fill factor and a smaller RWFE.

5.2.2 Practical Example

The four-element spherical lens design proposed in Section 4.3.1 was chosen to demonstrate a practical example of finding the optimal SLM resolution for a particular FOS. In this design, the SLM resolution was optimized based on the largest wavefront aberration, which occurs at the 40º field angle. The two-dimensional wavefront aberration map at the 40º field angle was obtained directly from Zemax, with five different sampling resolutions: 32×32, 64×64, 128×128, 256×256, and 512×512. As discussed in Section 5.1, the sampling resolution of the wavefront map represents the actual SLM resolution. The ratio $\frac{b}{a}$ was calculated from Equation (5-2), with the stop diameter, $D_{Stop} = 9.556$ mm, and considering a shadow mask width of $w = 2.8$ μm. The Zemax macro from Appendix C was used to calculate $\sigma_{0,0}$ and $MTF(\xi = 0)$ for the five different SLM resolution scenarios. Table 15 lists the pixel pitch, fill-factor, $\sigma_{0,0}$, and $MTF(\xi = 0)$, for the five SLM resolutions considered, with the ROI at 40º.

Table 15: Performance at the ROI with five different SLM resolutions (ROI at 40º).

SLM resolution	32×32	64×64	128×128	256×256	512×512
Pixel pitch in μm	300	150	75	37	19
Fill factor, $(b/a)^2$	0.98	0.96	0.93	0.85	0.73
$\sigma_{0,0}$	0.68	0.79	0.81	0.72	0.52
$MTF(\xi = 0)$	0.69	0.80	0.85	0.78	0.61

Figure 41 shows plots of $\sigma_{0,0}$ and $MTF(\xi = 0)$ versus N, where $N \times N$ is the SLM resolution. The optimal SLM resolution for this FOS design example is 128×128. For lower SLM resolutions, the phase diffraction caused by the RWFE is the main factor limiting the diffraction efficiency and the image quality at the ROI. For higher SLM resolutions, the amplitude diffraction caused by the shadow mask becomes the dominant factor affecting the performance of the FOS at the ROI.

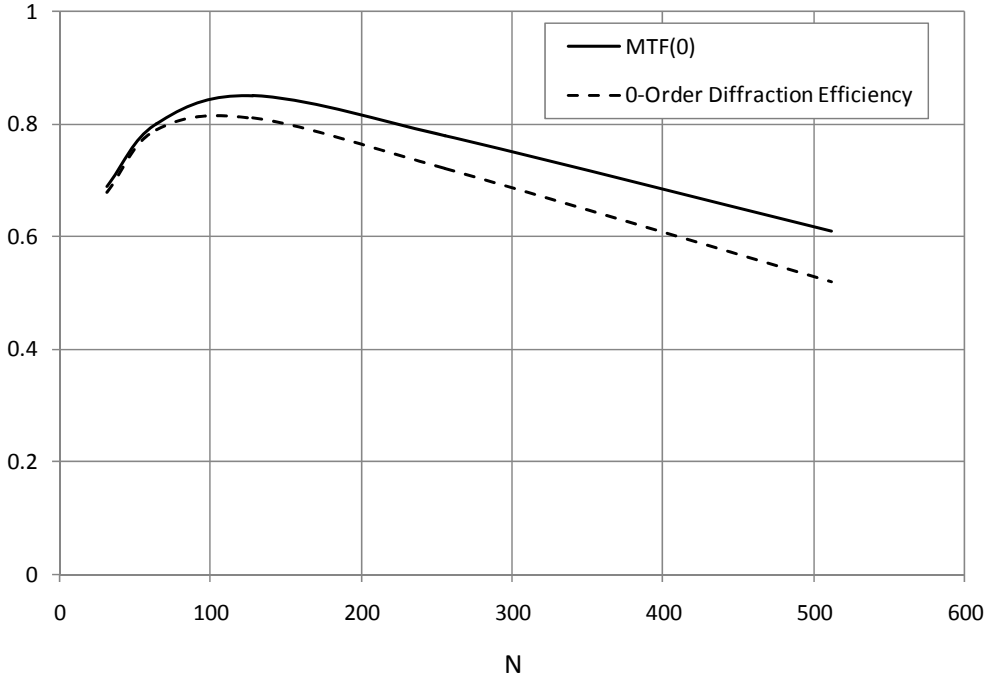

Figure 41: $\sigma_{0,0}$ and MTF at $\xi = 0$ versus N (ROI at 40º).

The zero-order diffraction efficiency and $MTF(\xi = 0)$ at the ROI were also calculated with the correction applied at 0º, 10º, 20º, and 30º, for an SLM resolution of 128×128 (listed in Table 16). Notice that the performance at the ROI is almost uniform across the

entire FOV, a result of the wavefront aberration being distributed somewhat evenly over the FOV.

Table 16: Performance at the ROI with correction at different field angles (128×128 SLM resolution).

Field angle in degrees	0º	10º	20º	30º	40º
$\sigma_{0,0}$	0.83	0.83	0.83	0.82	0.81
$MTF(\xi = 0)$	0.86	0.86	0.86	0.85	0.85

It is worth mentioning that, since both wavefront aberrations and pupil diameter scale lineraly with the focal length of the optical system, if a given FOS is scaled up or down while keeping the SLM resolution fixed, the MTF of the FOS will not change. Therefore, if an SLM is optimized for a specific lens design, the same SLM can be used with scaled-down versions of that lens, yielding systems with the same MTF as the original FOS.

5.3 MTF Performance

In this section, the overall image quality of the FOS design example proposed in the previous section is estimated, assuming an SLM resolution of 128×128 and a mask width of 2.8 μm. The lens has a circular aperture, so the MTF curve at the ROI can be directly

calculated from Equations (3-23) and (3-19), with $\xi_{cutoff} = \frac{1}{\lambda F/\#} = 671$ lp/mm and with the values for $MTF(\xi = 0)$ listed in Table 16.

Table 17: Zernike coefficients applied to the Zernike fringe phase surface to correct the aberration at five different field angles (ROI at 0º, 10º, 20º, 30º, and 40º).

	Config 1	Config 2	Config 3	Config 4	Config 5	Config 6
Z #	NO CORRECTION	ON-AXIS	10 DEGREES	20 DEGREES	30 DEGREES	40 DEGREES
1	0.00E+00	0.00E+00	0.00E+00	0.00E+00	0.00E+00	0.00E+00
3	0.00E+00	0.00E+00	0.00E+00	0.00E+00	0.00E+00	0.00E+00
4	0.00E+00	-5.83E-01	-3.76E-01	1.22E-01	5.61E-01	3.73E-01
5	0.00E+00	0.00E+00	9.09E-02	3.01E-01	4.27E-01	8.67E-02
8	0.00E+00	0.00E+00	2.97E-01	6.18E-01	9.73E-01	1.35E+00
9	0.00E+00	1.48E+00	1.42E+00	1.23E+00	9.36E-01	5.75E-01
11	0.00E+00	0.00E+00	4.02E-02	3.27E-01	1.13E+00	2.77E+00
12	0.00E+00	0.00E+00	6.69E-03	1.36E-02	-2.14E-02	-1.78E-01
15	0.00E+00	0.00E+00	1.36E-01	2.88E-01	4.68E-01	6.70E-01
16	0.00E+00	-1.33E-01	-1.39E-01	-1.59E-01	-1.95E-01	-2.49E-01
17	0.00E+00	0.00E+00	9.63E-04	1.56E-02	8.08E-02	2.62E-01
20	0.00E+00	0.00E+00	2.55E-04	2.94E-03	1.55E-02	5.87E-02
21	0.00E+00	0.00E+00	6.10E-03	2.54E-02	6.03E-02	1.12E-01
24	0.00E+00	0.00E+00	1.31E-02	2.96E-02	5.41E-02	9.26E-02
25	0.00E+00	-2.07E-03	-2.40E-03	-3.55E-03	-6.20E-03	-1.18E-02
27	0.00E+00	0.00E+00	-2.26E-05	-7.39E-04	-5.79E-03	-2.53E-02
28	0.00E+00	0.00E+00	6.89E-06	1.69E-04	1.44E-03	7.80E-03
31	0.00E+00	0.00E+00	-2.08E-04	-1.75E-03	-6.29E-03	-1.57E-02
32	0.00E+00	0.00E+00	4.17E-04	1.95E-03	5.58E-03	1.35E-02
35	0.00E+00	0.00E+00	4.98E-05	2.49E-04	9.59E-04	3.18E-03
36	0.00E+00	1.14E-04	1.27E-04	1.63E-04	1.95E-04	9.33E-05
37	0.00E+00	7.14E-06	9.38E-06	1.80E-05	3.92E-05	8.02E-05

Zemax can be used to evaluate the MTF at the uncorrected field angles when the correction applied at the ROI, following the method described in Section 5.1.3. A Zernike phase surface was placed at the stop to simulate the OPD introduced by the SLM. The Zernike coefficients for the aberration at 0º, 10º, 20º, 30º, and 40º were obtained from Zemax, and then placed in separate configurations in the *multiple configuration editor*.

The multiple configuration editor is a feature in Zemax allowing the user to change only certain parameters in the lens design while keeping everything else constant. Table 17 lists the coefficients applied to the Zernike phase surface to simulate the SLM correction at the five different field angles. In this case, toggling between configurations simulates the repositioning of the ROI at different field angles within the FOV.

Table 18 lists the zero-order diffraction efficiency, $MTF(\xi = 0)$, and the wavefront aberration at different field angles when correction is applied at 40º. Notice that, even 5º away from the ROI, at the 35º field angle, $\sigma_{0,0}$ and $MTF(\xi = 0)$ do not change significantly. However, aberrations in fast wide-angle lenses change rapidly with the field angle. As a result, aberrations become the dominant factor affecting the image quality away from the ROI. Figure 42 shows the estimated MTF of the FOS with the wavefront aberration corrected at 40º.

Table 18: Performance with correction applied at 40º (128×128 SLM resolution).

Field angle in degrees	40º	39º	35º	0º	– 40º
Zero-order efficiency, $\sigma_{0,0}$	0.81	0.81	0.81	0.83	0.81
MTF at $\xi = 0$	0.85	0.85	0.85	0.86	0.85
RMS aberration in waves	0	0.09	0.39	1.40	2.43
P-V aberration in waves	0	0.56	2.50	8.91	17.8

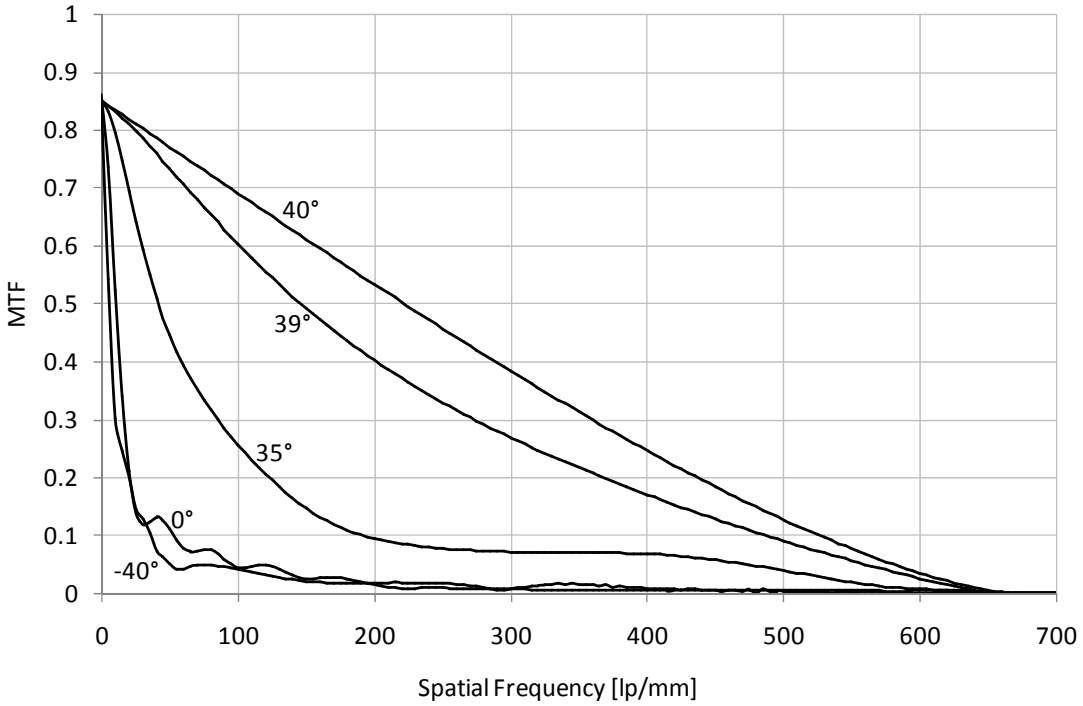

Figure 42: MTF with wavefront aberration corrected at 40º.

The size of the ROI at a certain field angle can be defined as the small FOV centered on that field angle within which the MTF contrast is larger than a specified value up to a fixed spatial frequency when correction is applied at the ROI. The size of the ROI has to be determined at different field angles within the FOV in order to estimate the minimum number of field angles where the aberration has to be evaluated and programmed into the SLM electronics. For this example, the size of the ROI was evaluated at 0º, 10º, 20º, 30º, and 40º, assuming that the MTF contrast within the ROI has to be larger than roughly 0.20 up to 300 lp/mm. Figure 43 to Figure 47 show the MTF at the center of the ROI and the MTF at the edge of the ROI, with the ROI at 0º, 10º, 20º, 30º, and 40º, respectively. The size of the ROI versus field angle is plotted in Figure 48. Notice that the size of the ROI decreases towards the peripheral angles.

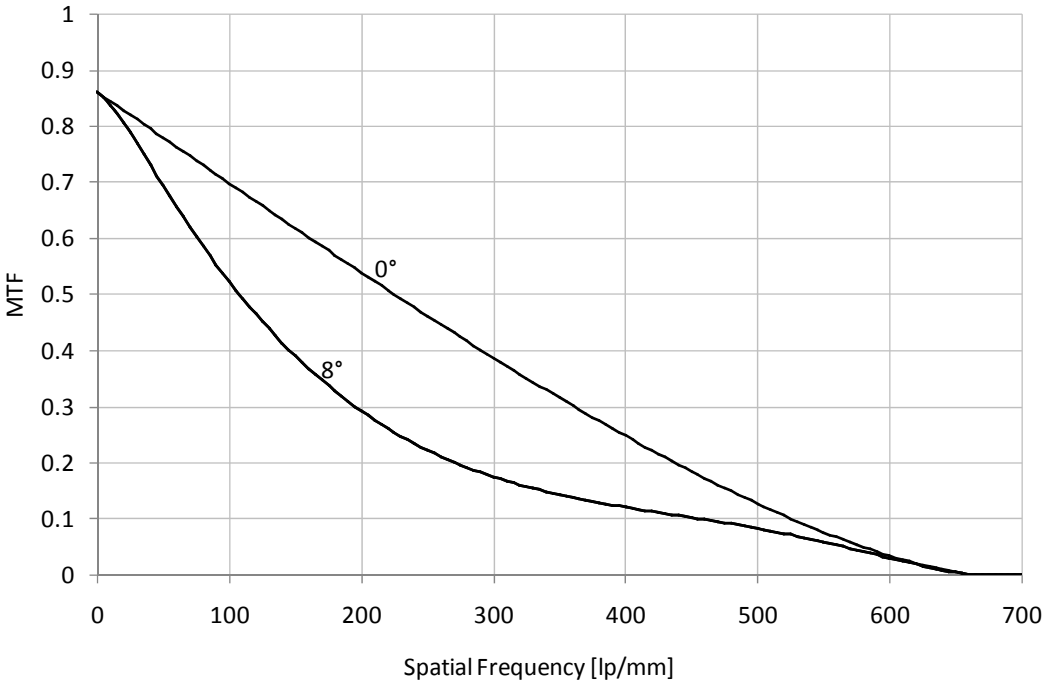

Figure 43: ROI at 0º.

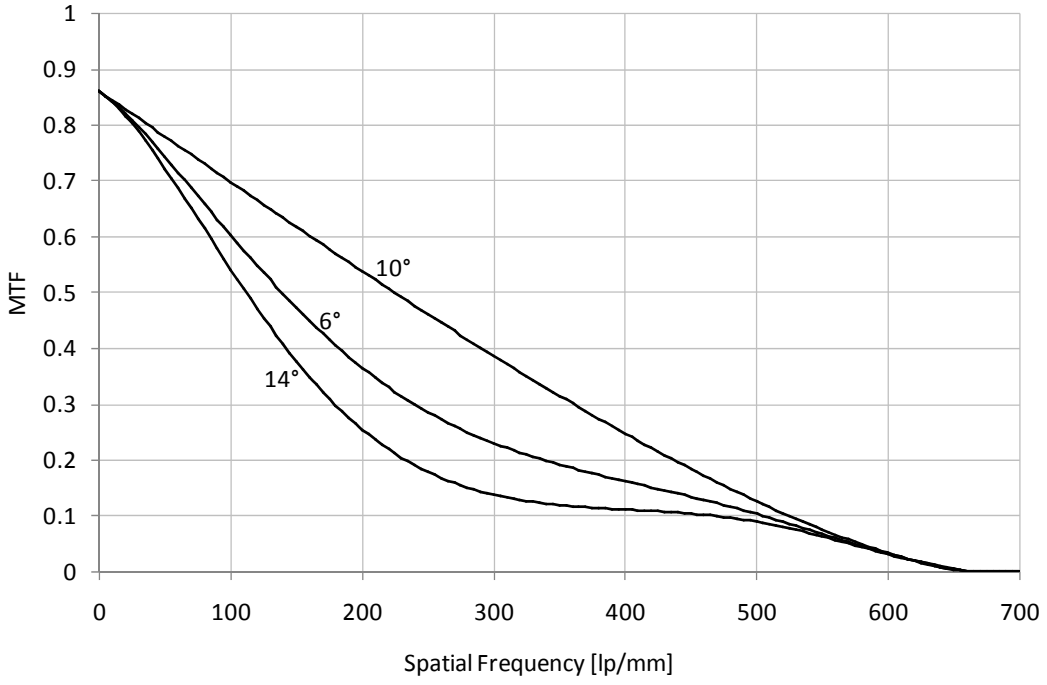

Figure 44: ROI at 10º.

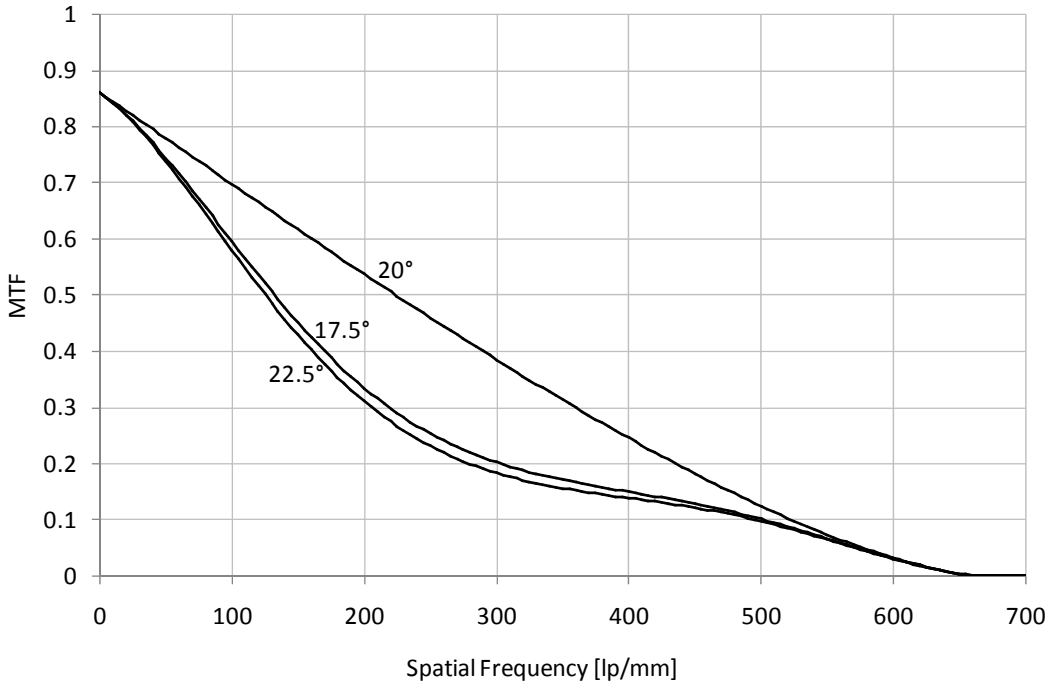

Figure 45: ROI at 20º.

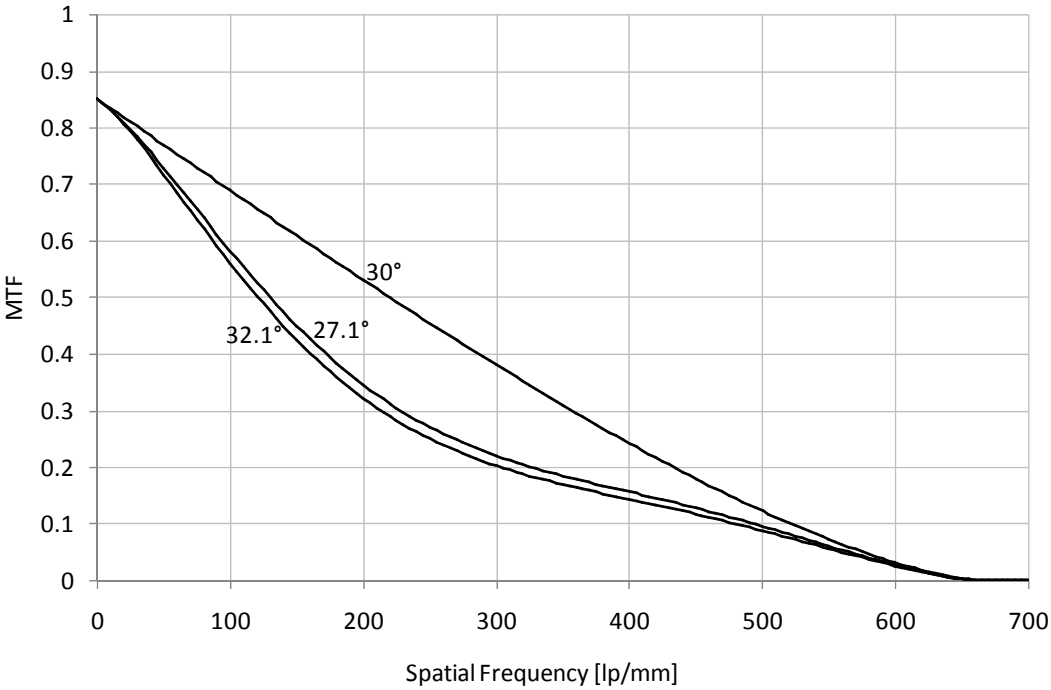

Figure 46: ROI at 30º.

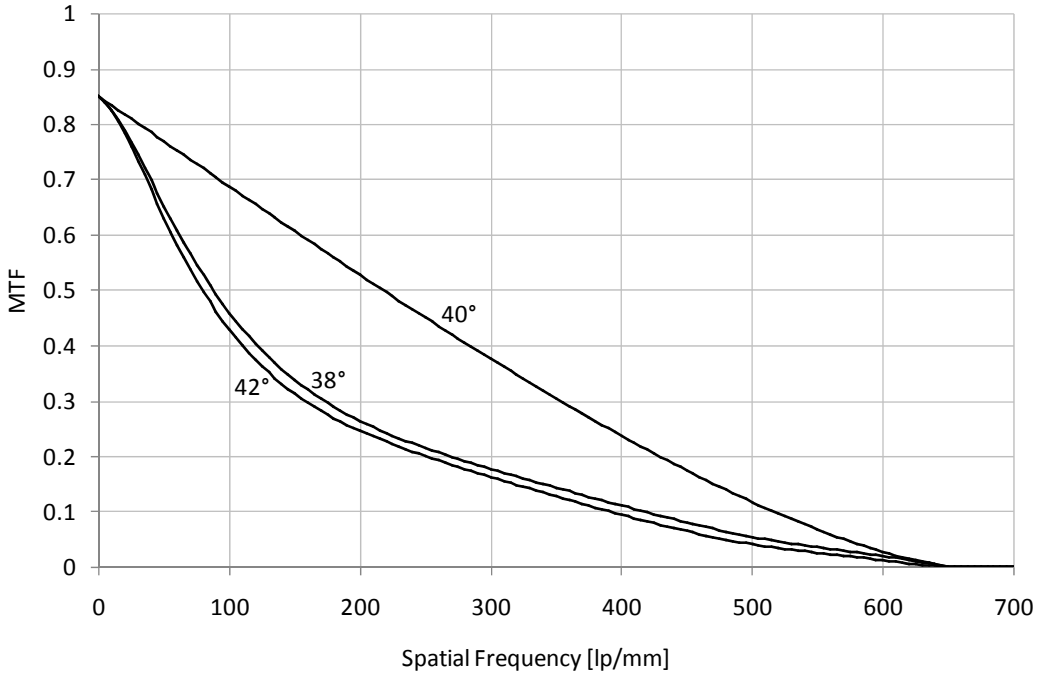

Figure 47: ROI at 40º.

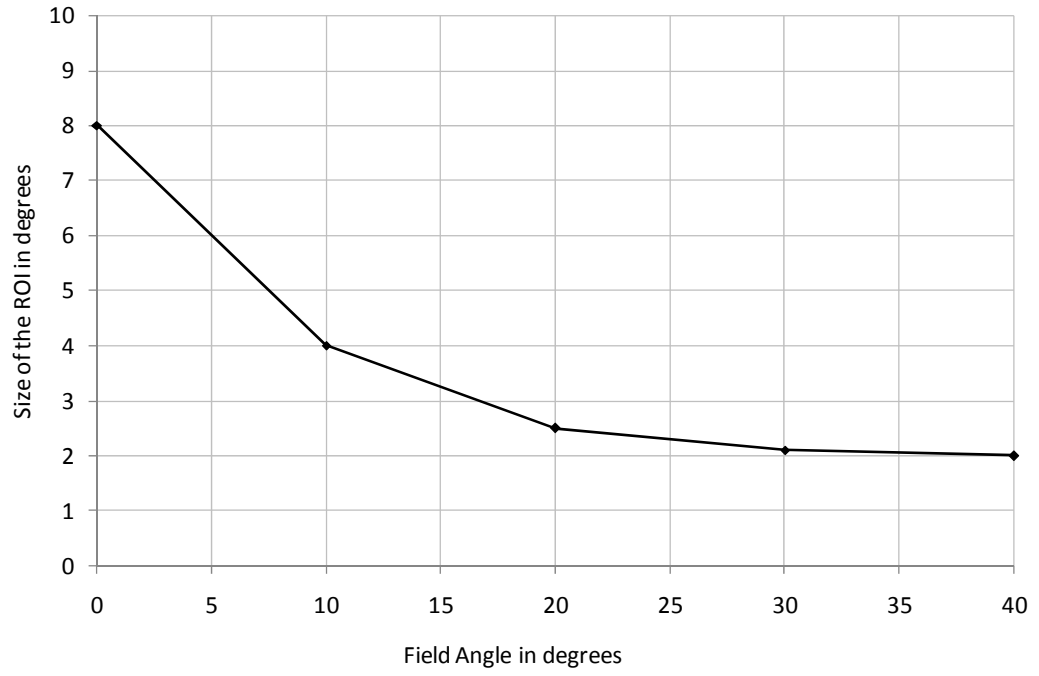

Figure 48: Size of the ROI versus field angle.

5.4 Tolerances and Calibration

There are three main factors affecting the image quality in optical systems: diffraction, aberrations left uncorrected by design, and additional aberrations caused by fabrication and assembly errors. Until now, we have only taken in to consideration the first two factors, ignoring the aberrations caused by the fabrication and assembly errors. Although these aberrations do not have a significant effect on the image quality in the case of slow optical systems (F/7 and larger), they can significantly affect the final performance of the manufactured lens in the case of fast optical systems.

The sensitivity of an optical system to fabrication and assembly errors depends primarily on the F/#, wavelength, and design. In general, faster lenses (lower F/#) and systems operating at lower wavelengths are more sensitive to errors. Also, designs with relatively large incidence angles at an optical surface are sensitive to the fabrication errors of that particular surface. Since fast wide-angle lenses used in FOSs are designed with a limited number of elements, marginal rays in the pupil and rays in the peripheral fields typically end up having rather large incidence angles at the optical surfaces. As a result, these lenses tend to be very sensitive to fabrication and assembly errors.

On the other hand, a great advantage of FOSs is that, besides correcting the nominal wavefront aberrations, these systems also have the ability to correct any additional

aberrations introduced by fabrication and assembly errors. The SLM can be calibrated across the entire FOV by measuring the actual wavefront of the manufactured lens at all field angles to be programmed into the SLM and adjusting the OPD of the SLM at each field angle.

This section analyzes the effects of fabrication and assembly errors on the image quality of fast wide-angle lenses. The four-element lens design is used as an example. A calibration method to eliminate additional aberrations introduced by these errors is suggested.

5.4.1 Optical Fabrication and Assembly Errors

The possible optical fabrication errors in a refractive element are surface power, surface irregularity, glass center thickness (CT), refractive index, wedge, and decenter. The power error of an optical surface is the deviation in the radius of curvature from the nominal prescription. The irregularity error is the deviation of the fabricated surface from the nominal shape, with the power removed. Power and irregularity are usually specified in fringes due to the typical optical surface test methods (interferometry or test plates). The glass CT error is the deviation of the distance between the two vertexes of the element from the nominal prescription. The index of refraction error is the deviation of the refractive index of the glass at a certain wavelength, as well as the deviation of the dispersion (Abbe number).

The wedge error is the tilt of one optical surface with respect to the other, and the decenter is the offset of one optical surface with respect to the other. In the case of spherical optics, we do not have to take into consideration the surface-to-surface decenter since both surfaces are spherical and do not have a fixed center of rotational symmetry. Any point on a sphere can be considered a center of rotational symmetry. As a result, a decenter error in the fabrication of a spherical element will appear as wedge after the edging process. Therefore, only a wedge tolerance should be specified for a spherical refractive element. However, surface-to-surface decenter should be toleranced separately for an element with two aspheric surfaces.

The possible optical assembly errors in a lens are air gap CT, element tilt, and element centration. The air gap CT error is the deviation in the air gap distance between the vertexes of two adjacent elements. The element tilt error is the tilt of an element around X or Y with respect to the mechanical axis. The element centration error is the offset of an element on X or Y with respect to the mechanical axis. Element tilt and centration are sometimes used as *compensators* in ultra-precision optics, in order to reduce the effect of optical fabrication wedge in spherical elements.

Table 19 shows typical optical fabrication and assembly tolerances for visible optics with diameters between 10 and 30 mm, which is the typical size for foveated imaging optics. The cost of the optics usually varies significantly with the tolerances. Also, very tight

tolerances are not always manufacturable, especially in cases with challenging aspect ratios or surface shapes, or when all the tolerances on one element are very tight.

Table 19: Typical optical fabrication and assembly tolerances for 10-30 mm visible optics.

Tolerance	Standard	Precision	Ultra-Precision
Power/Irregularity	5/2 fringes	3/1 fringes	1/0.5 fringes
Glass CT	0.100 mm	0.050 mm	0.020 mm
Wedge	6 arcmin	2 arcmin	1 arcmin
Index / Abbe #	0.001 / 2%	0.0001 / 0.5%	Melt index
Air CT	0.100 mm	0.050 mm	0.020 mm
Element Tilt	6 arcmin	2 arcmin	1 arcmin
Element Centration	0.100 mm	0.020 mm	0.005 mm

5.4.2 Monte-Carlo Tolerance Analysis

Establishing tolerances for the fabrication and assembly errors is a very important step in finalizing the optical design, as tolerances will significantly affect the wavefront aberrations resulting from these errors, and also determine the manufacturability, method of fabrication, and cost of the optics. Since fabrication and assembly errors are non-deterministic, a *Monte-Carlo tolerance analysis* is required to evaluate statistically the expected performance of the manufactured optical systems.

The Monte-Carlo (MC) tolerance analysis is a powerful lens design tool, currently available in most optical computer-aided design software. It computes the statistics of a given *merit function* when random perturbations are applied to the nominal design. These perturbations simulate all the possible fabrication and assembly errors that can occur during the manufacturing process. The lens designer can define these errors, their tolerances and distribution, the merit function, the compensators, and the number of MC trials. All the manufacturing errors and their typical tolerances described in the previous section can be modeled in the tolerance analysis. The distribution defines the probability of deviation from nominal design for each error, and can be normal (Gaussian), uniform, or defined by the user. The merit function is the criterion considered for the analysis. For instance, common merit functions are the wavefront error, the spot size, the MTF contrast at a certain spatial frequency, etc. Merit functions can also be a weighted combination of several different criteria defined and customized by the user. Compensators are design parameters that can be optimized in order to balance the other errors and minimize the merit function. Compensators are usually chosen such that they can be adjusted during the optical assembly process: back focal distance, air gaps, and element tilt and centration.

For each MC trial, the analysis program applies random perturbations to the optical system according to the tolerances and distributions defined by the lens designer. Then, the program reevaluates the merit function and optimizes the compensators to minimize the merit function. At the end of the analysis, the results are listed in a report indicating the worst-case scenario, best-case scenario, yield, and other useful statistical values. The

accuracy of the results increases with the number of MC trials. The program can also compute the sensitivity of the optical system to individual errors. The sensitivity analysis helps the lens designer understand which errors have the most significant impact on the merit function. If the results are not acceptable, the tolerances can be adjusted (tightened or loosened) depending on the sensitivity analysis. This process can be repeated until acceptable results are achieved.

5.4.3 Effect of Tolerances in a Fast Wide-Angle FOS

The same four-element spherical lens design was used as an example in order to analyze the effect of fabrication and assembly tolerances on the image quality of a fast wide-angle FOS, considering the tolerances listed in Table 20. These tolerances are relatively tight for the 25 mm diameter optics in this design. The merit function criterion for the MC tolerance analysis was set to be the RMS wavefront aberration, equally weighted across the FOV at five different field angles: 0º, 10º, 20º, 30º, and 40º. The multiple configuration Zemax model used previously in Section 5.3 was also used in this example. A tolerance analysis with 100 random MC trials was run for Configuration 1 in Table 17 (without applying any correction OPD to the SLM). The analysis was run using a normal (Gaussian) distribution for the manufacturing errors, without adjusting any compensators. A summary of the tolerance analysis results is listed in Appendix D.

Table 20: Fabrication and assembly tolerances.

Power/Irregularity	2/1 fringes
Glass CT	± 0.020 mm
Wedge	1.8 arcmin
Index	± 0.0001
Air CT	± 0.020 mm
Element Tilt	1.8 arcmin
Element Centration	0.020 mm

A random MC trial with the merit function close to the 50% percentile margin was chosen as a model for a typical manufactured lens. The 128×128 wavefront map was obtained from this model at the five field angles considered. The zero-order diffraction efficiency, $\sigma_{0,0}$, and $MTF(\xi = 0)$ were calculated using the Zemax macro in Appendix C. Table 21 lists the uncorrected wavefront aberrations, $\sigma_{0,0}$, and $MTF(\xi = 0)$ at 0º, 10º, 20º, 30º, and 40º.

Table 21: Performance at the ROI of a typical manufactured FOS.

Field angle in degrees	0º	10º	20º	30º	40º
RMS aberration in waves	0.70	0.65	0.72	0.98	1.31
P-V aberration in waves	2.74	2.44	3.70	5.39	8.42
Zero-order efficiency, $\sigma_{0,0}$	0.83	0.83	0.83	0.82	0.81
MTF at $\xi = 0$	0.86	0.86	0.86	0.85	0.85

The uncorrected wavefront aberrations in this typical manufactured lens are very close to the nominal aberrations listed in Table 5. In fact, aberrations at some field angles are slightly smaller than the nominal values, which is not unusual in optical systems with large nominal aberrations. The values for $\sigma_{0,0}$ and $MTF(\xi = 0)$ are identical to the nominal values listed in Table 16. So, fabrication and assembly tolerances do not have a significant effect on the diffraction efficiency of the FOS. This result was somewhat predictable, because in general, very aberrated optical systems are not sensitive to errors.

On the other hand, manufacturing errors can significantly affect the MTF of very well corrected optical systems, such as a fast FOS at the ROI. The FOS becomes very sensitive to errors when the aberration is corrected at the ROI. For instance, if the SLM of a fast wide-angle FOS is programmed to correct the aberrations obtained from the nominal lens design, the manufactured FOS will not have the expected diffraction-limited image quality at the ROI. Table 22 lists the additional aberrations caused by the errors in the typical manufactured lens when the nominal aberrations are corrected at the ROI. Note that the aberration at the ROI is not even close to the diffraction-limit. The MTF of the typical manufactured lens model is shown in Figure 49 with the nominal aberration corrected at 40º (Configuration 6 in Table 17). There is almost no difference between the MTF at the ROI and the MTF at the uncorrected field angles.

Table 22: Aberrations at the ROI caused by manufacturing errors.

Field angle in degrees	0º	10º	20º	30º	40º
RMS aberration in waves	0.30	0.34	0.38	0.40	0.41
P-V aberration in waves	1.38	1.61	1.81	1.93	1.94

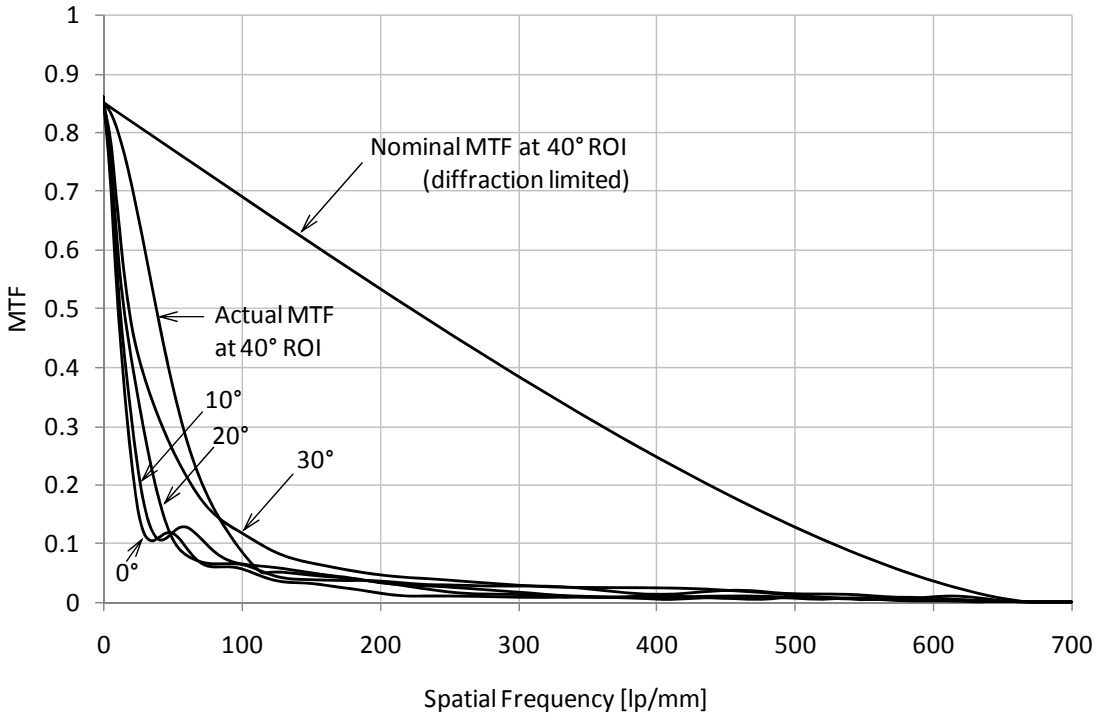

Figure 49: MTF with the ROI at 40º for a typical manufactured FOS.

5.4.4 Calibration

To obtain diffraction limited MTF at the ROI in the manufactured FOSs, the additional aberrations caused by fabrication and assembly errors have to be measured and corrected by adjusting and re-programming the OPD of the SLM. The SLM has to be reprogrammed at all field-angles with an adjusted wavefront aberration, $W' = W + W_{Errors}$, where W is the aberration obtained from the nominal design and pre-programmed into

the SLM, and W_{Errors} is the additional aberration caused by manufacturing errors, measured at the ROI with the nominal correction applied to the SLM.

However, additional aberrations introduced by fabrication and assembly errors are not rotationally symmetric about the optical axis, and they also vary with the field angle in fast wide-angle lenses. As a result, if the SLM is reprogrammed at all field angles with the same additional aberration, W_{Errors}, measured at a single field angle, the MTF at other field angles will be affected by aberrations.

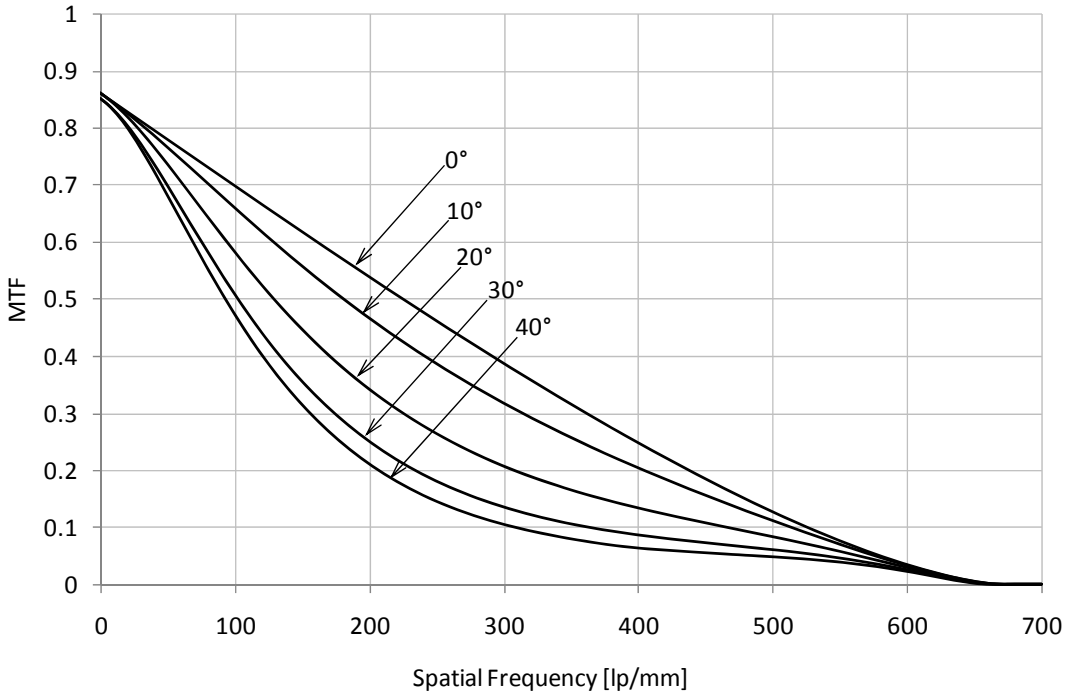

Figure 50: MTF at the ROI with calibration on-axis.

As an example, in the previous typical manufactured lens model, an additional Zernike phase surface was introduced next to the already existing phase surface in order to

simulate the OPD adjustment for the SLM calibration. The Zernike coefficients in this additional phase surface were set to cancel the additional aberration caused by manufacturing errors at 0º, simulating on-axis calibration only. Figure 50 shows the MTF at the ROI at 0º, 10º, 20º, 30º, and 40º, with calibration at 0º.

So, in order to obtain uniform image quality performance across the entire FOV, a fast wide-angle FOS has to be calibrated at several field angles within the FOV. The flow-chart diagram in Figure 51 illustrates the fundamental steps in the design, tolerancing, and calibration of a fast wide-angle FOS.

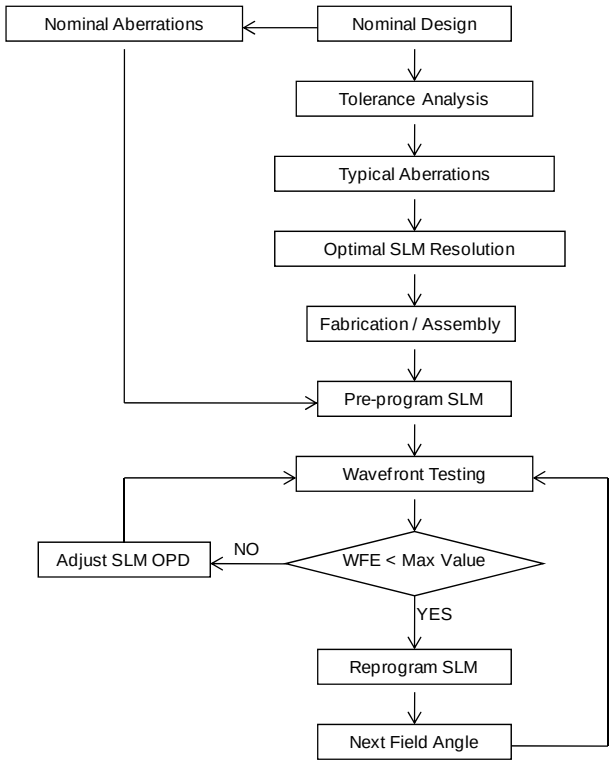

Figure 51: FOS design, tolerancing, and calibration steps.

5.5 Equivalent Conventional Lens

The zero-order diffraction efficiency in the FOS design example developed in this chapter is roughly 82%. Furthermore, although polarization independent devices have been developed [44,50,51], most LC SLM devices available commercially are polarization dependent, so they introduce an additional loss of roughly 50%. As a result, the total transmission of the FOS with a polarization dependent SLM would only be about 41%. From a radiometric point of view, such a significant transmission loss is equivalent to closing down the aperture of the lens. Since the transmission of a lens is proportional to $\left(\frac{1}{F/\#}\right)^2$, our F/2.8 FOS is equivalent to an F/4.4 conventional monochromatic lens in terms of transmission.

This simple "back-of-the-envelope" calculation leads to the inevitable question whether optical foveated imaging based on the current transmissive LC SLM technology has any major advantage over conventional wide FOV imaging optics. An F/4.4 lens would be less aberrated, less sensitive to tolerances, and more compact than an F/2.8 lens. Therefore, it would be interesting to design an equivalent slower conventional lens and compare it to the FOS in terms of image quality.

The equivalent monochromatic F/4.4 lens was designed by closing down the aperture in the original F/2.8 lens design. The optics was reoptimized, keeping the same retrofocus configuration, with the stop between the first and the second element. The design wavelength, EFL, and FOV were left unchanged. The prescription data is given in Table

23. The design layout, largest aberration, distortion, and relative illumination plots are shown in Figure 52. The overall length of this slower equivalent conventional lens is 48 mm (almost 25% shorter than the FOS).

Table 23: Prescription – equivalent F/4.4 conventional lens (all dimensions in mm).

Surf:Type		Comment	Radius	Thickness	Glass	Semi-Diameter
OBJ	Standard		Infinity	Infinity		Infinity
1	Standard		Infinity	10.000000		0.000000
2*	Standard	1st Element	9.669574	2.700000	BK7	5.500000
3*	Standard		5.189104	2.784330		4.000000
STO*	Standard	Filter	Infinity	0.900000	F_SILICA	3.500000
5*	Standard		Infinity	5.210320		3.500000
6*	Standard	2nd Element	-10.605560	4.200000	BK7	6.000000
7*	Standard		-8.246875	0.200000		7.500000
8*	Standard	3rd Element	-930.042202	3.600000	BK7	11.000000
9*	Standard		-22.588394	0.200000		11.000000
10*	Standard	4th Element	35.293356	3.600000	BK7	12.000000
11*	Standard		-248.560310	24.536467		12.000000
IMA	Standard	Image Plane	Infinity	-		12.132754

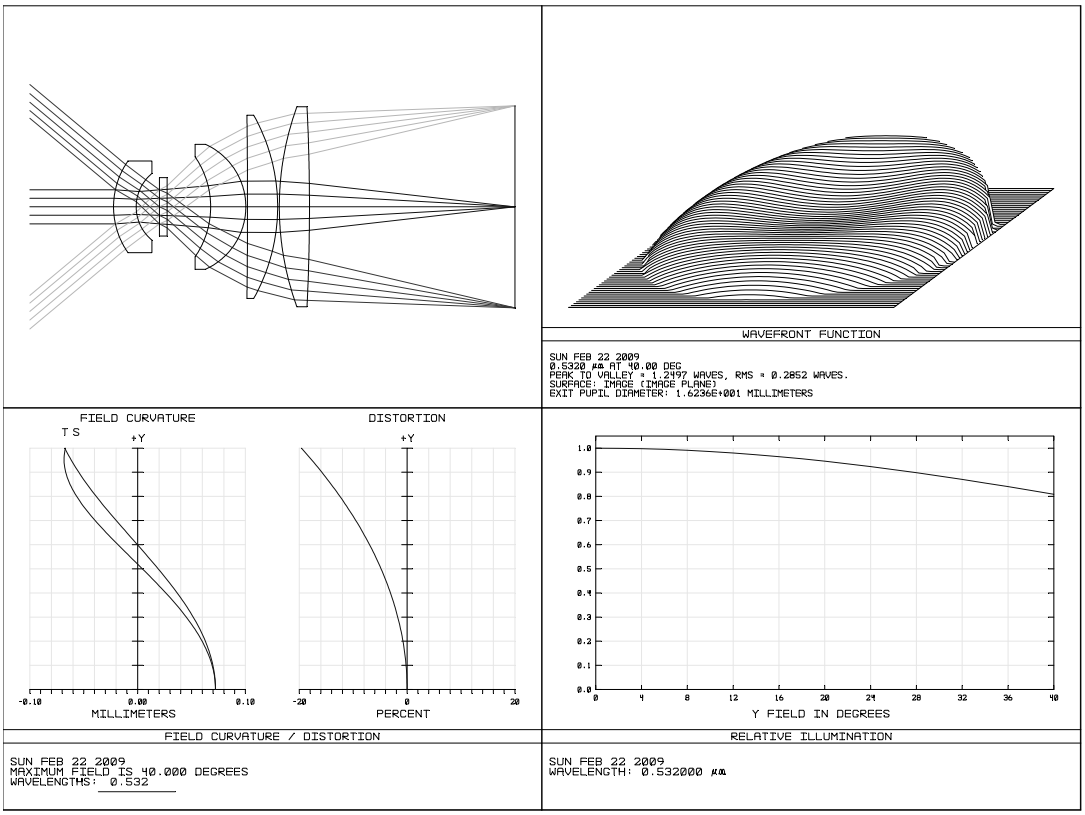

Figure 52: Equivalent F/4.4 conventional lens.

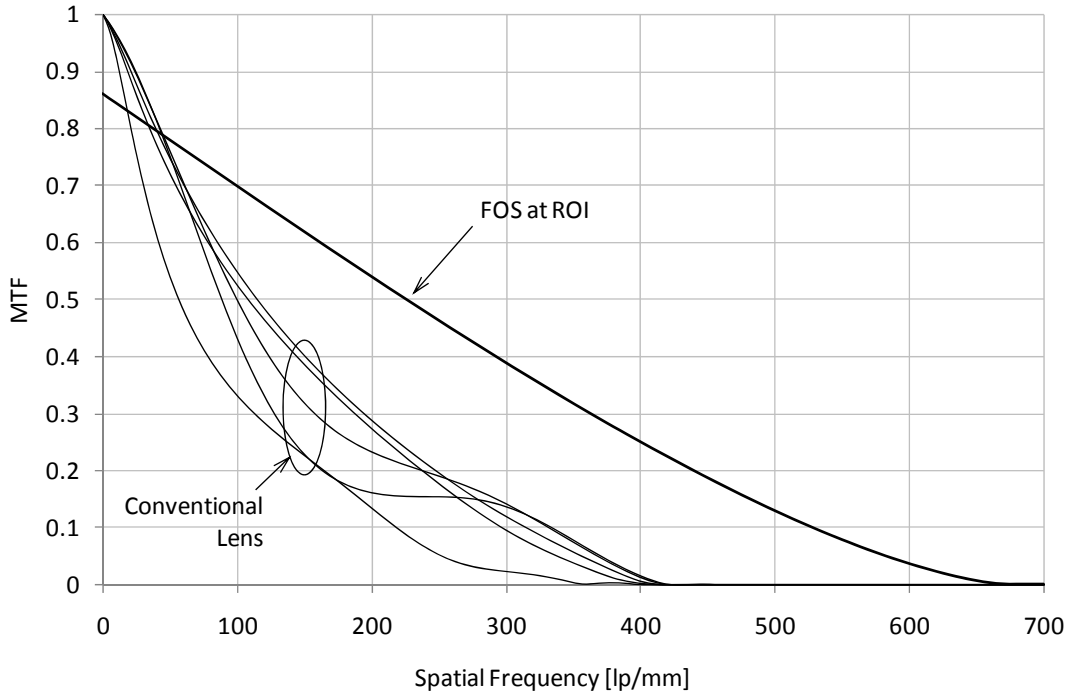

Figure 53: MTF of the FOS at the ROI (40% transmission) compared to the MTF of an equivalent F/4.4 conventional lens.

The MTF of a typical manufactured F/4.4 lens was estimated by running a MC tolerance analysis with the same set of tolerances specified in Table 20. A random trial with the merit function close to the 50% percentile margin was chosen as the model for a typical manufactured lens. Figure 53 compares the MTF of the typical manufactured equivalent conventional lens model to the MTF of the FOS at the ROI, assuming the FOS was calibrated to eliminate aberrations caused by manufacturing errors. The equivalent conventional lens performs better at lower spatial frequencies, up to about 40 lp/mm. On the other hand, the MTF of the conventional lens drops steeper, due to a shorter cutoff spatial frequency and larger aberrations. So, at higher spatial frequencies, the MTF of the FOS at the ROI is higher than the MTF of the conventional lens.

The resolution of a digital imaging system is also limited by the resolution of the sensor array. A high optical MTF at very high spatial frequencies is not always desirable, as aliasing artifacts due to sensor under-sampling can become a problem if the cutoff of the optical MTF is much larger than the Nyquist frequency of the sensor array [53]. This problem can be somewhat alleviated in digital imaging systems by using an optical low-pass filter in front of the sensor in order to limit the cutoff spatial frequency of the optical system.

5.6 General System Design Considerations

In general, for an imaging system, a set of requirements, specifications, and constraints need to be defined before starting the actual design work. The performance specifications of the system have to be determined starting from the application requirements. There are several relationships and tradeoffs between the application requirements, the system specifications, and the complexity of the lens design. This section covers basic concepts and tradeoffs in a typical visible imaging system design using a sensor array with a fixed magnification wide-angle lens.

Figure 54 illustrates the image formation of an extended object through an optical system. The magnification M is defined as

$$M = -\frac{q}{p} \xrightarrow{p >> f} -\frac{f}{p} \tag{5-6}$$

where p is the distance from the object to the lens, q is the distance from the lens to the image plane, and f is the focal length of the lens. When p approaches infinity, or $p >> f$, q approaches f. The object distance p, full object height h, and resolution requirements of the imaging system are usually set by the application requirements. That is, how far we need to detect, how much field we want to cover, and what is the smallest feature we want to resolve. The resolution requirements for the application can be specified in terms of the maximum spatial frequency that needs to be resolved in object space, $\xi_{\max}$.

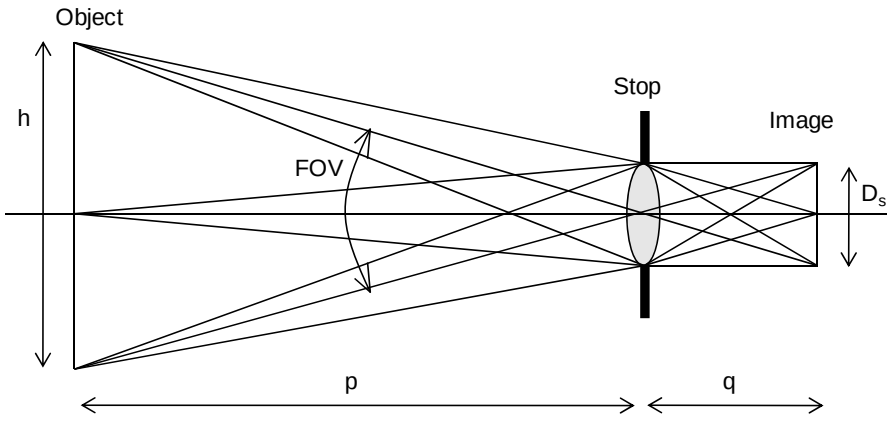

Figure 54: Imaging of an extended object through an optical system.

5.6.1 The Sensor

The sensor array should be able to resolve the maximum resolution required by the application. Therefore, with a distortion-free lens, the minimum required Nyquist

frequency of the sensor in image space, $\xi_{Nyquist}$, is given by the maximum resolvable spatial frequency in object space and the magnification of the optical system:

$$\xi_{Nyquist} = \frac{\xi_{\max}}{|M|} \tag{5-7}$$

In the case of extreme wide-angle lenses, where negative (barrel) distortion could be quite large, the Nyquist frequency has to be larger than specified in Equation (5-7), to avoid aliasing due to the significant decrease in magnification towards the peripheral FOV. Distortion is an off-axis error in the magnification of the optical system, and occurs due to an asymmetrical arrangement in the optical design. Distortion in wide-angle lenses typically increases faster towards the peripheral fields, varying with the cube of the field angle. As a result, the maximum magnification error due to distortion has to be taken into consideration when calculating the minimum required Nyquist frequency of the sensor array:

$$\xi_{Nyquist} = \frac{\xi_{\max}}{|M| \times (1 - distortion)} \tag{5-8}$$

Equation (5-8) led us to the idea of a new image sampling concept that could improve efficiency in foveated imaging systems using wide-angle lenses with large negative distortion. The idea is to apply another non-uniform resolution sampling algorithm in addition to the foveation algorithms in order to account for the drop in magnification with the field angle. Sampling could be done at a lower resolution throughout most of the

FOV, except for the peripheral field angles, where sampling should be done at a higher resolution to reduce aliasing effects due to the significant drop in magnification. Figure 55 illustrates an example of efficient non-uniform image sampling in a foveated imaging system using a wide-angle lens with large negative distortion. Since distortion remains constant with time, this additional non-uniform resolution sampling would be a static algorithm superimposed onto the dynamic foveation algorithms. This new concept could further improve efficiency in wide-angle foveated imaging systems, speeding up transmission rate, without giving up resolution towards peripheral fields. If no significant loss of resolution occurs due to aliasing, distortion can also be calibrated and eliminated at the image processing stage by stretching out the image according to the paraxial magnification of the lens.

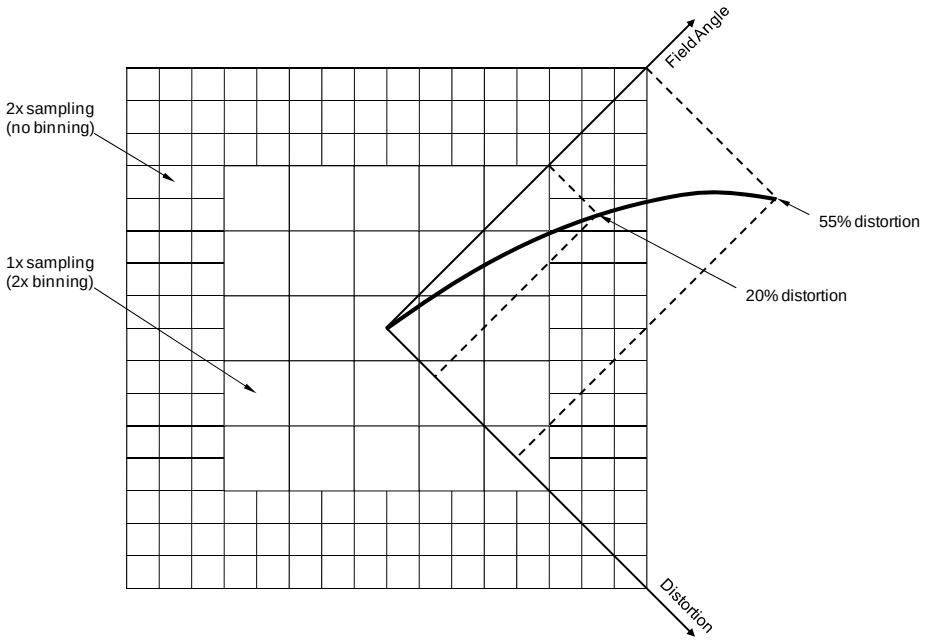

Figure 55: Example of efficient sampling in a foveated imaging system with 55% negative distortion: 2× pixel binning up to 20% distortion, and no binning from 20% up to 55%.

The Nyquist frequency of a contiguous sensor array is given by the pixel pitch [53]:

$$\xi_{Nyquist} = \frac{1}{2 \times (pixel\ pitch)} \tag{5-9}$$

There are several sensor formats, with different pixel sizes, based on CMOS or CCD technologies. As discussed previously in Chapters 1 and 2, in the case of foveated imaging applications, CMOS sensors are more suitable than CCD sensors, due to their lower power consumption and hardware design versatility. As discussed before, the sensor array should be able to resolve the maximum resolution required for the application, therefore the minimum resolution of the array is given by

$$N_s = 2\xi_{\max} h \tag{5-10}$$

where N_s is the number of rows in the sensor array. The size of the sensor array is given by the number of pixels in a row and the pixel pitch:

$$D_s = N_s \times pixel\ pitch \tag{5-11}$$

Equations (5-6), (5-8), (5-9), (5-10), and (5-11) can be combined in a general equation relating the sensor format to the optics and the application requirements:

$$D_s = \frac{h\,f}{p}\left(1 - distortion\right) \tag{5-12}$$

Now, let us consider the reverse situation, where we have a given imaging system, with a certain sensor and matching lens, and we would like to determine the object height and the maximum resolvable spatial frequency in object space in terms of object distance and imaging system specifications (sensor size, pixel pitch, focal length, and distortion). From Equation (5-12), the object height is given by the following expression:

$$h = p\frac{D_s}{f\left(1 - distortion\right)} \tag{5-13}$$

Assuming the lens can resolve spatial frequencies higher than the Nyquist frequency of the sensor array, the maximum resolvable spatial frequency in object space can be determined by replacing *h* in Equation (5-10) by the expression in Equation (5-13):

$$\xi_{\max} = \frac{1}{p}\frac{f\left(1 - distortion\right)}{2 \times pixel\ pitch} \tag{5-14}$$

5.6.2 The Optics

From Equation (5-12) it is evident that choosing the focal length is an important tradeoff in the system design. The sensor format and the size of the entire system scale with the

focal length of the lens. For a larger focal length, the sensor pixels can be larger, and therefore sensitivity is increased relative to noise. Also a larger focal length means a larger pupil, which would allow the use of a larger transmissive LC SLM. On the other hand, a smaller and lighter system is desirable in many applications (the main purpose of optical foveated imaging is to reduce the size and complexity of the optics). Also, a larger SLM does not guarantee a larger fill factor, as wavefront aberrations increase proportionally with the focal length of the optical system, so the resolution of the SLM would have to be increased in order to correct higher aberrations.

The minimum angular FOV of the system is determined by the application requirements:

$$FOV = 2\tan^{-1}\left(\frac{h/2}{p}\right) \tag{5-15}$$

Wavefront aberrations in a lens increase significantly with the field angle. For instance, if we consider the third order Seidel aberrations in an uncorrected lens, coma is proportional to the field angle, astigmatism and field curvature are proportional to the square of the field angle, and distortion is proportional to the cube of the filed angle.

The lens F/# is imposed in general by the application requirements (i.e. lighting conditions, exposure time, frame rate, resolution) and the sensor array specifications (i.e. pixel pitch, sensitivity, S/N ratio). The image space F/# is defined as the ratio between the focal length and the diameter of the entrance pupil (entrance pupil is the image of the aperture stop in object space):

$$F/\# = \frac{f}{D_{EP}} \tag{5-16}$$

The F/# of the lens is another important design tradeoff. As discussed in Section 2.1, a fast (small F/#) lens is desirable for several reasons. A faster lens delivers more light onto the sensor, increasing the S/N ratio of the system. This is essential, especially in the case of CMOS sensors, which are usually less sensitive than CCD sensors. The amount of light (irradiance) a lens puts onto the image plane is proportional to $\frac{1}{(F/\#)^2}$. More light onto the sensor also allows for a shorter exposure time (or faster frame rates, in the case of video), which is important in applications where the object moves quickly with respect to the imager, and real-time tracking is important. Another benefit of having more light onto the sensor is the ability to operate in poor lighting conditions. A small F/# will also increase the cutoff spatial frequency for the diffraction MTF of the optical system. On the other hand, wavefront aberrations increase dramatically with the aperture of the lens. Considering the third order Seidel aberrations, the spherical aberration is proportional to $\frac{1}{(F/\#)^3}$, coma is proportional to $\frac{1}{(F/\#)^2}$, and astigmatism and field curvature are proportional to $\frac{1}{F/\#}$. Therefore, complex optical designs are used to correct aberrations in fast lenses, making such optics relatively bulky compared to slower lenses. Other disadvantages of fast lenses are small depth-of-field and sensitivity to fabrication and assembly tolerances. Optical foveated imaging could be a possible method to reduce

complexity in fast wide-angle lenses and eliminate additional aberrations due fabrication tolerances.

6 CONCLUSIONS

This dissertation covered the methods and results of a detailed theoretical research study on the diffraction analysis, image quality, design, and optimization of fast wide-angle FOSs based on the current transmissive LC SLM technology.

We explained and quantified the amplitude and phase diffraction effects caused by the pixelated aperture of the SLM, revealing limitations imposed by the current transmissive LC SLM technology. The shadow mask and the discrete piston-only OPD introduced by the SLM are the main factors affecting the zero-order diffraction efficiency and MTF at the ROI. We developed a theoretical diffraction model to calculate the diffraction efficiency and MTF of an FOS. Our model quantifies the diffractive effects degrading the performance of these systems, and it is particularly useful as an FOS design and optimization tool. Based on this diffraction model, we wrote a Zemax macro that computes the zero-order diffraction efficiency and MTF for any lens design, SLM resolution, and pixel fill factor.

As a part of our study, we proposed five different fast wide-angle lens design examples that can be used to build practical FOSs based on the current transmissive SLM technology. The lens design examples studied here revealed additional challenges

specific to the optical design of fast wide-angle FOSs, such as controlling the relative illumination, distortion, and distribution of aberrations across a wide FOV with a limited number of elements. We also presented here the optical design we developed for a wide-angle FOS prototype built by the joint effort of several other research groups. The prototype was used for various demonstrations and experimental work.

One of the five lens design examples proposed here was chosen as a study case to demonstrate the design, analysis, and optimization of a practical wide-angle FOS based on the current state-of-the-art transmissive LC SLM technology. Our study revealed that choosing the optimal SLM resolution for a given lens design is a tradeoff between minimizing the amplitude diffraction effects caused by the shadow mask, and minimizing the phase diffraction effects caused by the discrete piston-only correction. We found that these diffractive effects limit the amount of wavefront aberration that can be efficiently corrected using transmissive LC SLMs. For instance, we determined that with the smallest phase mask width currently available, the maximum aberration in a wide-angle lens with a 10 mm stop diameter has to be less than roughly 10 waves P-V to achieve over 80% diffraction efficiency in the zero-order.

We also investigated the effects of fabrication and assembly tolerances on the image quality of fast wide-angle FOSs. These fast well-corrected optical systems are very sensitive to manufacturing errors. For instance, we showed that even with tight tolerances, additional aberrations caused by these errors severely degrade the image quality at the ROI. Therefore, a fast wide-angle FOS should be calibrated by measuring

these additional aberrations and adjusting the OPD patterns programmed into the SLM to cancel them out. We showed that the calibration has to be done over the entire FOV because the aberrations introduced by manufacturing errors vary with the field angle.

The theoretical study presented in this dissertation sets fundamental analysis, design, and optimization guidelines for future developments in fast wide-angle FOSs based on transmissive SLM devices. It also "sheds some light" on the mechanisms degrading the performance of these optical systems, pointing out the shortcomings of the fundamental concept and the limitations of the current technologies.

Further improvements in the fabrication technology of transmissive SLM devices are of paramount importance for future developments in the area of wide-FOV optical foveated imaging. Polarization-independent transmissive devices with high resolutions and larger fill factors could enable the realization of ultra-compact wide-angle FOSs capable of very high resolutions. Such FOSs could be combined with active variable-resolution CMOS sensors to develop compact, high-resolution imaging systems for applications where a wide FOV has to be constantly covered, and where size, weight, and fast data transmission are critical requirements.

APPENDIX A: PREVIOUS DESIGNS

Martinez et al [8]

Wavelength	550 nm
F/#	2.4
Full diagonal FOV	90 degrees
Image diagonal	50 mm
Effective focal length	25 mm
Wavefront error	215 waves
Distortion	2%
Drop in RI	78%
Total track	37 mm

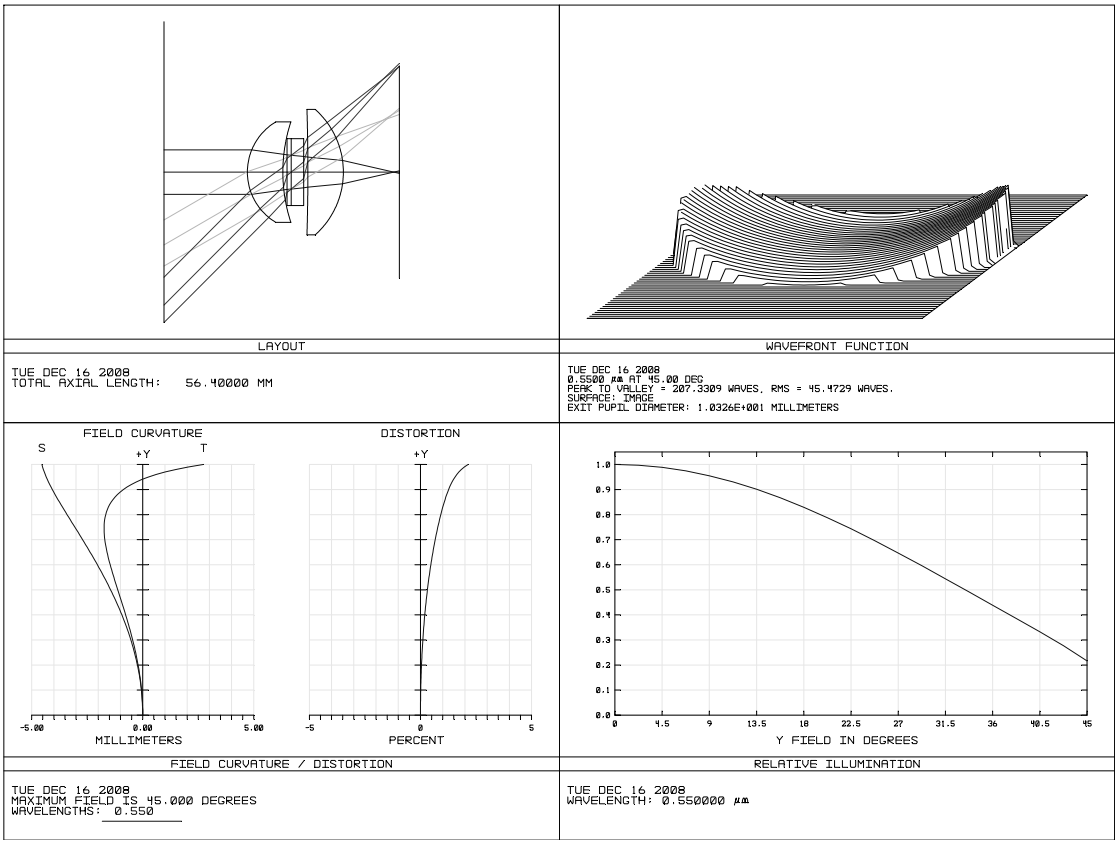

Wick et al [31]

Wavelength	550 nm
F/#	7.2
Full diagonal FOV	50 degrees (15 degrees experimental)
Image diagonal	70 mm
Effective focal length	34 mm
Wavefront error	9 waves
Distortion	2%
Drop in RI	22%
Total track	100 mm

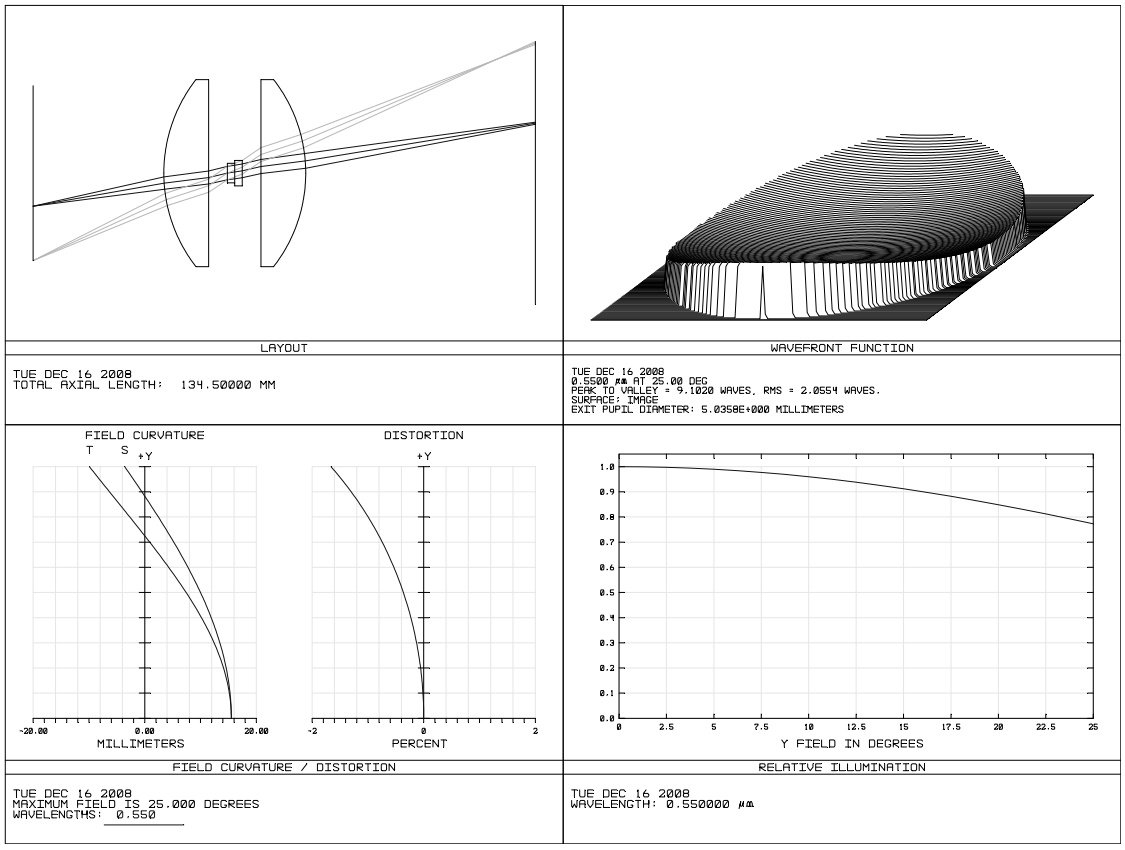

APPENDIX B: PRELIMINARY DESIGNS

Design #	# of elements	Max P-V WFE	Distortion	Drop in RI
1	3	< 16.5 waves	17.5%	14%
2	4	< 12.6 waves	29.9%	9%
3	5	< 11.3 waves	18.9%	8%
4	4	< 10.7 waves	20.2%	9%
5	5	< 6.6 waves	19.2%	3%
6	5	< 6.5 waves	19.3%	1%
7	4	< 11.0 waves	18.7%	5%

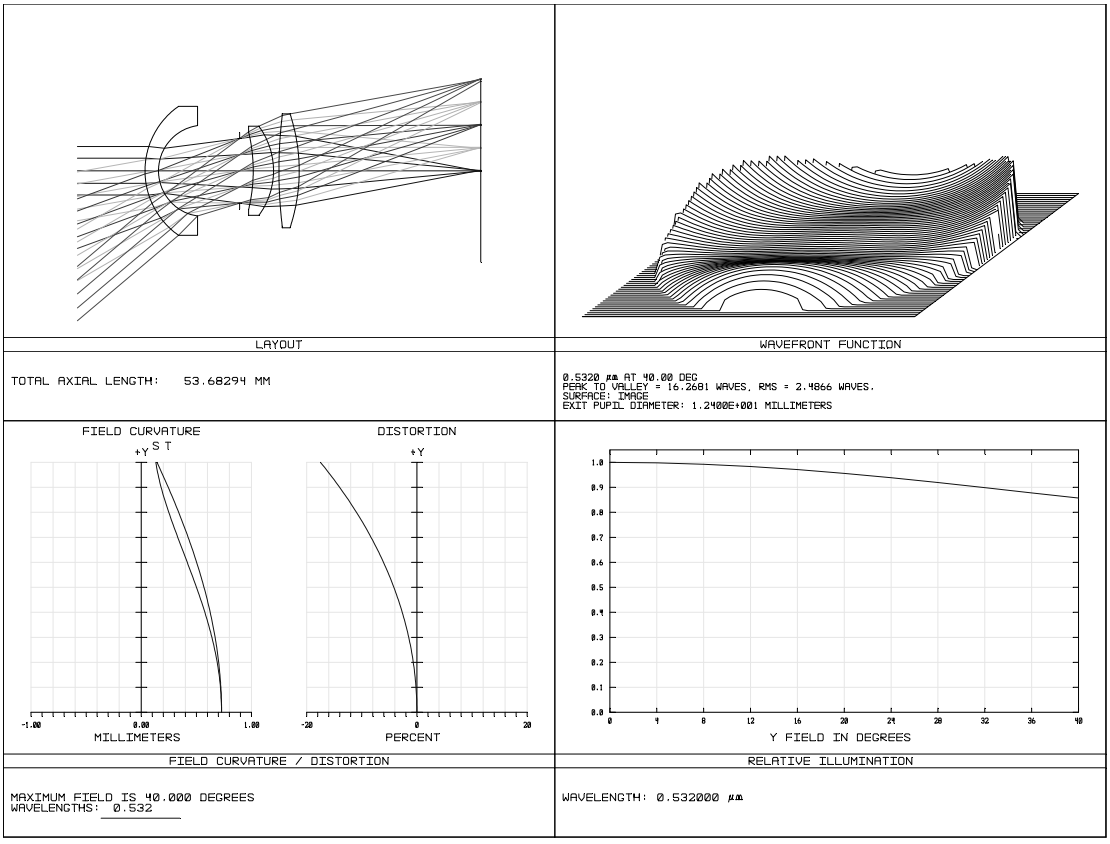

Design 1

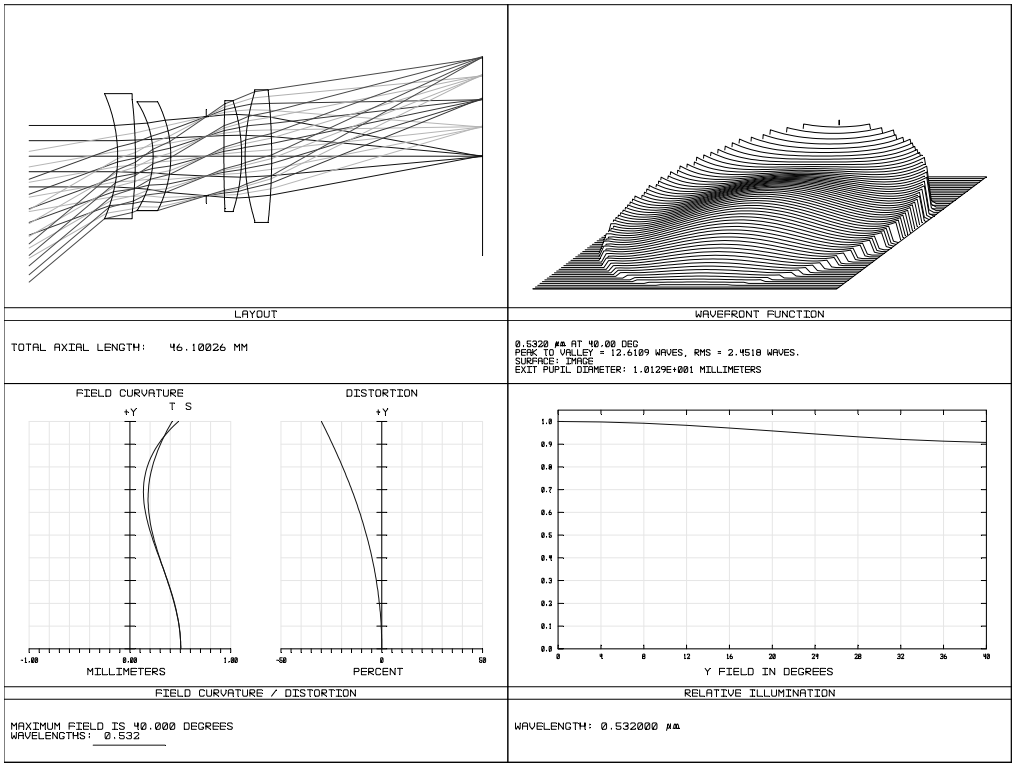

Design 2

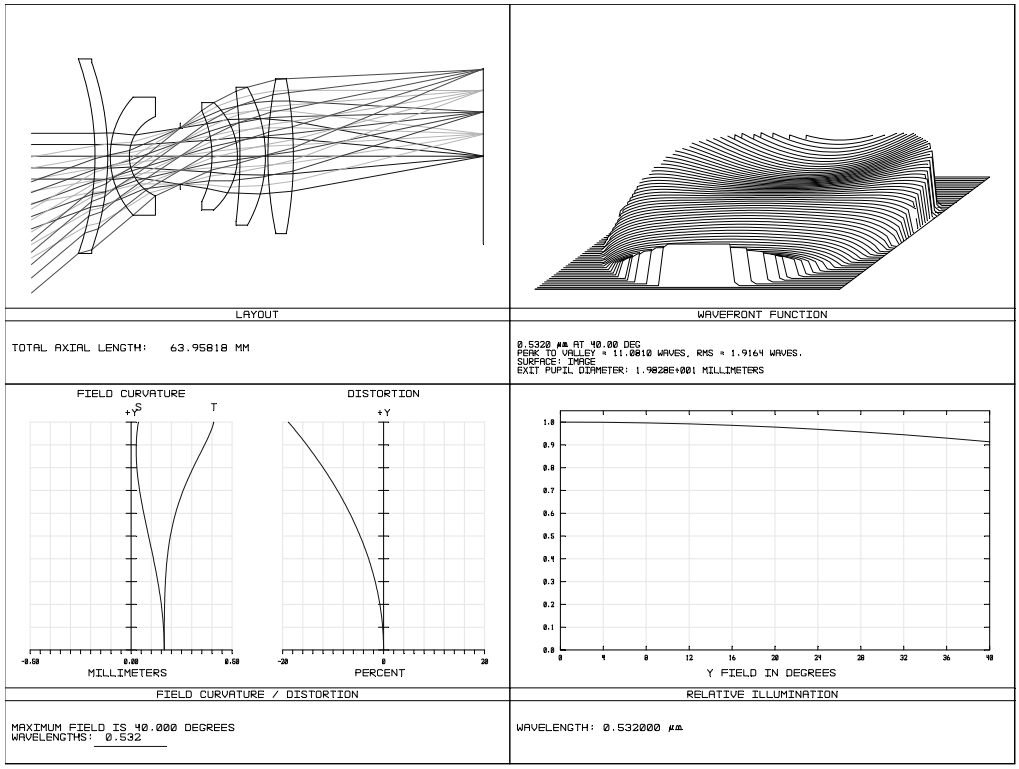

Design 3

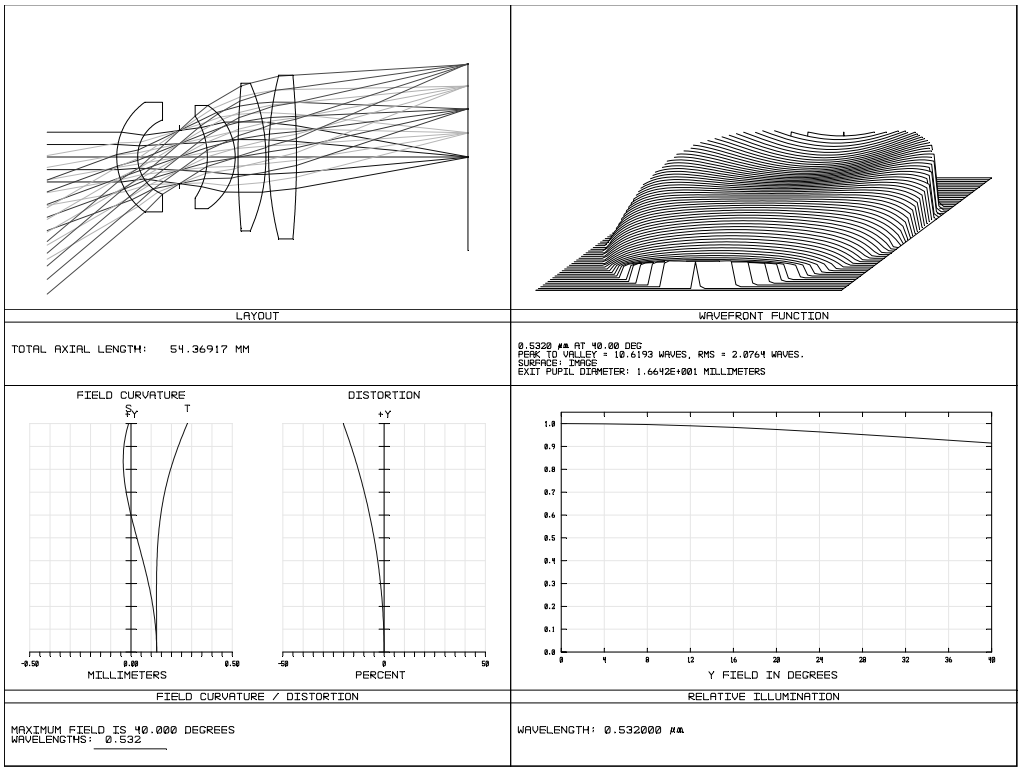

Design 4

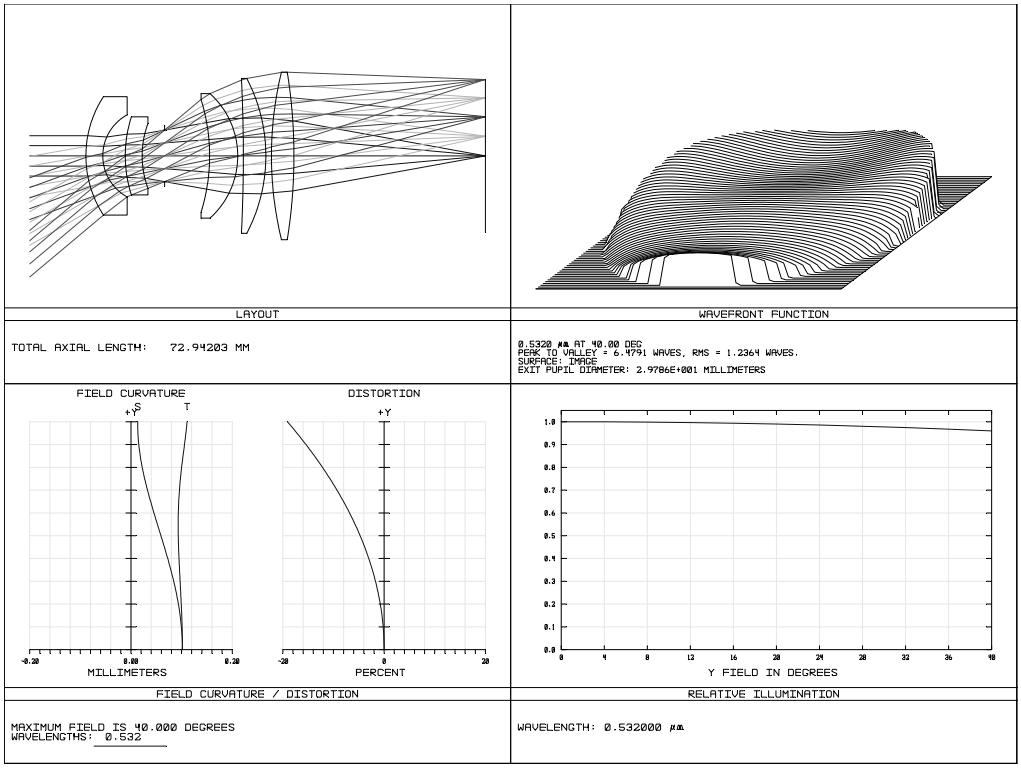

Design 5

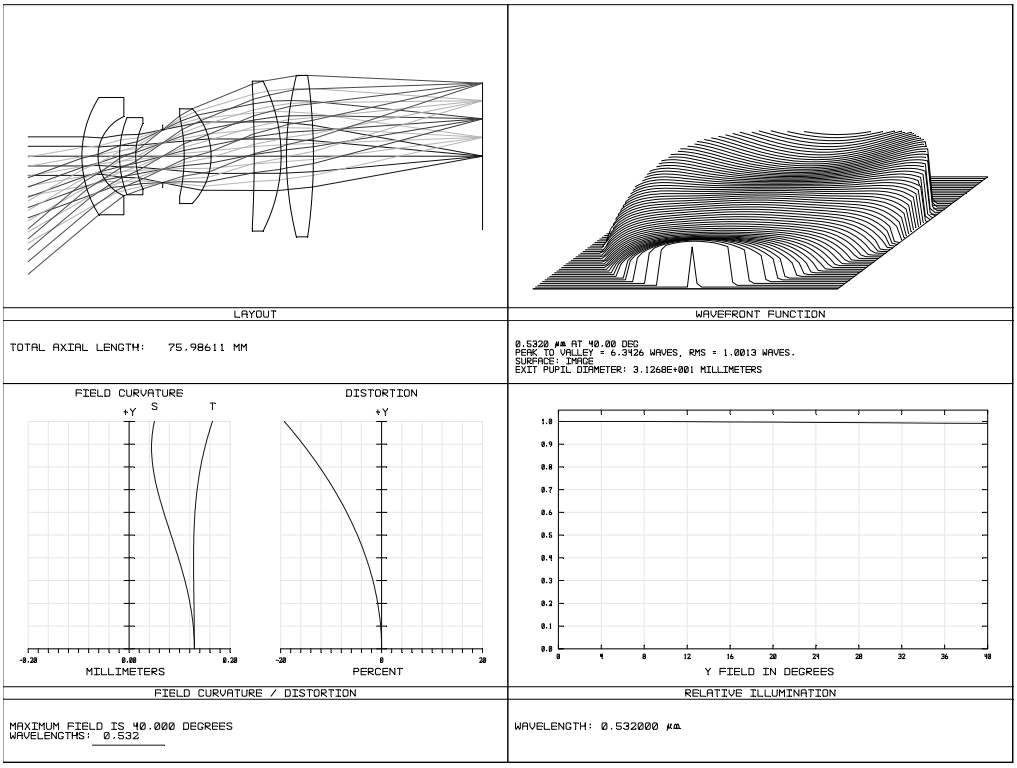

Design 6

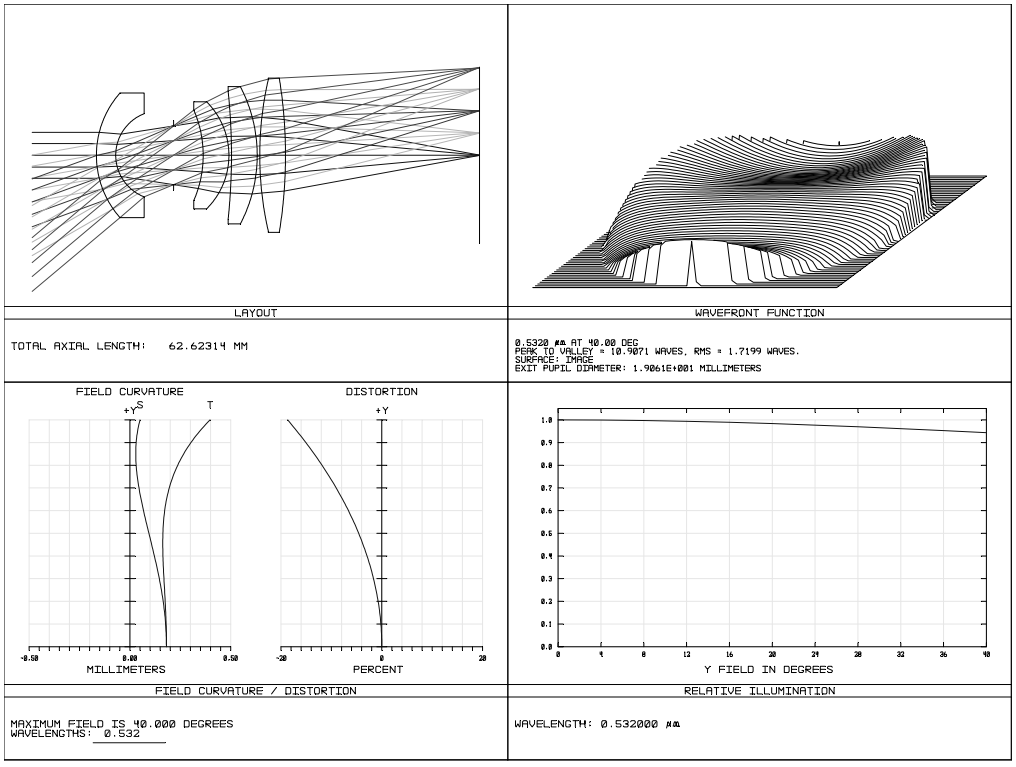

Design 7

APPENDIX C: ZEMAX MACRO TO DETRMINE THE DIFFRACTION EFFICIENCY AND MTF($\xi = 0$)

```
! This macro opens an N x N wavefront map file and reads the wavefront aberration into an array,
! A(i, j). It returns the RMS zero-order diffraction efficiency and MTF(0) assuming the SLM has a
! resolution of N x N, taking into account the ratio b/a. The macro also returns the RMS RWFE,
! the maximum P-V RWFE and the percentage of aperture where P-V RWFE > 0.25 waves.

INPUT "Enter file name:", filename$
INPUT "Enter N:", N
INPUT "Enter b/a ratio:", r

OPEN filename$
DECLARE A, DOUBLE, 2, N, N
FOR i, 1, N, 1
        FOR j, 1, N, 1
                READNEXT x
                A(i, j) = x
        NEXT
NEXT
CLOSE

total = 0
count = 0
max = 0
sum = 0
eff = 0

FOR i, 1, N-1, 1
FOR j, 1, N-1, 1
        IF (A(i, j) != 0)
                effx = 0
                effy = 0
                IF (A(i+1, j) != 0)
                        total = total + 1
                        RWFE = r * (A(i+1, j) - A(i, j))
                        effx = POWR(SINE(3.1416 * RWFE) / (3.1416 * RWFE), 2)
                        sum = sum + POWR(RWFE, 2)
                        IF (ABSO(RWFE) > 0.25) THEN count = count + 1
                        IF (ABSO(RWFE) > max) THEN max = ABSO(RWFE)
                ENDIF
                IF (A(i, j+1) != 0)
                        total = total + 1
                        RWFE = r * (A(i, j+1) - A(i, j))
                        effy = POWR(SINE(3.1416 * RWFE) / (3.1416 * RWFE), 2)
                        sum = sum + POWR(RWFE, 2)
                        IF (ABSO(RWFE) > 0.25) THEN count = count + 1
                        IF (ABSO(RWFE) > max) THEN max = ABSO(RWFE)
                ENDIF
                eff = eff + POWR(effx * effy, 2)
        ENDIF
NEXT
NEXT
```

```
PRINT " "
PRINT "RMS EFFICIENCY = ", POWR(r, 4) * SQRT(2 * eff / total) * 100, " %"
PRINT "MTF(0) = ", POWR(r, 3) * SQRT(2 * eff / total) * 100, " %"
PRINT " "
PRINT "RMS RWFE = ", 0.2887*SQRT(sum / total), " waves"
PRINT "Max P-V WFE = ", max, " waves"
PRINT "Percentage of pupil where P-V WFE > 0.25 waves = ", count / total * 100, " %"

END
```

APPENDIX D: TOLERANCE ANALYSIS RESULTS

Analysis for configuration 1 of 6

Units are Millimeters.
All changes were computed using linear differences.
All compensators were ignored.

Criterion : RMS Wavefront Error in waves
Mode : Sensitivities
Sampling : 3
Nominal Criterion : 0.66931093
Test Wavelength : 0.6328

Fields: User Defined Angle in degrees

#	X-Field	Y-Field	Weight	VDX	VDY	VCX	VCY
1	0.000E+000	0.000E+000	1.000E+000	0.000	0.000	0.000	0.000
2	0.000E+000	1.000E+001	1.000E+000	0.000	0.000	0.000	0.000
3	0.000E+000	2.000E+001	1.000E+000	0.000	0.000	0.000	0.000
4	0.000E+000	3.000E+001	1.000E+000	0.000	0.000	0.000	0.000
5	0.000E+000	4.000E+001	1.000E+000	0.000	0.000	0.000	0.000

Worst offenders:

Type	Value	Criterion	Change
TEDY 2 3	0.02000000	0.72003207	0.05072114
TTHI 11 12	0.02000000	0.70420716	0.03489624
TEDY 2 3	-0.02000000	0.70319494	0.03388401
TTHI 11 12	-0.02000000	0.69633507	0.02702414
TEDY 11 12	-0.02000000	0.69086217	0.02155124
TEDX 2 3	-0.02000000	0.68723338	0.01792245
TEDX 2 3	0.02000000	0.68723338	0.01792245
TTHI 14 16	0.02000000	0.68496875	0.01565783
TTHI 14 16	-0.02000000	0.68393699	0.01462607
TTHI 10 12	0.02000000	0.68018910	0.01087817

Estimated Performance Changes based upon Root-Sum-Square method:
Nominal RMS Wavefront : 0.66931093
Estimated change : 0.06454111
Estimated RMS Wavefront : 0.73385203

Monte Carlo Analysis:
Number of trials: 100
Initial Statistics: Normal Distribution

Nominal	0.66931093		
Best	0.66227728	Trial	5
Worst	0.84577010	Trial	8
Mean	0.70620987		
Std Dev	0.03626029		
90% <	0.73961744		
50% <	0.69680601		
10% <	0.67494999		

REFERENCES

1. W. J. Smith, *Modern Lens Design*, pp. 147-167, McGraw-Hill (1992).
2. http://63.240.118.132/images/Senior%20Site/Section%201/eye-diagram.jpg
3. S. J. Williamson and H. Z. Cummins, *Light and Color in Nature and Art*, Wiley (1983).
4. http://hyperphysics.phy-astr.gsu.edu/hbase/vision/rodcone.html
5. N. Tsumura, C. Endo, H. Haneishi, and Y. Miyake, "Image compression and decompression based on gazing area," *Proc. SPIE* **2657**, 361-367 (1996).
6. P. Kortum and W. Geisler, "Implementation of a foveated image coding system for image bandwidth reduction," *Proc. SPIE* **2657**, 350-360 (1996).
7. W. S. Geisler and J. S. Perry, "A real-time foveated multi-resolution system for low-bandwidth video communication," *Proc. SPIE* **3299**, 294-305 (1998).
8. T. Martinez, D. V. Wick, and S. R. Restaino, "Foveated, wide field-of-view imaging system using a liquid crystal spatial light modulator," *Opt. Express* **8**(10), 555-560 (2001).
9. R. K. Tyson, *Introduction to Adaptive Optics*, SPIE Press (2000).
10. J. W. Hardy, *Adaptive Optics for Astronomical Telescopes*, Oxford University Press (1998).
11. V. P. Lukin, P. F. Schippnick, *Atmospheric Adaptive Optics*, SPIE Press (1995).

12. J. Liang, B. Grimm, S. Goelz, and J. F. Bille, "Objective measurement of wave aberrations of the human eye with the use of a Hartmann-Shack wave-front sensor," *J. Opt. Soc. Am. A* **11**(7), 1949-1957 (1994).
13. D. Miller, D. R. Williams, G. M. Morris, and J. Liang, "Images of cone photoreceptors in the living human eye," *Vision Research* **36**(8), 1067-1079 (1996).
14. http://en.wikipedia.org/wiki/Foveated_imaging
15. M. Böhme, M. Dorr, T. Martinetz, and E. Barth, "Gaze-contingent temporal filtering of video," *Proceedings of ACM Symposium on Eye Tracking Research & Applications*, 109-116 (2006).
16. W. Zhou and A. C. Bovik, "Embedded foveation image coding," *IEEE Trans. on Image Processing* **10** (10), 1397-1410 (2001).
17. A. T. Duchowski and A. Çöltekin, "Foveated gaze-contingent displays for peripheral LOD management, 3D visualization, and stereo imaging," *ACM Transactions on Multimedia Computing, Communications, and Applications* **3**(4), 1-21 (2007).
18. 10. H. Murphy and A. T. Duchowski, "Hybrid image-model-based gaze-contingent rendering," *Proc. of ACM Symposium on Applied Perception in Graphics and Visualization*, 1-8 (2007).
19. G. Sandini, P. Questa, D. Scheffer, and A. Mannucci, "A retina-like CMOS sensor and its applications," *Proc. IEEE Workshop on Sensor Array and Multichannel Signal Processing*, 514–519 (2000).
20. T. Ienaga, K. Matsunaga, K. Shidoji, K. Goshi, Y. Matsuki, and H. Nagata, "Stereoscopic video system with embedded high spatial resolution images using two

channels for transmission," *Proc. of ACM Symposium on Virtual Reality Software and Technology*, 111–118 (2001).

21. A. Ude, C. Gaskett, and G. Cheng, "Foveated vision systems with two cameras per eye," *Proc. of IEEE International Conference on Robotics and Automation*, 3457-3462 (2006).
22. R. Etienne-Cummings, J. Van der Spiegel, P. Mueller, and M. Z. Zhang, "A foveated silicon retina for two-dimensional tracking," *IEEE Trans. Circuits Syst. II* **47**(6), 504-517 (2000).
23. G. Godin, P. Massicotte, and L. Borgeat, "High-resolution insets in projector-based stereoscopic displays: principles and techniques," *Proc. SPIE* **6055**, 60550F-1-12 (2006).
24. H. Hua and S. Liu, "Dual-sensor foveated imaging system," *Appl. Opt.* **47**(3), 317-327 (2008).
25. J. R. Janesick, *Scientific Charge-coupled Devices*, pp. 125-127, SPIE Press (2001).
26. Z. Zhou, B. Pain, and E. R. Fossum, "Frame-transfer CMOS active pixel sensor with pixel binning," *IEEE Trans. on Electron Devices* **44**(10), 1764 - 1768 (1997).
27. J. Coulombe, M. Swan, and C. Wang, "Variable resolution CMOS current mode active pixel sensor," *Proc. IEEE, International Symposium on Circuits and Systems 2000,* Vol. 2, 293-296 (2000).
28. F. Saffih and R. Hornsey, "Multiresolution CMOS image sensor," *Tech. Digest SPIE, Opto-Canada 2002*, 425 (2002).
29. http://www.aptina.com/products/image_sensors/
30. http://www.canon.com/technology/canon_tech/explanation/cmos/index.html

31. D. V. Wick, T. Martinez, S. R. Restaino, and B. R. Stone, "Foveated imaging demonstration," *Opt. Express* **10**(1), 60-65 (2002).

32. http://www.bnonlinear.com/products/XYphase/XYphase.htm

33. B. E. Bagwell, D. V. Wick, and J. Schwiegerling, "Multi-spectral foveated imaging system," *Proc. IEEE, Aerospace Conference 2006*, 1114 (2006).

34. J. Harriman, S. Gauza, S-T. Wu, D. V. Wick, B. Bagwell, T. Martinez, D. M. Payne, and S. Serati, "Transmissive spatial light modulators with high figure-of-merit liquid crystals for foveated imaging applications," *Proc. SPIE* **6135**, 61350C-1-13 (2006).

35. M. T. Gruneisen, R. C. Dymale, J. R. Rotgé, D. G. Voelz, and Melinda Deramo, "Wavelength-agile telescope system with diffractive wavefront control and acusto-optic spectral filter," *Opt. Eng.* **44**(10), 103202-1-5 (2005).

36. X. Zhao, "Broadband and wide field of view foveated imaging system in space," *Opt. Eng.* **47**(10), 103202-1-5 (2008).

37. B. E. Bagwell, D. V. Wick, W. D. Cowan, O. B. Spahn, W. C. Sweatt, T. Martinez, S. R. Restaino, J. R. Andrews, C. C. Wilcox, D. M. Payne, and R. Romeo, "Active zoom imaging for operationally responsive space," *Proc. SPIE* **6467**, 64670D-1-8 (2007).

38. B. Potsaid, Y. Bellouard, J. T. Wen, "Adaptive scanning optical microscope (ASOM): a multidisciplinary optical microscope design for large field of view and high resolution imaging," *Opt. Express* **13**(17), 6504-6518 (2005).

39. G. D. Love, "Wave-front correction and production of Zernike modes with a liquid-crystal spatial light modulator," *Appl. Opt.* **36**(7), 1517-1524 (1997).

40. W. C. Sweatt, O. B. Spahn, W. D. Cowan, and D. V. Wick, "Wavefront correction using micromirror arrays: Comparing the efficacy of tip-tilt-piston and piston-only micromirror arrays," *Proc. SPIE* **6342**, 6342071-6 (2006).

41. W. C. Sweatt, "Reduction of Zernike wavefront errors using a micromirror array,", Opt. Eng. 44(9), 980011-6 (2005).

42. G. Curatu, D. V. Wick, D. M. Payne, T. Martinez, J. Harriman, and J. Harvey, "Wide field-of-view imaging system using a liquid crystal spatial light modulator," *Proc. SPIE* **5874**, 587408-1-7 (2005).

43. X. Zhao, Y. Xie, and W. Zhao, "Wide field-of-view foveated imaging system," *Chinese Opt. Lett.* **6**(8), 561-563 (2008).

44. Y. H. Lin, H. Ren, Y. H. Wu, Y. Zhao, J. Fang, Z. Ge, and S. T. Wu "Polarization-independent liquid crystal phase modulator using a thin polymer-separated double-layered structure," *Opt. Express* **13**(22), 8746-8752 (2005).

45. R. K. Tyson, *Adaptive Optics Engineering Handbook*, pp. 151-195, CRC Press (2000).

46. D. V. Wick, D. M. Payne, T. Martinez, and S. R. Restaino, "Large dynamic range wavefront control of micromachined deformable membrane mirrors," *Proc. SPIE* **5798**, 158-161 (2005).

47. U. Efron, *Spatial Light Modulator Technology: Materials, Devices, and Applications*, CRC Press (1995).

48. S. T. Wu and D. K. Yang, *Fundamentals of Liquid Crystal Devices*, Wiley (2006).

49. http://www.sony.net/Products/SC-HP/brighterawld/index.html

50. H. Ren, Y. H. Lin, Y. H. Fan, and S. T. Wu, "Polarization-independent phase modulation using a polymer dispersed liquid crystal," *Appl. Phys. Lett.* **86**(14), 141110 (2005).

51. Y. H. Lin, H. Ren, Y. H. Fan, Y. H. Wu, and S. T. Wu, "Polarization-independent and fast-response phase modulation using a normal-mode polymer-stabilized cholesteric texture," *J. Appl. Phys.* **98**(4), 043112 (2005).

52. J. W. Goodman, *Introduction to Fourier Optics*, pp. 104, Roberts & Co. Pub., 3rd Ed. (2004).

53. G. D. Boreman, *Modulation Transfer Function in Optical and Electro-Optical Systems*, pp. 22, SPIE Press (2001).

54. http://www.zemax.com